MOLECULAR BEAM STUDY OF VAN DER WAALS MOLECULES: SPIN-ROTATION INTERACTION IN POTASSIUM-ARGON

by

EDWARD MARTIN MATTISON
B. S., Queens College, C. U. N. Y.
(1963)

SUBMITTED IN PARTIAL FULFILLMENT OF THE
REQUIREMENTS FOR THE DEGREE OF
DOCTOR OF PHILOSOPHY
at the
MASSACHUSETTS INSTITUTE OF TECHNOLOGY
February, 1974

Signature of Author: Signature redacted
Department of Physics, January 16, 1974

Certified by: Signature redacted
Thesis Supervisor

Accepted by: Signature redacted
Chairman, Departmental Committee on Graduate Students

MOLECULAR BEAM STUDY OF VAN DER WAALS MOLECULES:

SPIN-ROTATION INTERACTION IN POTASSIUM-ARGON

Submitted to the Department of Physics on January 16, 1974, in partial fulfillment of the requirements for the degree of Doctor of Philosophy.

ABSTRACT

We report a study, by molecular beam methods, of an alkali--rare-gas van der Waals molecule. Paramagnetic potassium-argon molecules (KAr) were produced in a supersonic molecular beam, and their magnetic resonance spectrum was observed. Central to the experiment was a measurement of the spin-rotation interaction $h\gamma \vec{S} \cdot \vec{N}$, where $\hbar\vec{S}$ is the spin angular momentum of the alkali valence electron and $\hbar\vec{N}$ is the rotational angular momentum of the molecule. The average spin-rotation constant was found to be $\bar{\gamma} = 240(5)$ kHz.

The magnetic energy levels of KAr have been calculated as functions of magnetic field by means of second-order perturbation theory. The results of computer simulations of the shape of the molecular spectrum are in good agreement with experimentally observed spectra.

Thesis Supervisor: Daniel Kleppner

Title: Associate Professor of Physics

To Marsha

TABLE OF CONTENTS

Page

SECTIONS

TABLE OF CONTENTS (continued)

Page

TABLE OF CONTENTS (continued)

TABLE OF CONTENTS (continued)

LIST OF FIGURES

LIST OF FIGURES (continued)

LIST OF TABLES

CHAPTER 1

INTRODUCTION

1.1 Statement of Problem

The existence of van der Waals molecules--molecules weakly bound by the induced dipole "van der Waals" force--has been recognized by spectroscopists for many years. Recently interest has increased in van der Waals molecules, particularly in those consisting of an alkali and a rare-gas atom, because of their role in electron-spin relaxation in optical pumping experiments (BOU69, BOU70, BOU72A, BOU72B)[*]. These experiments indicate that spin relaxation of an alkali vapor in an inert buffer gas is due primarily to formation of alkali--rare-gas molecules; the relaxation mechanism is the spin-rotation interaction $h\gamma \vec{S} \cdot \vec{N}$ between the spin $\hbar\vec{S}$ of the alkali valence electron and the rotational angular momentum $\hbar\vec{N}$ of the molecule. The experiments yield a value for the spin-rotation constant γ averaged over a thermal distribution of vibrational and rotational molecular states. They have not, however, been capable of determining the dependence of γ on rotational and vibrational state.

In the past decade experiments on molecular clustering have focused attention on the production of van der Waals molecules in rare gases and in other gaseous systems. It has been shown that clustering is enhanced in supersonic molecular beams, which are generated by the rapid expansion of a high pressure gas through an orifice into a vacuum. Supersonic beams have been produced that contain substantial fractions

---

[*] References to the published literature are listed at the end of the thesis. Notes amplifying the text will be found at the ends of the chapters. They are referred to in the text by numerical superscripts, e.g., ^{1}.

of rare-gas van der Waals molecules (MIL67, GOL70, YEA72).

This thesis stands at the confluence of these events: it reports the study by molecular beam magnetic resonance (MBMR) of a new class of molecule, the paramagnetic alkali--rare-gas van der Waals molecule. In this application the MBMR technique is capable of providing information on a variety of subjects, including the molecular hyperfine shift and the spin-rotation interaction; the present work centers primarily on a study of the spin-rotation interaction in potassium-argon molecules.

1.2 Van der Waals Molecules

Van der Waals molecules are those molecules in which the binding is predominantly due to the long-range van der Waals force: the major attractive term in the inter-atomic potential varies as $1/R^6$, where R is the inter-atomic separation. The van der Waals force, also called the dispersion force, arises from the mutual induction of dipole moments in the atoms of the molecule ((HER50, p. 377f), (MAR39)).

The binding energy of a van der Waals molecule is so weak (about 0.01 eV, 1% of a typical chemical bond) that its lifetime in a gas is limited to the time between collisions; for this reason they have not been observed by the usual chemical methods. Van der Waals molecules were originally discovered by spectroscopic observations. In systems that are not chemically bound, such as an alkali and a rare gas, the weak van der Waals attraction creates a shallow minimum in the molecular ground state potential energy curve at large atomic separations. Transitions from a van der Waals minimum to an excited state can be shifted in energy from the corresponding transition in isolated atoms (HER50, p. 395). The energy shifts produce band spectra, sometimes called staellite bands, at the sides of atomic absorption lines. References to observations of this effect are given by Herzberg (HER50, p. 395f), Ch'en and Takeo (CHE57), and Atakan and Jacobsen (ATA73); recent work is reported by Hedges et al. (HED72), Kudian and Welsh (KUD71), and Tanaka and Yoshimo (TAN72).

Polyatomic van der Waals systems, consisting of atom-molecule or molecule-molecule pairs, have been studied by electric resonance methods (DYK72, NOV73, HEN73). This technique is capable of measuring rotational, hyperfine, and other constants in polar molecules, but is not applicable to molecules lacking an electric dipole moment; it is also unsuitable for direct measurement of magnetic interactions.

As mentioned earlier, van der Waals molecules have been observed in optical pumping experiments. Bouchiat and her colleagues (BOU69, BOU70, BOU72A, BOU72B) have studied the relaxation of rubidium spin polarization in cells filled with argon, krypton, and xenon. We turn to this work in the next section.

1.3 Spin-rotation Interaction in Alkali--Rare-Gas van der Waals Molecules

The experiments of Bouchiat et al. gave the initial incentive for our measurement of the spectrum of alkali--rare-gas van der Waals molecules. Those workers measured the relaxation of optically pumped rubidium against backgrounds of argon, xenon, and krypton, as functions of rare-gas pressure and external dc magnetic field. Postulating that the spin relaxation is primarily due to the spin-rotation interaction $h\gamma(R)\vec{S}\cdot\vec{N}$ they found the behavior of the relaxation to be explained on the basis of the existence of two types of collisions: two-body "sudden" collisions lasting approximately 10 - 12 seconds; and "sticking" collisions, in which bound alkali--rare-gas molecules are formed as a result of three-body interactions and last for roughly 10^{-8} seconds, the collision time in the gas.

The spin-rotation constant is a function of the inter-atomic distance R, and therefore of the vibrational and rotational state of the molecule. Because the optical pumping method averages over a wide thermal distribution of molecular states, it is insensitive to the radial dependence of γ. The average values, $\bar{\gamma}$, obtained by Bouchiat et al. are (BOU72A):

	$\bar{\gamma}$ (MHz)
Rb-Ar	0.09 - 0.11
Rb-Kr	0.647 ± 0.018
Rb-Xe	1.4 - 1.7

Bouchiat and Pottier (BOU72B) report an optical pumping technique incorporating an rf field to induce spin-flips in alkali--rare-gas molecules in particular rotational states, thereby selectively changing the relaxation rate. The method is potentially capable of revealing the radial dependence of $\gamma(R)$. Their preliminary results failed to reveal any dependence of the spin-orbit coupling constant upon the vibration-rotation state of the molecule. However, they do not exclude the possibility of future experiments yielding different results.

Herman (HER64) has calculated the radial dependence of $\gamma(R)$ for rubidium--rare gas molecules. The application of this calculation to KAr is discussed in Chapter 2.

It is clearly advantageous to measure the spin-rotation interaction by a direct resonance technique that is sufficiently precise to determine the radial dependence of $\gamma(R)$; the MBMR method provides such an opportunity. Supersonic jets can produce substantial quantities of van der Waals molecules in a molecular beam, where they are completely isolated from other molecules and atoms. By observing the molecular magnetic resonance spectrum, the strength of the spin-rotation interaction can be deduced. Molecules containing alkalis are particularly attractive for MBMR because they have large magnetic moments (one Bohr magneton) that allow them to be deflected easily, and because they can be detected efficiently by a surface ionization detector.

1.4 Molecular Beam Magnetic Resonance Method

In MBMR, a beam of molecules or atoms passes through a state-selecting magnet, then through a resonance region, and finally through a second state selector, on its way to a detector (see Fig. 1-1). The state selectors are inhomogeneous magnets that deflect particles according to their spin states. We assume that spin-$\frac{1}{2}$ particles are involved, so only two spin states are possible. In Fig. 1-1 the source has been arranged so that particles in the "spin-up" state leave the first deflecting (or "A") magnet along the axis of the apparatus, while the spin-down particles are deflected into the magnet wall.

The second, or "C" magnet has parallel pole faces that create a uniform magnetic field. A resonance coil, supplied with rf current, is suspended in the C magnet. The rotating magnetic field created by this current can change the spin state of some of the beam particles. The beam leaving the C magnet, then, contains particles in both spin states, whereas the entering beam, due to the action of the A magnet, contained particles in only one state.

The second deflecting magnet (the "B" magnet) again separates the

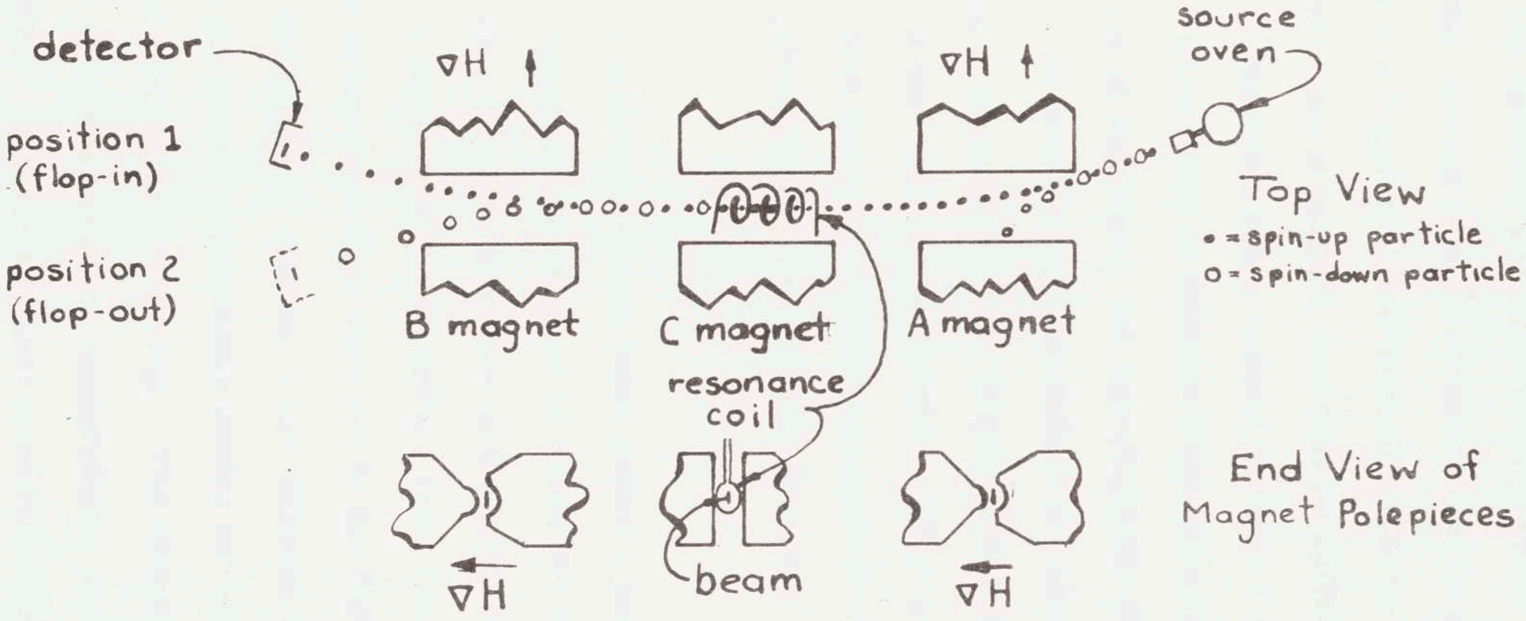

Fig 1-1
Molecular Beam Magnetic Resonance

particles according to their spin states. If no spins are flipped in the resonance region, all the particles passing through the B magnet will be in the spin-up state, and will strike the detector at position 1; none would be found if the detector were moved to position 2. If, however, the frequency of the current in the resonance coil is adjusted so that some of the spins are flipped, those particles will be in the spin-down state when they enter the B magnet, and will be deflected toward position 2. The number of particles going toward position 1 will decrease, while the number of particles found at position 2 (previously zero) will increase. Placing the detector at position 1 and observing the decrease in intensity as the rf frequency passes through resonance is called the "flop-out" technique; placing it at position 2 and observing the intensity increase at resonance is called the "flop-in" technique. Flop-in has the advantage of allowing one to look for a small increase against a small background, while flop-out requires looking for a small decrease in a large signal.

1.5 Jet Beams

A supersonic molecular beam (also called a jet, or nozzle, beam) is produced by a high-pressure source in which the mean free molecular path is much smaller than the diameter of the orifice from which the beam expands. A supersonic beam differs from traditional effusive molecular beams in having a high intensity in the forward direction and a narrow velocity distribution, that is, a low internal temperature. These properties make jet beams particularly useful for scattering experiments and for studies of molecular clustering. The characteristics and uses of jet beams are discussed in many publications, including AND65, AND66, GOR71, and ZOR74. Shapiro (SHA53) treats the theory of isentropic nozzle flow.

Different mass species in a jet beam have the same average velocity. In the present experiment, this allows the relative deflections of potassium-argon molecules and potassium atoms to be predicted accurately, and aids in the separation of molecules from atoms.

The enhancement of molecular clustering in jet beams has been studied by many workers (GOL70, GOL72, GOR71, HAG72, MIL67, MIL70, YEA72). Yealland et al., for example, have produced beams of argon containing up to 10% Ar_2 (YEA72).

In studies of jet beams of alkalis, several workers have come to conflicting conclusions regarding the vibrational temperatures of dimers in the beams. Gordon and Herschbach (GOR71) and Forman, Kendall, and Grice (FOR72) concluded from considerations of energy balance that Rb_2, Cs_2, and K_2 molecules in supersonic beams were vibrationally excited. On the other hand, Sinha, Schultz, and Zare (SIN73), using observations of induced fluorescence, found substantial vibrational cooling of Na_2 and K_2 in such beams: they measured vibrational and rotational temperatures of $153^\circ K$ and $55^\circ K$, respectively, for Na_2. Dyke et al. (DYK72) used electric resonance spectroscopy to measure a rotational temperature of $64 \pm 30^\circ K$ in a beam of HCN from a $283^\circ K$ nozzle source.

Because the shape of the molecular magnetic resonance spectrum depends upon the distribution of internal states, a comparison of observed and calculated MBMR spectra may prove capable of yielding an independent measurement of vibrational and rotational temperatures.

CHAPTER 2

THEORY

2.1 Introduction

Physical theory is used to design an experiment and to predict its results; the results, in turn, test or extend the theory. In this chapter we will discuss the interactions in potassium-argon molecules in order to explain how the experiment works, and what results are to be expected. The experimentally observed molecular spectra are presented in Chapter 5, with a discussion of their implications.

The weak binding of argon-potassium is indicative of the fact that the argon does not greatly perturb the potassium atom. In the next section we discuss the energy levels of a free potassium atom in a magnetic field. In section 2.3 we will describe the additional interactions in the van der Waals molecule, and their effects on the magnetic resonance spectrum.

Because the interactions giving rise to the spin-rotation coupling in the molecule are short-range, the spin-rotation constant γ is a function of the inter-nuclear distance R, and therefore of the molecule's rotational and vibrational state. The functional dependence of γ on R, and the distribution of molecular states--that is, the rotational and vibrational temperatures of the molecules--affect the shape of the observed molecular spectrum. A phenomenological discussion of the spectral shape is given in section 2.4.

A calculation of γ has been done by Herman (HER64) for Rb--rare-gas molecules. In section 2.5 we estimate the results of his calculation for KAr.

2.2 Energy Levels of Potassium

A. Hamiltonian

We are interested in the energy levels of a free potassium atom in a magnetic field. The hamiltonian for the interactions of the nuclear and electronic spins is

$$\mathcal{H} = ha\,\vec{I}\cdot\vec{S} + g_S\mu_o\vec{S}\cdot\vec{H}_o + g_I\mu_N\vec{I}\cdot\vec{H}_o \tag{2.1}$$

where $\hbar\vec{I}$ = nuclear spin

$\hbar\vec{S}$ = electron spin ($S = \frac{1}{2}$)

a = hyperfine coupling constant

g_S = electron g factor = $-\mu_S/S\mu_o \cong 2$

μ_o = Bohr magneton ($\mu_o/h = 1.398$ MHz/G)

g_I = nuclear g factor = $-\mu_I/I\mu_N$

μ_N = nuclear magneton ($\mu_N/h = 762.3$ Hz/G)

H_o = applied magnetic field

(In this thesis most interaction energies are expressed in terms of frequency, that is, (energy)/h.)

Two stable isotopes of potassium exist. Their characteristics and those of argon are given in Table T2.1. Because ^{39}K and ^{41}K have the same nuclear spin, their energy levels are similar. In any event, the low abundance of ^{41}K allows one to ignore its contribution to the observed molecular spectrum. (^{41}K does affect the atomic resonances, however, as discussed in section 4.3D.)

B. Energy Levels

In the absence of a magnetic field the hyperfine interaction couples $\vec{I}$ and $\vec{S}$ to form $\vec{F}$:

Table T2.1

Properties of Potassium and Argon

	Symbol	Value ^{39}K	^{41}K	^{40}Ar	Units	Reference
Atomic Number	Z	19	19	18		
Atomic Weight	A	39	41	40		
Natural Abundance		93%	6%	100%		
Atomic Hyperfine Separation	$\Delta\nu_{hfs}$	461.723	254.108	0	MHz	RAM56, p. 255
Nuclear Spin	I	3/2	3/2	0		
Nuclear g Factor	g_I	+0.391	+0.215	0		FUL65
Ground Electronic State		$4s\ ^2S_{\frac{1}{2}}$	$4s\ ^2S_{\frac{1}{2}}$	$3p^6\ ^1S_0$		

$$\vec{F} = \vec{I} + \vec{S} \qquad (2.2)$$

The good quantum numbers in this case are F, m_F ($= m_I + m_S$), I, and S. A high magnetic field decouples $\vec{I}$ from $\vec{S}$, and the good quantum numbers are I, m_I, S, and m_S. In intermediate fields the eigenfunctions of the hamiltonian (2.1) are neither pure (F, m_F) states nor pure (m_I, m_S) states; however, m_F is a good quantum number in all magnetic fields.

With $S = \frac{1}{2}$ and $I = 3/2$, the possible values of F are

$$F = 1,\ 2 \qquad (2.3)$$

The energy levels are given by the Breit-Rabi formula (RAM56, p. 80):

$$W(F, m_F) = -\frac{\Delta W}{2(2I+1)} - \frac{\mu_I}{I} H_o m_F \pm \frac{\Delta W}{2}\sqrt{1 + \frac{4m_F}{2I+1}x + x^2} \qquad (2.4)$$

where $\Delta W = h(\Delta\nu_{hfs}) =$ hyperfine separation

$$x = \frac{(g_S\mu_o - g_I\mu_N)H_o}{\Delta W}$$

and

$$\Delta W = \frac{ha}{2}(2I+1)$$

(Although F is not a good quantum number for high fields, it may be used as a label because the energy levels are continuous functions of H_o and go to the (F, m_F) values for $H_o \to 0$.)

Because of the small size of $\mu_I H_o$ compared with the other terms in Eq. 2.4 ($\mu_I/\mu_S \cong 3 \times 10^{-5}$ in ^{39}K), we shall henceforth ignore the contribution of μ_I. For $I = 3/2$, then,

$$W(F, m_F) = -\frac{\Delta W}{8} \pm \frac{\Delta W}{2}\sqrt{1 + m_F x + x^2} \quad \text{for } F = \binom{2}{1} \qquad (2.5)$$

or

$$W(F, m_F) = -\frac{ha}{4} \pm ha\sqrt{1 + m_F x + x^2} \qquad (2.6)$$

$$\text{with} \quad x = \frac{g_S\mu_o H_o}{\Delta W} = \frac{g_S\mu_o H_o}{2\,ha}$$

$W(F, m_F)$ is shown as a function of x in Fig. 2-1. It will be seen from Fig. 2-1, or from Eq. 2.5, that the separation between the $m_F = 2$ and $m_F = -2$ states is equal to the hyperfine separation when $x = 1$; thus x measures the degree of coupling of $\vec{S}$ to the magnetic field.

From Fig. 2-1 we can easily see which transitions are observable in an MBMR experiment. The MBMR apparatus detects changes in electron spin state; that is, between high-field states labelled $m_S = +\frac{1}{2}$ and those labelled $m_S = -\frac{1}{2}$. In the low-field region, where $\vec{I}$ and $\vec{S}$ are strongly coupled, the magnetic dipole selection rules are $\Delta F = 0, \pm 1$, $\Delta m_F = 0, \pm 1$. In this region $\Delta F = \pm 1$ transitions have energies of the

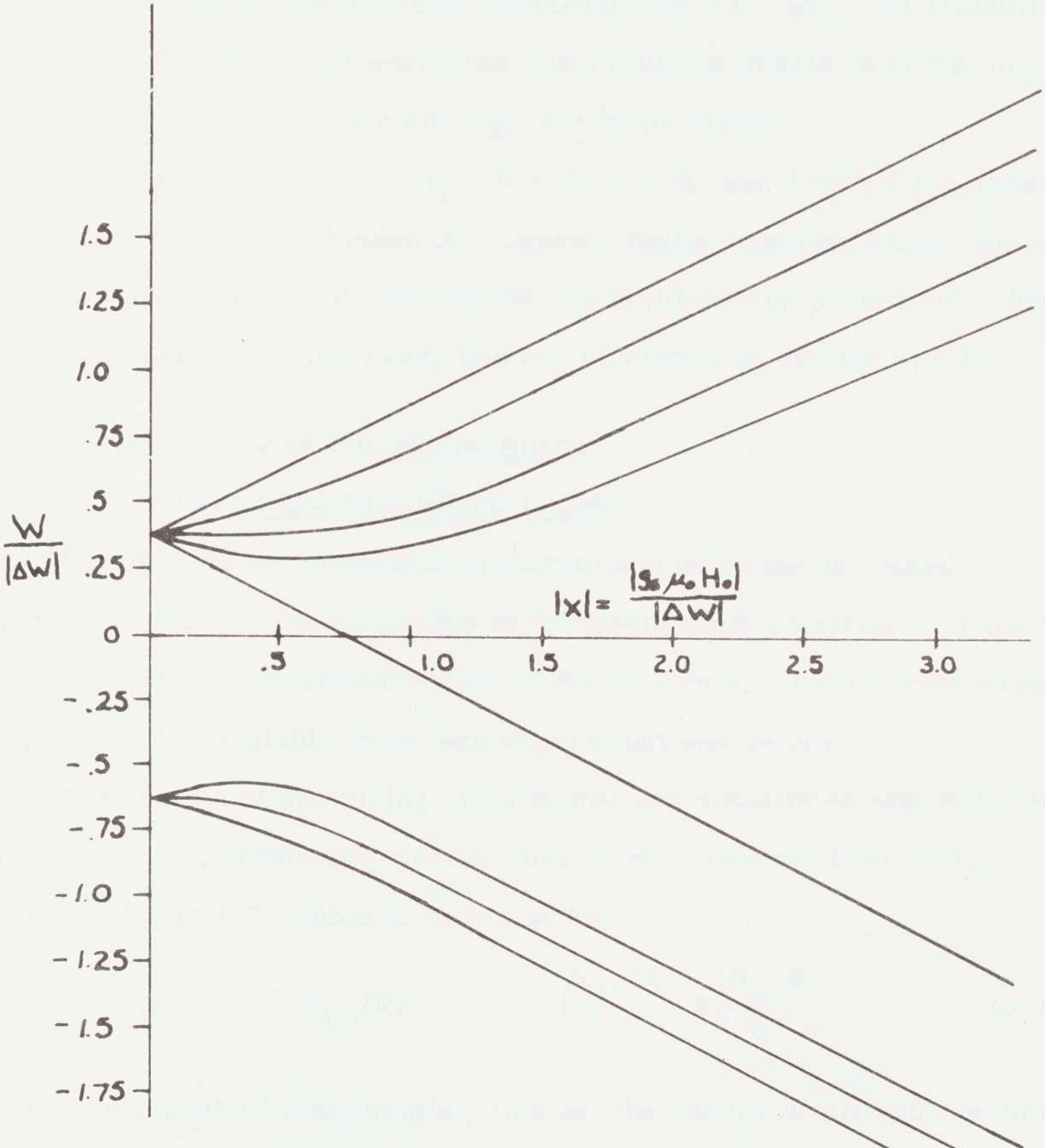

Fig. 2-1 Energy Levels of Potassium in a Magnetic Field.

order of the hyperfine separation, or approximately 460 MHz for ^{39}K. The frequencies of $\Delta F = 0$, $\Delta m_F = \pm 1$ transitions, however, depend on H_o, and can be made as small as is convenient. For this reason, and because the corresponding molecular transitions, described in section 2.3, yield an easily interpretable spectrum, $\Delta F = 0$, $\Delta m_F = \pm 1$ transitions are used. The only such transition observable by MBMR is $(F = 2, m_F = -1) \rightarrow (F = 2, m_F = -2)$, indicated in Fig. 2-1 by an arrow.

The transitions $(F = 2; m_F = 0 \rightarrow -2, 1 \rightarrow -2, \text{ and } 2 \rightarrow -2)$, i.e., those with $\Delta m_F = \geq 1$, are forbidden by magnetic dipole selection rules, but can proceed, albeit with small probability, by multi-photon processes. These transitions have been observed, and are discussed in section 4.3.D.

2.3 Energy Levels of Potassium-Argon

A. Rotational and Vibrational Levels

Interpreting the molecular spectrum and deducing the radial dependence of γ require knowledge of the interatomic potential V(r) and of the rotational and vibrational states of the molecule. Information about the potential is available from both experiment and theory.

The results of scattering experiments are sometimes expressed in terms of a two-parameter potential such as the Lennard-Jones 6-12 potential of Eq. 2.7, which is shown in Fig. 2-2.

$$V_{LJ}(R) = \epsilon\left[\left(\frac{R_m}{R}\right)^{12} - 2\left(\frac{R_m}{R}\right)^{6}\right] \tag{2.7}$$

ϵ is the well depth of the potential, that is, the energy at the equilibrium separation $R = R_m$. For potassium-argon, Düren et al. (DUR68) have found

$$\epsilon = 0.86 \times 10^{-14} \text{ erg}$$

$$R_m = 5.05 \text{ Å}$$

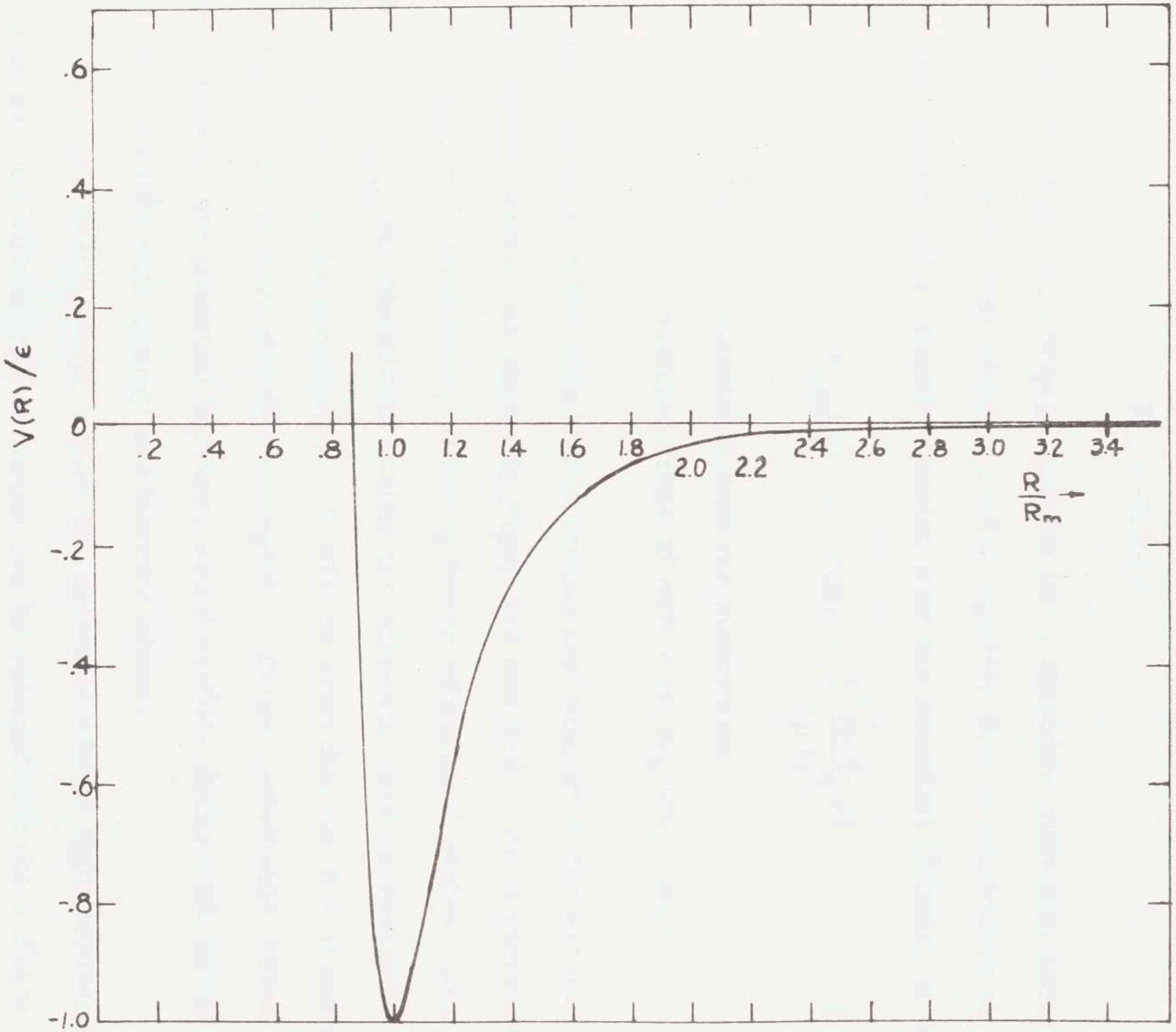

Fig. 2-2 Lennard-Jones 6-12 Potential.

The ab **initio** calculation by Baylis (BAY69) of the KAr potential has produced a tabulated function having the same general shape as Fig. 2-2 but, of course, a different functional dependence upon R. Baylis finds

$$\epsilon = 0.84 \times 10^{-14} \text{ erg}$$

$$R_m = 5.24 \text{ Å}$$

Solving the Schrodinger equation for a diatomic molecule bound by a central potential V(R) yields a radial equation that is equivalent to a one-dimensional Schrodinger equation with the potential (SCH68, p. 453)

$$V_{eff}(R) = V(R) + \frac{\hbar^2 N(N+1)}{2\mu R^2} \qquad (2.8)$$

where $\hbar\vec{N}$ = rotational angular momentum

μ = reduced mass of pair = $m_1 m_2/(m_1 + m_2)$

For each value of N the effective potential can support a certain number of vibrational states, as shown in Figs. 2-3 and 2-4. As N increases, the well becomes shallower, allowing fewer vibrational states, until for some $N = N_{max}$ no vibrational states are allowed; this corresponds to dissociation of the molecule. It will be seen that for N > 0 some vibrational levels have positive energies. These metastable states can tunnel through the potential barrier, and therefore decay with lifetimes that vary rapidly with energy and barrier shape.

Near the well bottom, where the potential can be approximated by a parabola, the vibrational energies can be calculated from a linear harmonic oscillator model:

$$E_{vib} = (v + \tfrac{1}{2})\hbar\omega \qquad v = 0, 1, 2, \cdots \qquad (2.9)$$

where E_{vib} = energy of vibrational state above well bottom

$$\omega = \sqrt{k/\mu} = \left[\frac{1}{\mu}\left(\frac{d^2 v_{eff}}{dR^2}\right)_{R = R_{min}}\right]^{\frac{1}{2}}$$

For a Lennard-Jones 6-12 potential, the vibrational energies of the N = 0 state are

$$E_{vib} = \hbar\sqrt{\frac{72\epsilon}{\mu R_m^2}}\,(v + \tfrac{1}{2}) = \frac{12\epsilon}{\sqrt{\beta}}(v + \tfrac{1}{2}) \tag{2.10}$$

where $\beta = 2\mu\epsilon R_m^2/\hbar^2$ is a convenient dimensionless parameter. The separation between vibrational states, then, is

$$\Delta E_{vib} = \frac{12\epsilon}{\sqrt{\beta}} \tag{2.11}$$

By contrast, the rotational energies are

$$E_{rot} = \frac{N(N+1)\hbar^2}{2\mu R_m^2} = \frac{\epsilon}{\beta}N(N+1) \quad N = 0, 1, \cdots, N_{max} \tag{2.12}$$

with separation depending upon N:

$$\Delta E_{rot} = \frac{2N\epsilon}{\beta} \qquad N = 1, 2, \cdots, N_{max} \tag{2.13}$$

The ratio of vibrational to rotational separation is

$$\frac{\Delta E_{vib}}{\Delta E_{rot}} = \frac{6\sqrt{\beta}}{N} \tag{2.14}$$

For KAr, $\beta = 1.4 \times 10^3$. (We have used $R_m = 5.24$ Å, $\epsilon = 0.84 \times 10^{-14}$ erg.)

Thus

$$\frac{\Delta E_{vib}}{\Delta E_{rot}} = \frac{224}{N} \quad (= 7.5 \text{ for } N = 30) \qquad (2.15)$$

showing that the vibrational states are much more widely spaced than the rotational states. Figure 2-4 displays the energy levels in a manner that emphasizes the relative spacings. The energies were calculated by Goldhor (GOL72A) from the Baylis potential for KAr.

B. Hamiltonian

The interactions among the angular momenta $\hbar\vec{I}$, $\hbar\vec{S}$, and $\hbar\vec{N}$ of a molecule in a magnetic field $\vec{H}_o$ are given by the hamiltonian

$$\begin{aligned}\mathcal{H} = {} & [a+\alpha]h\vec{I}\cdot\vec{S} + g_S\mu_o\vec{S}\cdot\vec{H}_o + \gamma h\vec{S}\cdot\vec{N} + g_I\mu_N\vec{I}\cdot\vec{H}_o \\ & + g_N\mu_N\vec{N}\cdot\vec{H}_o + \gamma_I h\vec{I}\cdot\vec{N}\end{aligned} \qquad (2.16)$$

Nuclear and rotational magnetic moments are typically less than a nuclear magneton; therefore we expect the $\vec{I}\cdot\vec{H}_o$ and $\vec{N}\cdot\vec{H}_o$ terms to be less than $\vec{S}\cdot\vec{H}_o$ in the ratio $\frac{\mu_N}{\mu_o} \sim 5 \times 10^{-4}$. Similarly we expect $\frac{\gamma_I}{\gamma} \sim \frac{\mu_N}{\mu_o}$. Ignoring the last three terms in Eq. 2.16 we have

$$\mathcal{H} = [a+\alpha]h\vec{I}\cdot\vec{S} + g_S\mu_o\vec{S}\cdot\vec{H}_o + \gamma h\vec{S}\cdot\vec{N} \qquad (2.17)$$

α represents the shift in the potassium hyperfine coupling due to the perturbation by the argon; like γ, it is a function of the interatomic distance R, and consequently of the internal state of the molecule.

C. Energy Levels

In discussing the eigenvalues of the hamiltonian, 2.17, it is convenient to consider three ranges of magnetic field strength.

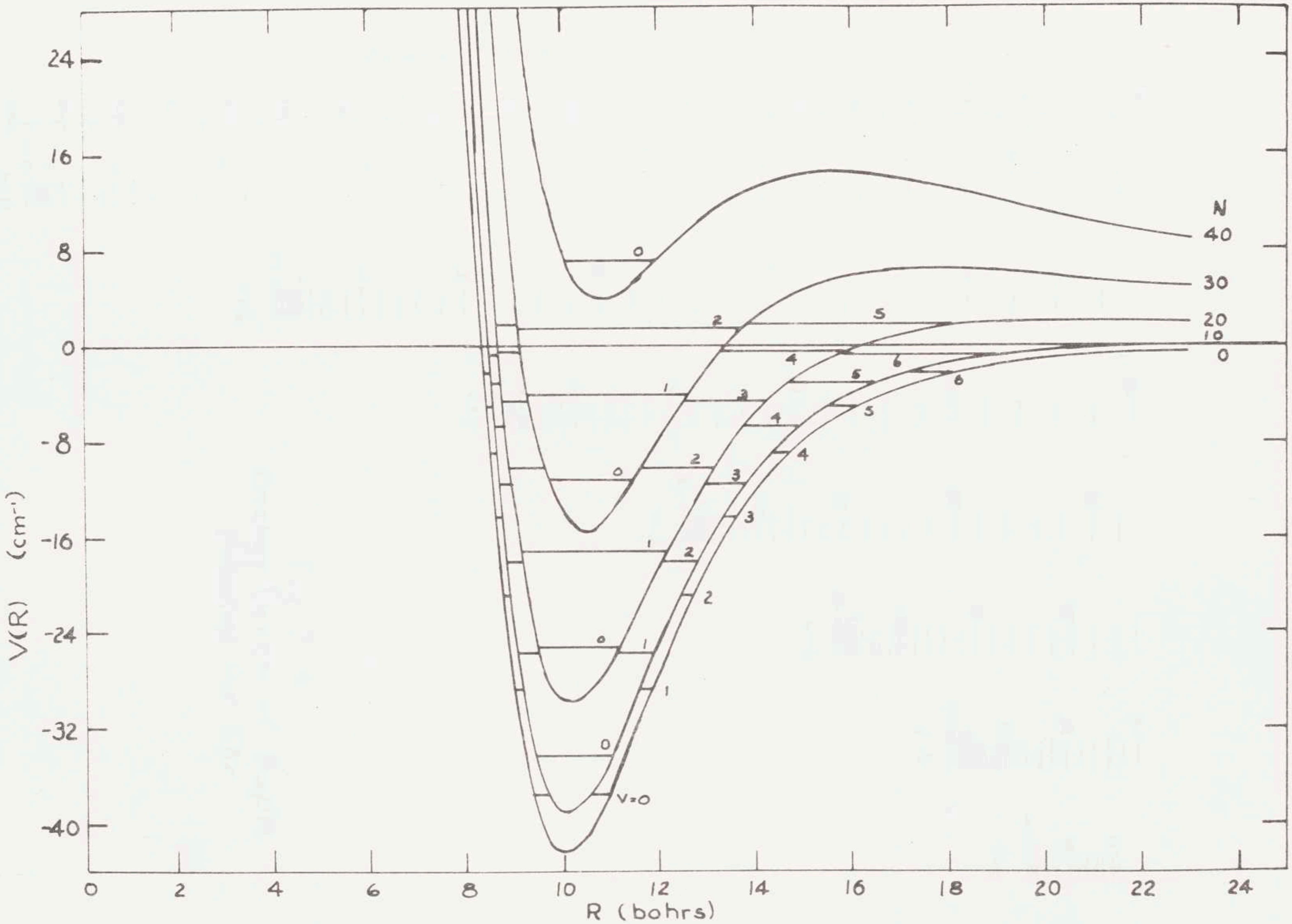

Fig. 2-3 Rotational and Vibrational Levels of KAr.
(Baylis Potential)

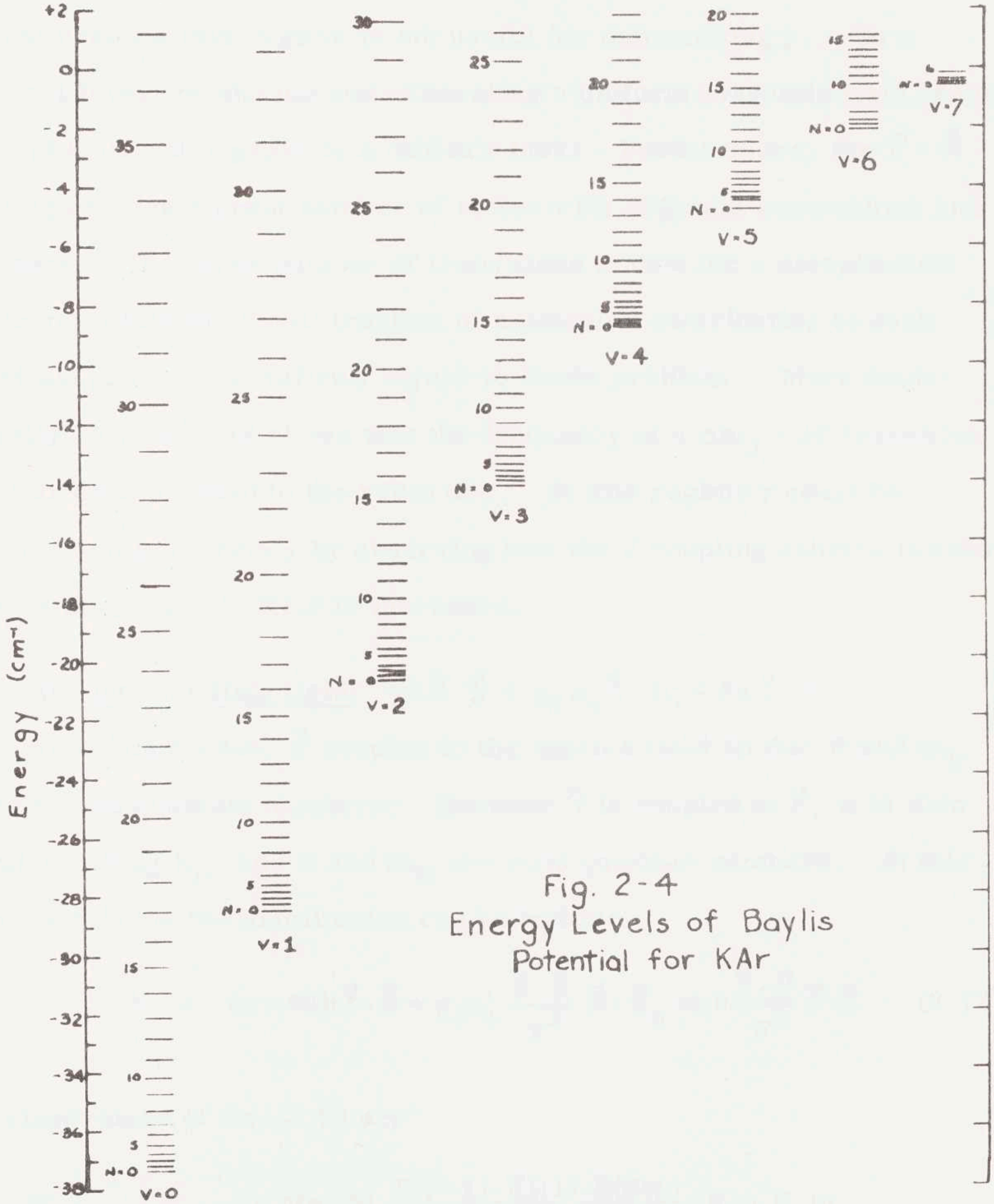

Fig. 2-4
Energy Levels of Baylis
Potential for KAr

(i) Low field: $0 \leq g_S \mu_o \vec{S} \cdot \vec{H}_o << \gamma h \vec{S} \cdot \vec{N}$

In a very low field ($H_o \leqslant 0.01$ G for $\gamma = 0.3$ MHz), $\vec{I}$ and $\vec{S}$ couple to form $\vec{F}$, and $\vec{F}$ couples to $\vec{N}$ (by means of the spin-rotation interaction) to form the total angular momentum $\vec{J}$: $\vec{J} = \vec{F} + \vec{N} = \vec{I} + \vec{S} + \vec{N}$. The energy levels in this coupling scheme are given in Appendix A2.1. For several reasons this regime is not useful for determining γ. On a practical level, producing and calibrating a uniform magnetic field of the order of 0.01 - 0.1 gauss is a difficult task. Furthermore, the $\vec{F} \cdot \vec{N}$ coupling creates a great number of states with different separations and g-factors. The large number of transitions makes for a complicated spectrum, while the small fraction of molecules contributing to each transition produces a difficult signal-to-noise problem. More fundamentally, Eq. A2.1/2 shows that the frequency of a $\Delta m_J = \pm 1$ transition is not directly related to the value of γ. In this regime γ could be measured only indirectly by observing how the J coupling scheme breaks down as the magnetic field is increased.

(ii) Intermediate field: $\gamma h \vec{S} \cdot \vec{N} < g_S \mu_o \vec{S} \cdot \vec{H}_o < ha \vec{I} \cdot \vec{S}$

As H_o increases, $\vec{F}$ couples to the applied field so that F and m_F become good quantum numbers. Because $\vec{N}$ is coupled to $\vec{F}$, it is also quantized along H_o, and N and m_N are good quantum numbers. In this coupling scheme the hamiltonian can be written

$$\mathcal{H} = (a + \alpha) h \vec{I} \cdot \vec{S} + g_S \mu_o \frac{\vec{S} \cdot \vec{F}}{F^2} \vec{F} \cdot \vec{H}_o + \gamma h \frac{\vec{S} \cdot \vec{F}}{F^2} \vec{F} \cdot \vec{N} \qquad (2.18)$$

The eigenvalues of Eq. 2.18 are

$$W_{F, m_F, N, m_N} = h(a+\alpha) \frac{F(F+1) - I(I+1) - S(S+1)}{2} + g_F \mu_o H_o m_F + \tfrac{1}{2} g_F \gamma h m_F m_N \qquad (2.19)$$

where $g_F = g_S \frac{\vec{S} \cdot \vec{F}}{F^2}$; $g_{F=2} = \frac{1}{2}$, $g_{F=1} = -\frac{1}{2}$. These energy levels are similar to those of free potassium in a low field, with the addition of the hyperfine shift and the term in m_N arising from the spin-rotation interaction.

Because H_o is non-zero in this regime, $\vec{I}$ and $\vec{S}$ are not completely coupled, F is not strictly a good quantum number, and Eq. 2.19 must be modified; this corresponds to the "intermediate field" regime of free potassium, treated by Ramsey (RAM56, p. 80). The exact energy levels are given by the Breit-Rabi formula, Eq. 2.4. This will be discussed in section 2.3D.

(iii) High field: $ha \vec{I} \cdot \vec{S} << g_S \mu_o \vec{S} \cdot \vec{H}_o$

In high field (in the A and B magnets, for example) $\vec{S}$ couples to H_o. Because $\vec{I}$ and $\vec{N}$ are coupled to $\vec{S}$, they too are coupled to the field. The good quantum numbers are S, m_S, I, m_I, N, and m_N. The energy is dominated by the $\vec{S} \cdot \vec{H}_o$ interaction, so there are two groups of levels, corresponding to $m_S = \pm\frac{1}{2}$, with substructure due to the hyperfine and spin-rotation interactions.

An energy level diagram showing the coupling regimes for N = 1 (the simplest non-trivial case) is given in Fig. 2-5.

D. Molecular Transitions in Intermediate Fields

In intermediate fields the spin-rotation coupling in KAr is a small perturbation to the Zeeman levels of the potassium atom. Consequently, the discussion in section 2.2C of the observable transitions in free potassium applies to KAr: the MBMR technique permits us to observe transitions in the molecule between the states (F = 2, m_F = -1) and (F = 2, m_F = -2). We wish to calculate the frequency of this transition

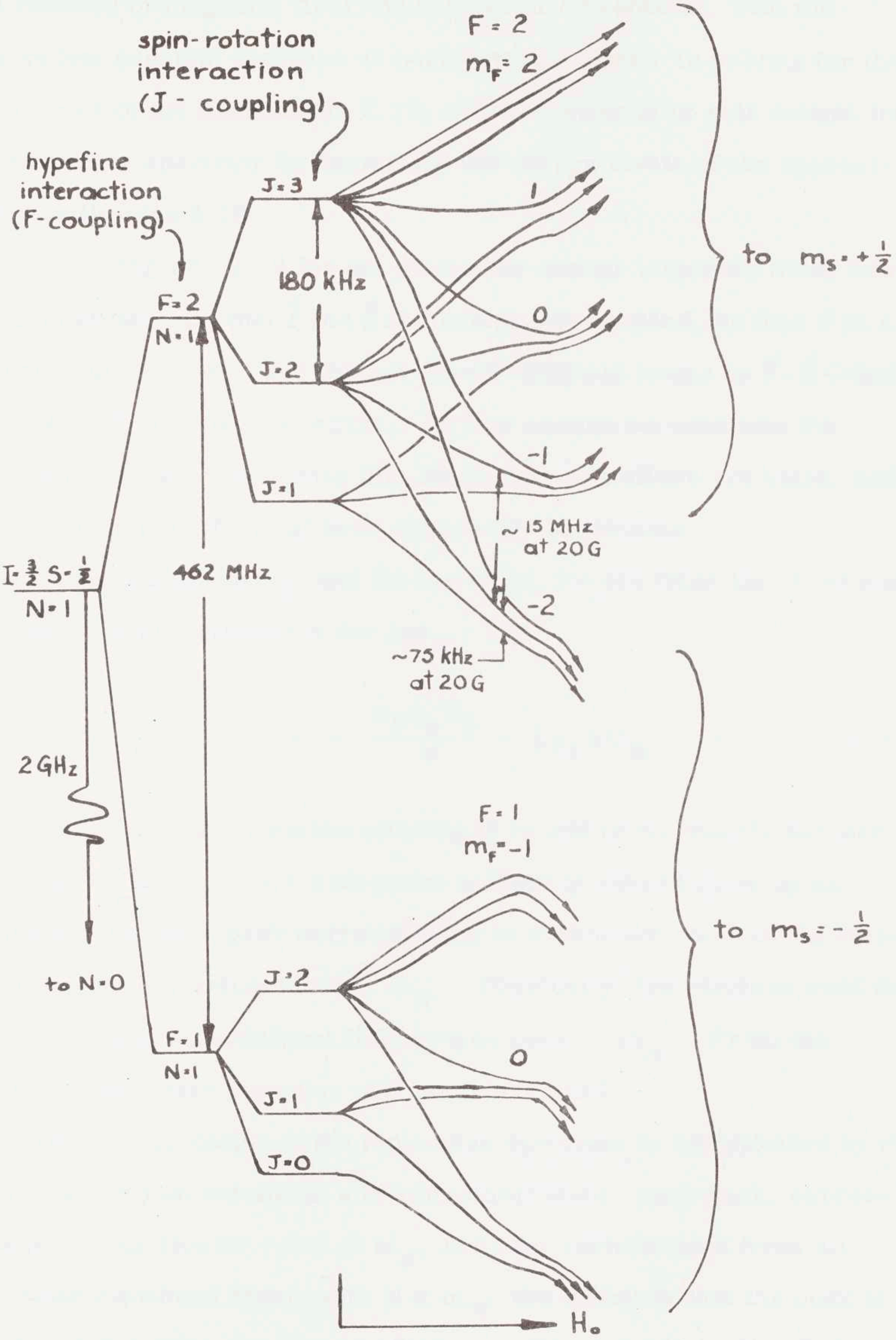

Fig. 2-5 Energy Levels of KAr in a Magnetic Field.

as a function of magnetic field and spin-rotation constant, with the appropriate quantum numbers as parameters. Prior to solving for the eigenvalues of the hamiltonian 2.17, we shall attempt to gain insight into the molecular spectrum by examining the energy levels of the approximate hamiltonian 2.18.

In writing Eq. 2.19 for the molecular energy levels we made two approximations: (a) that $\vec{I}$ and $\vec{S}$ are completely coupled, so that F is a good quantum number, and (b) that the off-diagonal terms in $\vec{F} \cdot \vec{N}$--that is, $F_+N_- + F_-N_+$--have no effect. In this section we calculate the transition frequency assuming that these approximations are valid, and then consider the effects of their successive breakdown.

If approximations (a) and (b) are valid, we see from Eq. 2.19 that the frequency of a transition for $\Delta m_F = 1$ is

$$\nu = \frac{g_F \mu_o H_o}{h} + \tfrac{1}{2} g_F \gamma m_N \qquad (2.20)$$

The effect of the spin-rotation coupling is to add to the atomic Zeeman resonance a fine structure with peaks uniformly spaced apart by an amount $\gamma g_F/2$, each peak corresponding to a different value of the rotational magnetic quantum number m_N. Physically, the electron sees the static field plus an additional field proportional to m_N. From the spacing of the peaks the value of γ can be obtained.

The interpretation of the molecular spectrum is complicated by the dependence of γ on rotational and vibrational state: each peak, corresponding to a particular value of m_N, includes contributions from all molecular rotational states with $N \geq m_N$; the result is that the peak is broadened and skewed. These effects are discussed in section 2.4.

Another complication arises from the breakdown of approximation (a): F is not really a good quantum number. Equation 2.19, then, does not give the exact energy levels, nor Eq. 2.20 the exact transition frequencies; instead, the Breit-Rabi formula must be used. We now show, however, that for sufficiently small fields the transition frequencies are given by a modification of Eq. 2.20 in which g_F is a function of magnetic field.

The hamiltonian of Eq. 2.17 can be written

$$\frac{\mathcal{H}}{h} = A\vec{I}\cdot\vec{S} + BS_z + \gamma S_z N_z + \gamma\left[\frac{S_+N_- + S_-N_+}{2}\right] \tag{2.21}$$

where $A = a + \alpha$, $B = g_S\mu_o H_o/h$. The eigenfunctions of the hamiltonian $A\vec{I}\cdot\vec{S} + BS_z$ are eigenfunctions of N^2 and N_z; therefore the term in square brackets has no diagonal matrix elements, makes no contribution in first order perturbation theory, and for the moment will be ignored: this is approximation (b). The eigenvalues of the remainder of $\mathcal{H}$ will be found exactly.

$\gamma S_z N_z$ has diagonal matrix elements with states (N, m_N): $\langle \xi, N, m_N | \gamma S_z N_z | \xi', N', m'_N \rangle = \gamma m_N \langle \xi | S_z | \xi' \rangle \, \delta_{NN'} \, \delta_{m_N m'_N}$. ($\xi$ and ξ' represent other quantum numbers). If $\gamma m_N S_z$ is included with BS_z, $\mathcal{H}$ becomes

$$\frac{\mathcal{H}}{h} = A\vec{I}\cdot\vec{S} + CS_z \tag{2.22}$$

where $C = B + \gamma m_N = \frac{g_S\mu_o H_o}{h} + \gamma m_N$. The Breit-Rabi formula gives for the eigenvalues of Eq. 2.22,

$$\nu_{F,m_F} = -\tfrac{1}{4}A \pm A\sqrt{1 + m_F x + x^2} \tag{2.23}$$

where $x \equiv C/2A$ and $\pm \Rightarrow F = \{{}^{2}_{1}\}$. The frequency of the transition $F = 2,\ m_F = -1 \rightarrow -2$ is

$$\nu = A\left[\sqrt{1-x+x^2} - \sqrt{1-2x+x^2}\right] = A\left[\sqrt{1-x+x^2} - (1-x)\right] \tag{2.24}$$

For $x < 1$ we expand the radical, keeping terms up to x^3:

$$\nu = A \cdot \frac{x}{2}\left[1 + \frac{3}{4}x + \frac{3}{8}x^2\right] \tag{2.25}$$

Now,

$$x = \frac{C}{A} = \frac{g_S\mu_o H_o/h + \gamma m_N}{2A} \tag{2.26}$$

so

$$\nu = \frac{1}{2}\left(\frac{\mu_o H_o}{h} + \frac{\gamma m_N}{2}\right)\left[1 + \frac{3}{4}x + \frac{3}{8}x^2\right] \tag{2.27}$$

The leading factor of $\frac{1}{2}$ is the quantity we have called g_F (for $F = 2$); the term in square brackets is a correction to g_F due to the non-zero magnetic field. Because x contains γm_N we must expand the quantity in square brackets. Let

$$x \rightarrow x + x' \tag{2.28}$$

where now

$$x = \frac{g_S\mu_o H_o}{2Ah} \tag{2.29}$$

$$x' = \frac{\gamma m_N}{2A} \tag{2.30}$$

(This corresponds to the conventional definition of x given by Ramsey (RAM56, p. 80).) Equation 2.27 becomes

$$\nu = \frac{A}{2}(x + x')\left[1 + \frac{3}{4}(x+x') + \frac{3}{8}(x+x')^2\right] \tag{2.31}$$

Keeping terms to order x^3 and $x'x^2$ we find

$$\nu = \frac{A}{2}x\left[1+\frac{3}{4}x+\frac{3}{8}x^2\right] + \frac{A}{2}x'\left[1+\frac{3}{2}x+\frac{9}{8}x^2\right] \qquad (2.32)$$

or

$$\nu = g'_F(x)\frac{\mu_o H_o}{h} + g''_F(x)\frac{\gamma}{2}m_N \qquad (2.33)$$

where

$$g'_F(x) = \tfrac{1}{2}\left(1+\frac{3}{4}x+\frac{3}{8}x^2\right) \qquad (2.34)$$

$$g''_F(x) = \tfrac{1}{2}\left(1+\frac{3}{2}x+\frac{9}{8}x^2\right) \qquad (2.35)$$

We see from Eq. 2.33 that in intermediate magnetic fields, coupling $\vec{S}$ to the field preserves the form of Eq. 2.20, but makes the g-factors (unequal) functions of H_o. For a Zeeman frequency of 15 MHz the correction to the spin-rotation g-factor is approximately 18%; this must be taken into account when determining γ from the spacing between the spectral peaks.

In calculating the eigenvalues of hamiltonian 2.21 in intermediate fields, we ignored the off-diagonal terms. Inclusion of these terms requires second-order perturbation theory. Let

$$\mathcal{H} = \mathcal{H}_o + \mathcal{H}' \qquad (2.36)$$

$$\mathcal{H}_o = Ah\,\vec{I}\cdot\vec{S} + g_S\mu_o H_o S_z \qquad (2.37)$$

$$\mathcal{H}' = \gamma h\,\vec{S}\cdot\vec{N} = \gamma h\,S_z N_z + \tfrac{1}{2}\gamma h(S_+N_- + S_-N_+) \qquad (2.38)$$

To calculate the energy levels of $\mathcal{H}$ one diagonalizes $\mathcal{H}_o$, finding its eigenvalues and eigenvectors, and then calculates the corrections to the energies due to the perturbation $\mathcal{H}'$. The first term in $\mathcal{H}'$, proportional to S_zN_z, has only diagonal matrix elements in the new basis; it contributes only in first order, yielding a transition frequency equivalent to Eq. 2.33. The second term has only off-diagonal matrix elements; it contributes in second order and gives a result that alters the shape of the molecular spectrum. The calculation is described in Appendix A2.2. The result is that the frequency ν of the transition between the states ($F = 2$, $m_F = -1$) and ($F = 2$, $m_F = -2$) is given by

$$\nu = \nu_{+}^{(0)} + \nu^{(1)} + \nu^{(2)} \tag{2.39}$$

with

$$\nu^{(0)} = g'_F(x)\,\mu_o H_o/h \tag{2.40}$$

$$\nu^{(1)} = g''_F(x)\,\gamma m_N/2 \tag{2.41}$$

$$\begin{aligned} \nu^{(2)} = {} & \frac{\gamma}{2}\left[\frac{\gamma h}{\Delta W}\right]\left[\frac{1-y}{\sqrt{1-x+x^2}-(1-x)} + \frac{\frac{1}{4}(1+y)(1+w)}{\sqrt{1-x+x^2}-\sqrt{1+x^2}}\right]\left[N(N+1)-m_N^2\right] \\ & + \frac{\gamma}{2}\left[\frac{\gamma h}{\Delta W}\right]\left[\frac{\frac{1}{4}(1+y)(1+w)}{\sqrt{1-x+x^2}-\sqrt{1+x^2}}\right] m_N \end{aligned} \tag{2.42}$$

where $g'_F(x)$ and $g''_F(x)$ are defined in Eqs. 2.34 and 2.35, and

$$\Delta W = \text{hyperfine separation} = 2Ah$$

$$x = \frac{g_S \mu_o H_o}{\Delta W} \tag{2.43}$$

$$y = \frac{1 - 2x}{2\sqrt{1 - x + x^2}} \tag{2.44}$$

$$w = \frac{x}{\sqrt{1+x^2}} \tag{2.45}$$

The effects of these terms on the molecular spectrum are discussed in section 2.4.

2.4 Molecular Magnetic Resonance Spectrum

As we have observed, the molecular spin-rotation interaction adds a substructure to the atomic Zeeman resonance. Equation 2.20 and, more exactly, Eq. 2.33 predict a number of lines, one for each value of m_N, spaced equally and symmetrically about the Zeeman frequency. However, each m_N-line contains contributions from molecules in various rotation-vibration states; therefore, the dependence of γ on molecular state, and the number of molecules in each state, affect the shapes and positions of the lines. Furthermore, the transition frequencies are correctly given not by Eq. 2.33, but by Eq. 2.39, making the interpretation of the spectrum even more difficult. A computer becomes essential for modelling the spectrum. The results of computer calculations are given in Chapter 5; however, the qualitative discussion in this section is an aid to understanding the individual effects.

A. Effect of Vibrational and Rotational Temperatures

Each spectral line, specified by a particular value of m_N, contains contributions from molecules in all (N, v) states with $N \geq m_N$. The states are not equally populated, however; to the extent that the distribution can be characterized by temperature, the probability of a molecule being in a state (N, m_N, v) is proportional to the Boltzmann factor $\exp\left(-\frac{E(N)}{kT_N} - \frac{E_N(v)}{kT_v}\right)$, where E(N) is the energy of the state (N, 0), $E_N(v)$ is the energy of the state (N, v) with respect to the state (N, 0), and T_N is the rotational temperature and T_v the vibrational temperature of the beam. The dependence of E(N) on m_N is entirely negligible here. For a low-temperature beam the higher (N, v) states will be significantly less populated than the lower ones, causing a characteristic decrease in peak heights with increasing m_N. (Even if all states were equally populated, corresponding to a high temperature, the peak heights would decrease with increasing $|m_N|$ because fewer N states contribute to the higher m_N-peaks; a low molecular temperature quickens this decrease.)

The rotational and vibrational temperatures affect the shape of each peak as well as its height through the radial dependence of γ. This is discussed in sections 2.4B and C.

B. Dependence of γ on Molecular State

While Bouchiat's experiments and Herman's calculation suggest that the spin-rotation coupling arises from a short-range interaction, the exact functional dependence of γ upon the atomic separation has not been determined. It is convenient to assume a power law for γ:

$$\gamma(R) = \gamma_o\left(\frac{R_m}{R}\right)^n \qquad (2.46)$$

The value of γ to be used in Eq. 2.39 is the expectation value of $\gamma(R)$ in the molecular state (N, v). The expectation values for several values of n have been calculated by Goldhor (GOL72A) for the Baylis KAr potential. The values of $\langle(\frac{R}{R_m})^{-6}\rangle$ and $\langle(\frac{R}{R_m})^{-12}\rangle$ are plotted in Figs. 2-6 and 2-7, respectively, as functions of N for several values of the vibrational quantum number v. It will be seen that $\langle R^{-n}\rangle$ generally decreases with increasing v and N. The exception occurs for R^{-12}, where the expectation value increases with v for small values of N and v: the strong power dependence emphasizes the contribution of small values of R sampled by

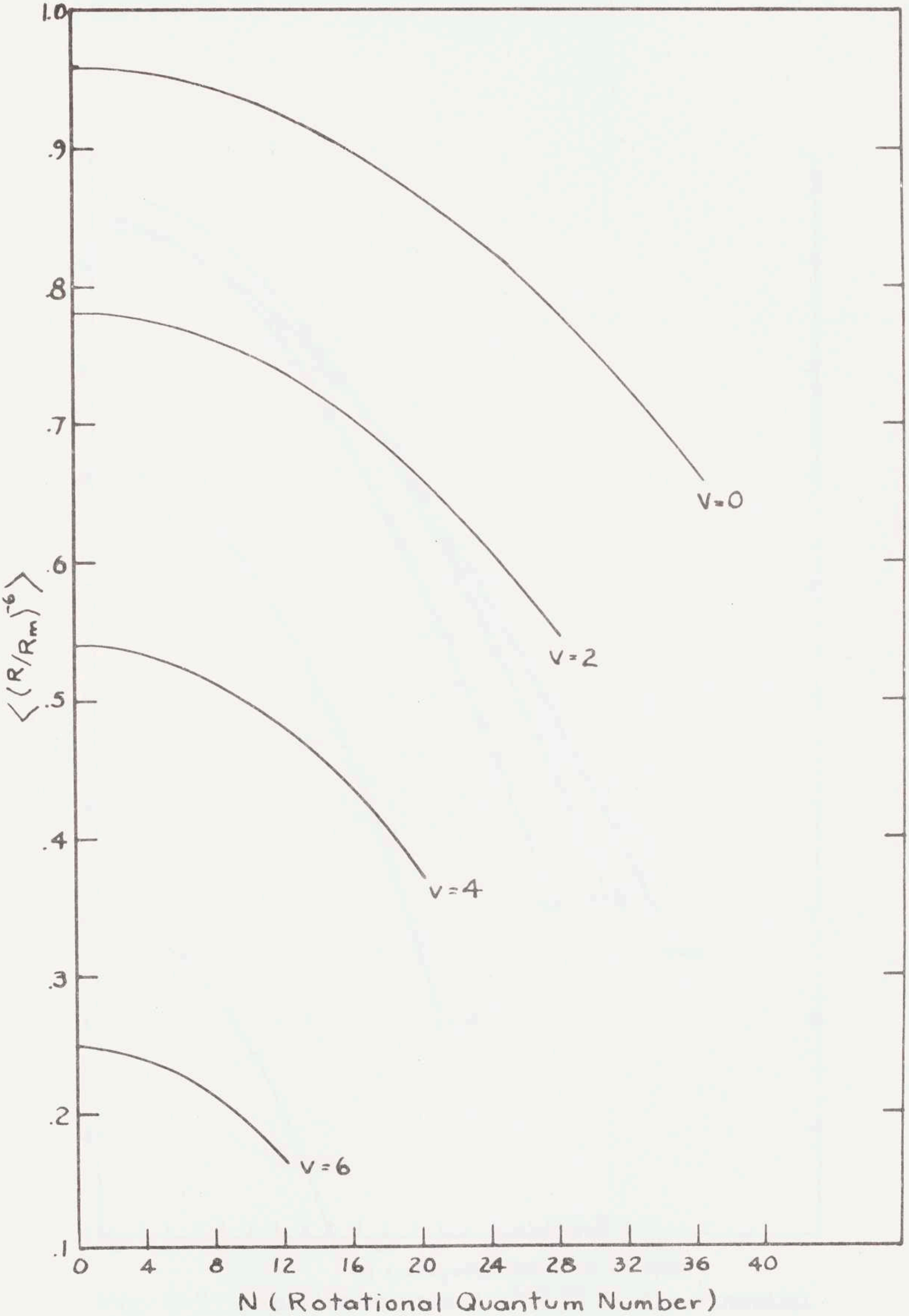

Fig. 2-6 Expectation Values of R^{-6} in KAr Potential.

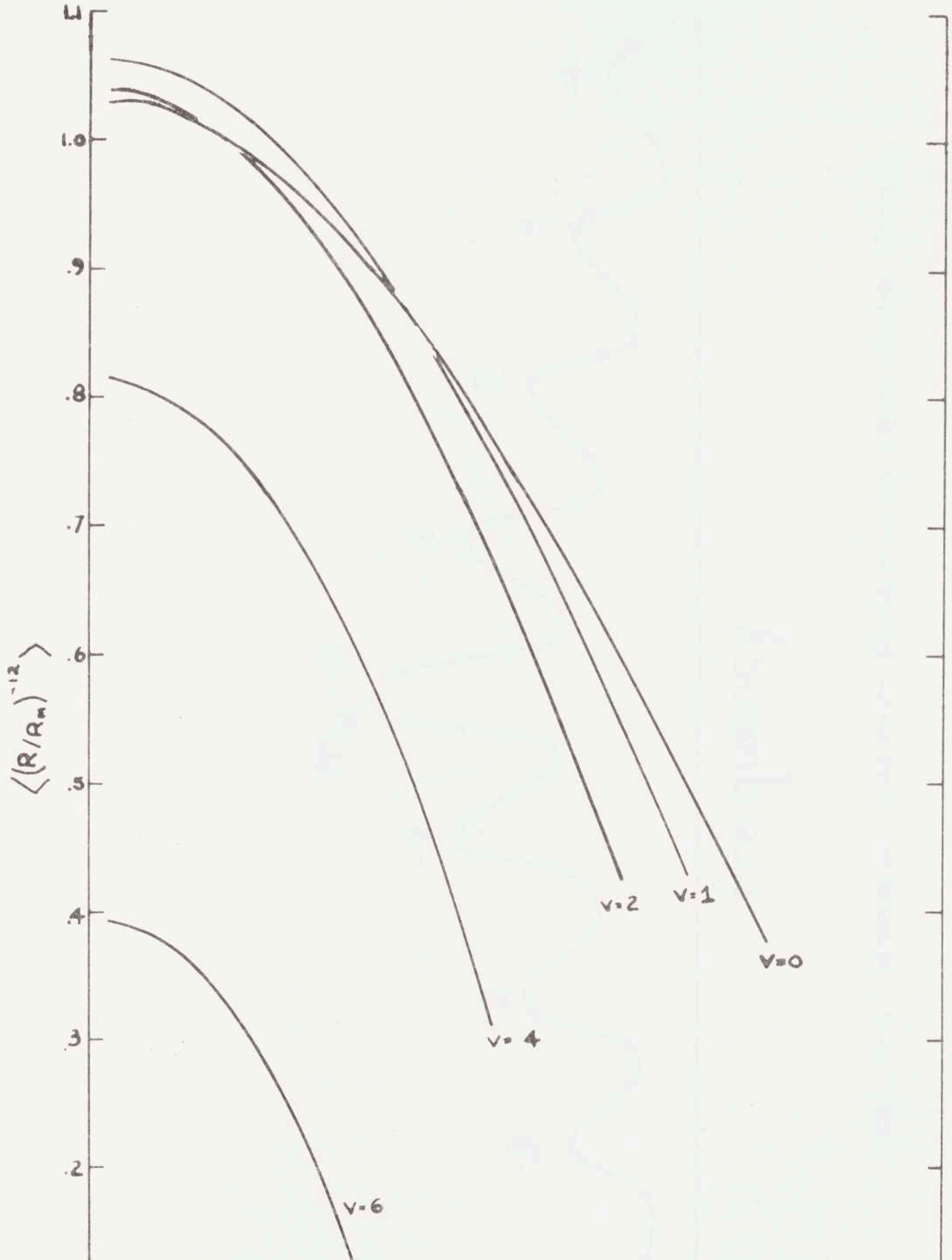

Fig. 2-7 Expectation Values of R^{-12} in KAr Potential.

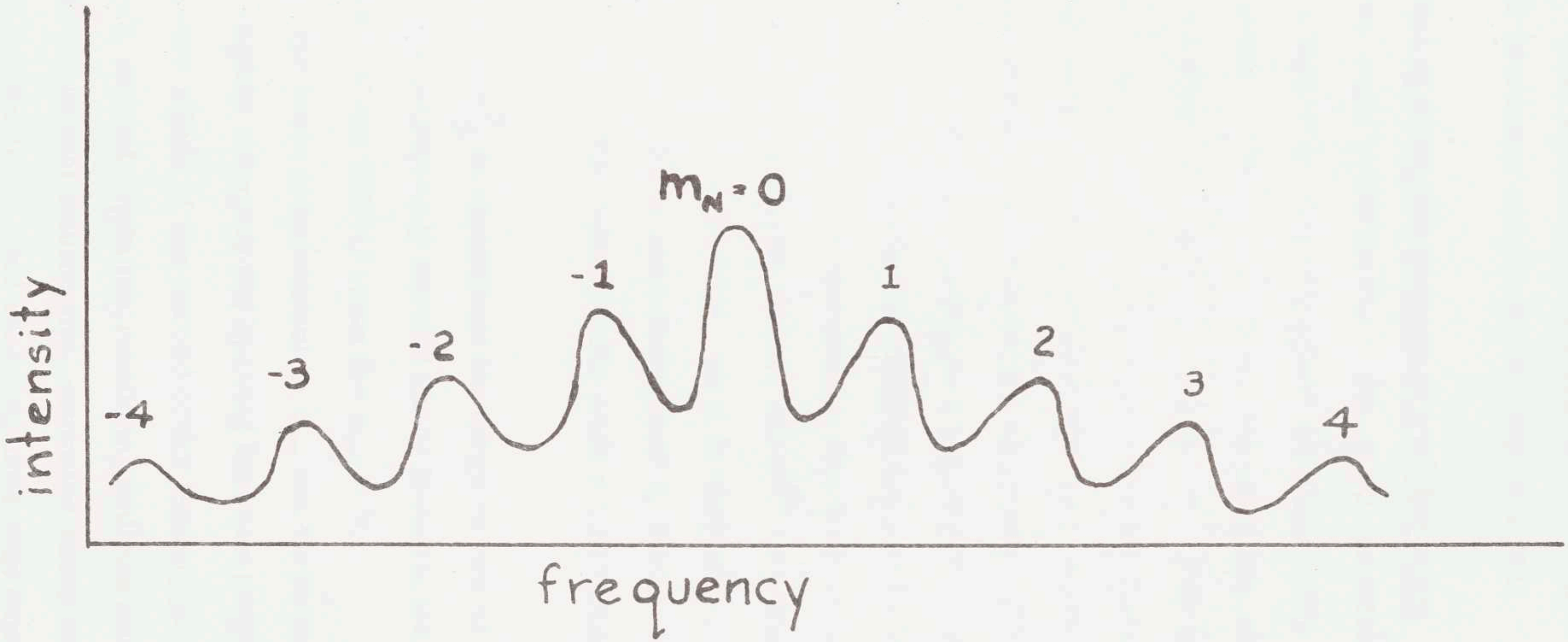

Fig. 2-8 Molecular Spectrum Predicted by First-Order Theory.

these states. This reflects the fact that $\langle R^{-n} \rangle \neq \langle R \rangle^{-n}$; Goldhor has shown that $\langle R \rangle$ increases monotonically with N and v.

C. Effect of State-Dependence of γ on Spectrum

The first-order equation for ν, Eq. 2.33, predicts that the decrease of γ with (N, v) skews the spectral peaks symmetrically toward the central Zeeman frequency. The $m_N = 1$ peak, for example, contains contributions from all states except those with $N = 0$. For moderate dependence of γ on R (e.g., $\gamma \propto R^{-6}$), γ is largest for the state $N = 1$. States with higher values of N contribute lines that are closer to the Zeeman frequency; but because these states are successively less populated their lines are less intense, leading to a hypothetical spectrum such as that of Fig. 2-8. The situation is complicated, however, by the second order terms of Eq. 2.42. In particular, the term containing N(N+1) can be significant even at moderate fields: for $\nu^{(0)} = 15$ MHz, $\nu^{(1)} \sim 75$ kHz, and $N = 10$, this term is ~ 20 kHz, so it is certainly comparable to $\nu^{(1)}$ for small m_N. (As will be seen in Chapter 5, the peaks with $|m_N| < 4$ are resolved best.) The N(N+1) term adds a high-frequency tail on to each peak.

The term in m_N^2 is significant for large values of m_N. It shifts the spectrum asymmetrically toward lower frequencies, and tends to cancel the effect of the N(N+1) term for $m_N \cong N$.

Finally, the term proportional to m_N can be included with the first-order term, slightly changing the spacing between peaks.

The precise effect of the second order terms, particularly of the term in N(N+1), depends upon the rotational and vibrational temperatures, and is difficult to predict intuitively; computer simulations of the spectrum are presented in Chapter 5, and are compared with experimental data.

2.5 Calculation of the Spin-Rotation Constant

In the past fifteen years a great deal of work has been done on the relaxation of optically pumped alkali vapor in cells filled with rare gas. The quantity most frequently measured is the disorientation cross section σ. The cross section for depolarization of the alkali ground state is many orders of magnitude smaller than the kinetic cross section $\sigma_{kin} \sim 10^{-16}$ cm^2. In 1962, Bernheim (BER62) proposed the spin-rotation interaction as a mechanism for disorientation. Extending Bernheim's idea, Herman (HER64) has shown that the spin-rotation energy is dominated by a short-range, second-order interaction. He calculated values of σ for Rb--rare-gas relaxation that agree within a factor of two with measured values quoted in his paper. Soboll (SOB69) has used Herman's method to calculate σ for Na--rare-gas combinations and has obtained results that also agree well with experiment. The short-range nature of the interaction has been confirmed by Bouchiat's results (BOU69); however, the value for γ_{RbKr} calculated from Herman's data is about seven times that measured by Bouchiat.

We should like to compare Herman's calculation with our results. Obtaining a theoretical value for γ requires some rough estimates for certain quantities; as we shall see, the result is a value which is larger than our experimentsl results by a factor of about ten.

Herman considers a second-order spin-rotation hamiltonian

$$\mathcal{H} = \gamma'(R)\, \vec{N}' \cdot \vec{S}'/I(R) \qquad (2.47)$$

where $\vec{N}'$ = rotational angular momentum of molecule

$\vec{S}'$ = electron spin angular momentum

$I(R)$ = moment of inertia of molecule

γ' is dimensionless; it is related to our parameter γ by

$$\gamma = \gamma' \hbar / 2\pi I \tag{2.48}$$

with

$$I = \mu R^2 \tag{2.49}$$

Herman considers two effects which lead to a spin-rotation interaction in the close approach of an alkali and a rare-gas atom: overlap, in which the exclusion principle requires the molecular wave functions to be antisymmetrized with respect to interchange of electron coordinates, and deformation of the ground states of the atoms. Deformation is caused by long-range Coulomb interactions, which are responsible for the van der Waals force, and by short-range interactions that yield first-order repulsive energies without leading to correlation of the instantaneous positions of the electrons in the two atoms. Herman has calculated the spin-rotation constant for RbHe and RbNe. He finds that the short-range contribution to γ' in RbNe is approximately twenty times the overlap contribution, while in RbHe it is 10^4 times the long-range contribution. Applying Herman's methods to KAr, I have found that the short-range component of γ' is roughly 10^4 times the long-range component. These calculations indicate that long-range and overlap contributions to γ' can be ignored.

When the alkali is deformed, a fraction Λ of the ^2P state is mixed into its wavefunction. By a variational calculation Herman shows that $\Lambda(R)$ is related to $E_{SR}(R)$, the short-range repulsive interatomic energy by

$$\Lambda(R_o) \approx - \frac{E_{SR}(R_o)}{\sqrt{E_H \overline{E}}} \frac{R_o}{a_o} \tag{2.50}$$

where E_H = ionization potential of hydrogen = 13.6 eV

a_o = first Bohr radius = 0.52×10^{-8} cm

R_o = distance of closest approach of atoms

E_{SR} = short-range interaction energy

$\overline{E}$ = energy of alkali P state

He finds for the short-range component of γ',

$$\gamma'(R_o)_{\text{short range}} \approx \frac{4}{3}\Lambda^2(R_o)\left[1 - \frac{\overline{E}}{E_{av}}\right]\frac{E_{so}}{\overline{E}} \tag{2.51}$$

where E_{so} = fine-structure splitting of alkali P state

E_{av} = average of $\overline{E}$ and the alkali ionization energy E_I:

$$E_{av} = (\overline{E} + E_I)/2$$

For KAr we take R_o to be equal to R_m; Baylis (BAY69) gives

$$R_m = 9.9\ a_o$$

Moore (MOO71) gives the following values for potassium:

$$E_I = 4.34 \text{ eV}$$

$$\overline{E} = 1.61 \text{ eV}$$

$$E_{so} = 7.16 \times 10^{-3} \text{ eV}$$

Thus we have $E_{av} = 2.98$ eV.

The difficulty in evaluating Eqs. 2.50 and 2.51 comes in obtaining a value for $E_{SR}(R_m)$. Herman uses a scaling argument to estimate E_{SR} for the interaction of rubidium with rare gases. He assumes that the long- and short-range energies bear a constant ratio at a given radius, so that, knowing the van der Waals constant for the Rb--rare-gas combinations, and having calculated E_{SR} for RbHe, he can find E_{SR} for the other combinations. For KAr we shall use a similar type of scaling argument to find E_{SR}, but shall begin by obtaining E_{SR} for KHe from an experimental measurement of σ.

If we break up the Lennard-Jones potential of Eq. 2.7 into long- and short-range parts we have

$$V_{LR} = -2\,\epsilon(R/R_m)^{-6} \tag{2.52}$$

$$V_{SR} = \epsilon(R/R_m)^{-12} \tag{2.53}$$

Thus at $R = R_m$, the short-range energy scales with the well depth ϵ.

The disorientation cross section for KHe has been measured by Bernheim (BER65):

$$\sigma_{(KHe)} = 1.1 \times 10^{-25}\ \text{cm}^2 \tag{2.54}$$

Herman (HER64) finds that

$$\sigma = \gamma'^2(R_o)\,\sigma_{kin}/12 \tag{2.55}$$

where

$$\sigma_{kin} = \pi R_o^2 = \text{kinetic cross section} \tag{2.56}$$

With $R_o = 11\ a_o = 5.72 \times 10^{-8}$ cm (BAY69) we have

$$\gamma'_{KHe} = 1.12 \times 10^{-5} \tag{2.57}$$

Using Eq. 2.50 and 2.51 this leads to

$$\Lambda_{KHe} = 6.4 \times 10^{-2} \tag{2.58}$$

and

$$E_{SR}(\mathrm{KHe}) = 2.63 \times 10^{-2}\ \mathrm{eV} \tag{2.59}$$

Since $E_{SR}(R_m)$ scales with ϵ, and since $\epsilon_{KHe} = 3.0\ \mathrm{cm}^{-1}$ and $\epsilon_{KAr} = 42\ \mathrm{cm}^{-1}$ (BAY69), we have

$$\begin{aligned} E_{SR}(\mathrm{KAr}) &= \frac{42}{3} \times 2.63 \times 10^{-2} \\ &= 0.368\ \mathrm{eV} \end{aligned} \tag{2.60}$$

Again using Eqs. 2.51 and 2.50 we obtain for KAr

$$\Lambda_{KAr} = 0.78 \tag{2.61}$$

$$\gamma'_{KAr} = 1.69 \times 10^{-3} \tag{2.62}$$

Then Eqs. 2.48 and 2.49, with $R_m = 5.2 \times 10^{-8}$ cm, give

$$\gamma_{KAr} = 3.14\ \mathrm{MHz} \tag{2.63}$$

This is approximately ten times larger than the value measured in this experiment (see Chapter 5).

As a check on the calculation, we can compute γ_{RbKr} from Herman's data, and compare it with Bouchiat's measurements. For Rb, $\overline{E} = 1.58$ eV, $E_{so} = 3.0 \times 10^{-2}$ eV, and $E_{av} = 2.88$ eV (MOO71). (Herman claims $E_{av} = 3.38$ eV; however, the ionization potential of Rb (MOO71) is 4.18 eV, leading to $E_{av} = (1.58 + 4.18)/2 = 2.88$ eV.) Using these values, plus $R_o = 7.8\ a_o$ (cf. $R_m = 10\ a_o$ given by Baylis) and $E_{SR} = 0.301$ eV given by Herman, one finds

$$\Lambda_{RbKr} = 0.504 \tag{2.64}$$

$$\gamma'_{RbKr} = 2.9 \times 10^{-3} \tag{2.65}$$

$$I = 11.6 \times 10^{-38} \text{ gr. cm}^2 \tag{2.66}$$

$$\gamma_{RbKr} = 4.25 \text{ MHz} \tag{2.67}$$

This may be compared with $\gamma_{RbKr} = 0.64$ MHz measured by Bouchiat (BOU69). The calculations of γ after Herman are consistently larger than experimental values by approximately an order of magnitude. On the other hand, Herman's calculations agree quite well with disorientation cross section measurements. The discrepancy may be due to the fact that the cross sections are measured in experiments that are most sensitive to two-body "sudden" collisions, in which the partners approach each other closer than R_m and therefore experience large short-range forces, while in molecular formation the atoms spend most of their time at greater distances and experience weaker short-range force. If that is the case, it would seem that Herman's calculation is more applicable to interactions in fast collisions than in molecules; however, the roughness of the calculations makes a definite conclusion impossible.

APPENDIX A2.1

MOLECULAR ENERGY LEVELS IN LOW MAGNETIC FIELDS

In a low magnetic field, such that $g_S\mu_o \vec{S}\cdot\vec{H}_o \ll \gamma h \vec{S}\cdot\vec{N}$, the molecular angular momenta couple in the hierarchy $\vec{F} = \vec{I} + \vec{S}$, $\vec{J} = \vec{F} + \vec{N}$. The hamiltonian of Eq. 2.13 can then be written

$$\mathcal{H} = h(a+\alpha)\vec{I}\cdot\vec{S} + \gamma h \frac{\vec{S}\cdot\vec{F}}{F^2}\vec{F}\cdot\vec{N} + g_S\mu_o \frac{\vec{S}\cdot\vec{F}\vec{F}.\vec{J}}{F^2 J^2}\vec{J}\cdot\vec{H}_o \qquad (A2.1/1)$$

The eigenvalues are

$$\begin{aligned} E_{I,S,F,N,J,m_J} &= h(a+\alpha)\frac{[F(F+1)-I(I+1)-S(S+1)]}{2} \\ &+ h\gamma\left[\frac{F(F+1)+S(S+1)-I(I+1)}{2F(F+1)}\right]\left[\frac{J(J+1)-F(F+1)-N(N+1)}{2}\right] \\ &+ g_S\mu_o\left[\frac{F(F+1)+S(S+1)-I(I+1)}{2F(F+1)}\right] \\ &\times\left[\frac{J(J+1)+F(F+1)-N(N+1)}{2J(J+1)}\right] m_J H_o \end{aligned} \qquad (A2.1/2)$$

For I = 3/2, S = 1/2, and N = 1 (the simplest non-trivial case in KAr) the possible values of F and J are

$F = 2,\ J = 3,\ 2,\ 1$

$F = 1,\ J = 2,\ 1,\ 0$

From Eq. A2.1/2 we obtain

F	J	$E_{FJm_J}(N=1)$
2	3	$\frac{3}{4}(a+\alpha)h + \frac{1}{2}h\gamma + \frac{1}{6}g_S\mu_oH_om_J$
	2	$\frac{3}{4}(a+\alpha)h - \frac{1}{4}h\gamma + \frac{5}{24}g_S\mu_oH_om_J$
	1	$\frac{3}{4}(a+\alpha)h - \frac{3}{4}h\gamma + \frac{3}{8}g_S\mu_oH_om_J$
1	2	$-\frac{5}{4}(a+\alpha)h - \frac{1}{4}h\gamma - \frac{1}{8}g_S\mu_oH_om_J$
	1	$-\frac{5}{4}(a+\alpha)h + \frac{1}{4}h\gamma - \frac{1}{8}g_S\mu_oH_om_J$
	0	$-\frac{5}{4}(a+\alpha)h + \frac{1}{2}h\gamma - \frac{1}{8}g_S\mu_oH_om_J$

It will be noticed that the Zeeman energies for all states with F = 1 are equal. This reflects the fact that for F = N the spin g-factor is independent of J, as shown by the last term of Eq. A2.1/2.

APPENDIX A2.2

MOLECULAR ENERGY LEVELS IN INTERMEDIATE MAGNETIC FIELDS

Using second order perturbation theory we solve for the energy levels of the hamiltonian

$$\mathcal{H} = \mathcal{H}_o + \mathcal{H}' \qquad \text{(A2.2/1)}$$

where

$$\mathcal{H}_o = Ah\,\vec{I}\cdot\vec{S} + g_S\mu_o H_o S_z \qquad \text{(A2.2/2)}$$

and

$$\mathcal{H}' = \gamma h\,\vec{S}\cdot\vec{N} = \gamma h\, S_z N_z + \frac{\gamma h}{2}(S_+N_- + S_-N_+) \qquad \text{(A2.2/3)}$$

A. Unperturbed eigenvalues and eigenvectors

The eigenvalues and eigenvectors of $\mathcal{H}_o$ may be calculated readily in the basis N, m_N, I, m_I, S, m_S. Because $\mathcal{H}_o$ commutes with the operators N^2, I^2, S^2, N_z, and $F_z = I_z + S_z$, the good quantum numbers are N, m_N, I, S, and $m_F = m_I + m_S$. As H_o approaches zero the energy levels continuously approach the eigenvalues of $Ah\,\vec{I}\cdot\vec{S}$, for which F is a good quantum number: consequently we may label the energy levels of $\mathcal{H}_o$ by F and m_F at all fields. As discussed by Ramsey (RAM56, p. 86), for $S = \frac{1}{2}$ the $\mathcal{H}_o$-matrix breaks up into a series of 2 x 2 submatrices, corresponding to values of m_F between $|I - \frac{1}{2}|$ and $-|I - \frac{1}{2}|$. The two submatrices for $m_F = \pm(I + \frac{1}{2})$ are of order 1 x 1. Labelling the basis states by (m_I, m_S), with $m_S = +\frac{1}{2}$ and $-\frac{1}{2}$ indicated by $\uparrow$ and $\downarrow$, a typical submatrix, with $m_F = m$, is

$$\begin{array}{ccc} & (m - \frac{1}{2}, \uparrow) & (m + \frac{1}{2}, \downarrow) \\ (m - \frac{1}{2}, \uparrow) & \frac{1}{2}Ah(m-\frac{1}{2}) + \frac{1}{2}g_S\mu_o H_o & \frac{1}{2}Ah\sqrt{I(I+1)-m^2+\frac{1}{4}} \\ (m + \frac{1}{2}, \downarrow) & \frac{1}{2}Ah\sqrt{I(I+1) - m^2 + \frac{1}{4}} & -\frac{1}{2}Ah(m+\frac{1}{2})-\frac{1}{2}g_S\mu_o H_o \end{array} \qquad \text{(A2.2/4)}$$

Solving the secular equation of A2.2/4 we find the eigenvalues

$$\lambda_{\pm,m} = -\frac{\Delta W}{2(2I+1)} \pm \frac{\Delta W}{2}\sqrt{1 + \frac{4m}{2I+1}x + x^2} \qquad (A2.2/5)$$

where

$$\Delta W = hA(2I+1)/2 = \text{hyperfine separation} \quad (A2.2/6)$$

$$x = g_S\mu_o H_o/\Delta W \; (= \mu_o H_o/A \text{ for } I = \tfrac{3}{2})$$

and

$$\pm \Rightarrow F = I \pm \tfrac{1}{2} \; (= 2,\ 1 \text{ for } I = \tfrac{3}{2})$$

Equation A2.2/5 is just the Breit-Rabi formula. For potassium $I = 3/2$, so $2I+1 = 4$, and

$$\lambda_{\pm,m} = -Ah/4 \pm AhZ_m \qquad (A2.2/7)$$

where

$$Z_m = \sqrt{1 + mx + x^2} \qquad (A2.2/8)$$

Diagonalizing the matrix A2.2/4, using the eigenvalues A2.2/7, one finds the eigenvectors $\beta_{F,m}$:

$$\beta_{2,m} = \frac{P_m^+}{\sqrt{Y_m^2 + (P_m^+)^2}}\,|m-\tfrac{1}{2},\uparrow\rangle + \frac{Y_m}{\sqrt{Y_m^2 + (P_m^+)^2}}\,|m+\tfrac{1}{2},\downarrow\rangle$$

(A2.2/9)

$$\beta_{1,m} = \frac{P_m^-}{\sqrt{Y_m^2 + (P_m^-)^2}}\,|m-\tfrac{1}{2},\uparrow\rangle + \frac{Y_m}{\sqrt{Y_m^2 + (P_m^-)^2}}\,|m+\tfrac{1}{2},\downarrow\rangle$$

(A2.2/10)

where

$$Y_m = \sqrt{1 - \frac{m^2}{4}} \qquad (A2.2/11)$$

$$P_m^{\pm} = \tfrac{1}{2}m + x \pm \sqrt{1 + mx + x^2} \qquad (A2.2/12)$$

In the next sections we will need only $\beta_{F,m}$ with m = -2, -1, and 0. Evaluating the coefficients of these states we find

$$\beta_{2,0} = \sqrt{(1+w)/2}\ |-\tfrac{1}{2},\uparrow\rangle + \sqrt{(1-w)/2}\ |\tfrac{1}{2},\downarrow\rangle \qquad \text{(A2.2/13)}$$

$$\beta_{2,-1} = \sqrt{(1-y)/2}\ |-3/2,\uparrow\rangle + \sqrt{(1+y)/2}\ |-\tfrac{1}{2},\downarrow\rangle \qquad \text{(A2.2/14)}$$

$$\beta_{2,-2} = |-3/2,\downarrow\rangle \qquad \text{(A2.2/15)}$$

where

$$y = \frac{1-2x}{2\,Z_{-1}} = \frac{1-2x}{2\sqrt{1-x+x^2}} \qquad \text{(A2.2/16)}$$

$$w = x/Z_o = x/\sqrt{1+x^2} \qquad \text{(A2.2/17)}$$

The energies of these states are

$$E_{2,0} = Ah(-\tfrac{1}{4} + \sqrt{1+x^2}) \qquad \text{(A2.2/18)}$$

$$E_{2,-1} = Ah(-\tfrac{1}{4} + \sqrt{1-x+x^2}) \qquad \text{(A2.2/19)}$$

$$E_{2,-2} = Ah(\tfrac{3}{4} - x) \qquad \text{(A2.2/20)}$$

B. Perturbation Calculation

Because $\mathcal{H}_o$ does not contain N^2 or N_z, the eigenvectors β_{F,m_F} are states of good N, m_N, as well as good m_F. When $\mathcal{H}'$ is added to $\mathcal{H}_o$ the resulting hamiltonian does not conserve either m_N or m_F, but does conserve the quantity $M = m_N + m_I + m_S = m_F + m_N$. Consequently $\mathcal{H}$ does not have matrix elements between states of different total magnetic quantum number M, and the $\mathcal{H}$ matrix breaks up into a series of 8 x 8 submatrices, each with a different value of M. A typical such matrix is shown in Fig. A2.2-1. The states are labelled $\beta^{m_N}_{F,m_F}$, with $m_N = M - m_F$.

	$\beta^{M+2}_{2,-2}$	$\beta^{M+1}_{2,-1}$	$\beta^{M}_{2,0}$	$\beta^{M-1}_{2,1}$	$\beta^{M-2}_{2,2}$	$\beta^{M+1}_{1,-1}$	$\beta^{M}_{1,0}$	$\beta^{M-1}_{1,1}$
$\beta^{M+2}_{2,-2}$	$\lambda_{2,-2}+D^{M+2}_{2,-2}$	${}_{-2,-1}G$				${}_{-2,-1}K$		
$\beta^{M+1}_{2,-1}$	${}_{-1,-2}G$	$\lambda_{2,-1}+D^{M+1}_{2,-1}$	${}_{-1,0}G$			${}_{-1}L^{M+1}$	${}_{-1,0}K$	
$\beta^{M}_{2,0}$		${}_{0,-1}G$	$\lambda_{2,0}+D^{M}_{2,0}$	${}_{0,1}G$		${}_{0,-1}K$	${}_{0}L^{M}$	${}_{0,1}K$
$\beta^{M-1}_{2,1}$			${}_{1,0}G$	$\lambda_{2,1}+D^{M-1}_{2,1}$	${}_{1,2}G$		${}_{1,0}K$	${}_{1}L^{M-1}$
$\beta^{M-2}_{2,2}$				${}_{2,1}G$	$\lambda_{2,2}+D^{M-2}_{2,2}$			
$\beta^{M+1}_{1,-1}$	${}_{-1,-2}K$	${}_{-1}L^{M+1}$	${}_{-1,0}K$			$\lambda_{1,-1}+D^{M+1}_{1,-1}$	${}_{-1,0}Q$	
$\beta^{M}_{1,0}$		${}_{0,-1}K$	${}_{0}L^{M}$	${}_{0,1}K$		${}_{0,-1}Q$	$\lambda_{1,0}+D^{M}_{1,0}$	${}_{0,1}Q$
$\beta^{M-1}_{1,1}$			${}_{1,0}K$	${}_{1}L^{M-1}$			${}_{0,1}Q$	$\lambda_{1,1}+D^{M-1}_{1,1}$

Fig. A2.2-1 Hamiltonian Submatrix with Total Magnetic Quantum Number M.
(Basis States $\beta^{m_N}_{F,m_F}$)

The matrix elements in this matrix are indicated schematically. The quantities λ_{F,m_F} are the eigenvalues of $\mathcal{H}_o$ given by Eq. A2.2/7. The other matrix elements are best explained by dividing the perturbing hamiltonian into two parts:

$$\mathcal{H}' = \mathcal{H}'_1 + \mathcal{H}'_2 \qquad \text{(A2.2/21)}$$

$$\mathcal{H}'_1 = \gamma h S_z N_z \qquad \text{(A2.2/22)}$$

$$\mathcal{H}'_2 = \tfrac{1}{2}\gamma h(S_+N_- + S_-N_+) \qquad \text{(A2.2/23)}$$

$\mathcal{H}_1'$ conserves all quantum numbers and therefore has matrix elements only between states with the same quantum numbers. However, because F is not actually a good quantum number, but only a label, $\mathcal{H}_1'$ can have matrix elements between states with different values of F; these are designated ${}_{m_F}L^{m_N}$. The matrix elements of $\mathcal{H}_1'$ between states of constant F are called $D^{m_N}_{F,m_F}$.

$\mathcal{H}_2'$ has no diagonal elements, but does have matrix elements between states with the same value of $(m_N + m_S)$, and because $\mathcal{H}_2'$ is diagonal in m_I we can equally say that it has matrix elements between states of constant $(m_N + m_F)$. Furthermore, its only non-zero matrix elements are between states with m_F (m_N) differing by ± 1 (∓ 1). Matrix elements of $\mathcal{H}_2'$ between states with F = 2 are designated ${}_{m_{F_1},m_{F_2}}G$; those between states with F = 1, ${}_{m_{F_1},m_{F_2}}Q$; and those between states with F = 2 and F = 1, ${}_{m_{F_1},m_{F_2}}K$.

We wish to find the effect of $\mathcal{H}'$ on the frequency of the transition between the states (F = 2, $m_F = -1$, m_N) and (F = 2, $m_F = -2$, m_N). To do this we calculate the changes in the energies of these states, using first- and second-order perturbation theory. Labelling the levels by m_F we write

$$W_{m_F} = W^{(0)}_{m_F} + W^{(1)}_{m_F} + W^{(2)}_{m_F} \qquad \text{(A2.2/24)}$$

where the superscript indicates the order of the perturbation. $W^{(0)}_{m_F}$ is the energy level of the unperturbed hamiltonian $\mathcal{H}_o$.

(i) <u>First Order Perturbation</u>

(a) $m_F = -2$

The basis states are labelled $|m_N, m_I, m_S\rangle$, with N, I, and S understood. Only $\mathcal{H}_1'$ contributes to $W^{(1)}_{m_F}$.

$$W^{(1)}_{-2} = \langle \beta^{m_N}_{2,-2} | \mathcal{H}'_1 | \beta^{m_N}_{2,-2} \rangle = \langle m_N, -3/2, | \gamma h\, S_z N_z \, | m_N, -3/2, \rangle$$

$$W^{(1)}_{-2} = -\tfrac{1}{2}\gamma h m_N \qquad \text{(A2.2/25)}$$

(b) $m_F = -1$

$$W^{(1)}_{-1} = \langle \beta^{m_N}_{2,-1} | \mathcal{H}'_1 | \beta^{m_N}_{2,-1} \rangle$$

From Eq. A2.2/14,

$$W^{(1)}_{-1} = \Big\{ \sqrt{\tfrac{1-y}{2}} \;\langle m_N, -3/2, \uparrow | + \sqrt{\tfrac{1+y}{2}} \;\langle m_N, -\tfrac{1}{2}, \downarrow | \; |\gamma S_z N_z|$$

$$\times \; \sqrt{\tfrac{1-y}{2}} \;| m_N, -3/2, \uparrow \rangle + \sqrt{\tfrac{1+y}{2}} \;| m_N, -\tfrac{1}{2}, \downarrow \rangle \Big\}$$

$$= -\tfrac{1}{2}\gamma h m_N\, y \qquad \text{(A2.2/26)}$$

$$W^{(1)}_{-1} = \left[\frac{2x - 1}{2\sqrt{1-x+x^2}} \right] \frac{\gamma h}{2}\, m_N \qquad \text{(A2.2/27)}$$

(ii) Second Order Perturbation

The second order correction to the energy of the state $|0\rangle$ is given by

$$W^{(2)}_0 = \sum_{\substack{k \\ k \neq 0}} \frac{|\langle 0 | \mathcal{H}' | k \rangle|^2}{E_0 - E_k} \qquad \text{(A2.2/28)}$$

where E_0 and E_k are the energies of the unperturbed states $|0\rangle$ and $|k\rangle$. Because we are concerned with relatively low magnetic fields ($x < 1$), the energy differences between states with $F = 2$ are of the order of the Zeeman energy, while those between states with $F = 2$ and $F = 1$ are of the order of the hyperfine separation. We will therefore ignore the contribution to $W^{(2)}_{m_F}$ of the matrix elements between states of different F, that is, the matrix elements labelled K in Fig. A.2.2-1. As discussed previously, only $\mathcal{H}'_2$ gives non-zero second-order matrix elements.

(a) $\underline{m_F = -2}$

$$W^{(2)}_{-2} = \frac{|\langle \beta^{m_N}_{2,-2} | \mathcal{H}'_2 | \beta^{m_N - 1}_{2,-1} \rangle|^2}{E_{2,-2} - E_{2,-1}} \qquad \text{(A2.2/29)}$$

From Eqs. A2.2/14 and 15 we have

$$W^{(2)}_{-2} = \frac{\left| \left\langle m_N, -\tfrac{3}{2}, \downarrow \right| \frac{\gamma h}{2}(S_+N_- + S_-N_+) \left| \sqrt{\tfrac{1-y}{2}}\, \left|m_N - 1, -\tfrac{3}{2}, \uparrow\right\rangle + \sqrt{\tfrac{1+y}{2}}\, \left|m_N - 1, -\tfrac{1}{2}, \downarrow\right\rangle \right|^2}{E_{2,-2} - E_{2,-1}}$$

$$= \left(\frac{\gamma h}{2}\right)^2 \left(\frac{1-y}{2}\right) \left| \left\langle m_N, -\tfrac{3}{2}, \downarrow \right| S_-N_+ \left| m_N - 1, -\tfrac{3}{2}, \uparrow \right\rangle \right|^2 \Big/ (E_{2,-2} - E_{2,-1})$$

$$W^{(2)}_{-2} = \frac{\left(\frac{\gamma h}{2}\right)^2 \left(\frac{1-y}{2}\right) \left[N(N+1) - (m_N - 1)m_N\right]}{E_{2,-2} - E_{2,-1}} \qquad \text{(A2.2/30)}$$

(b) $\underline{m_F = -1}$

$$W^{(2)}_{-1} = \frac{|\langle \beta^{m_N}_{2,-1} | \mathcal{H}'_2 | \beta^{m_N + 1}_{2,-2} \rangle|^2}{E_{2,-1} - E_{2,-2}} + \frac{|\langle \beta^{m_N}_{2,-1} | \mathcal{H}'_2 | \beta^{m_N - 1}_{2,0} \rangle|^2}{E_{2,-1} - E_{2,0}}$$

(A2.2/31)

We obtain

$$W^{(2)}_{-1} = \frac{\left(\frac{\gamma h}{2}\right)^2 \left(\frac{1-y}{2}\right) \left[N(N+1) - (m_N + 1)m_N\right]}{E_{2,-1} - E_{2,-2}}$$

$$+ \frac{\left(\frac{\gamma h}{2}\right)^2 \frac{1}{4} (1+y)(1+w) \left[N(N+1) - (m_N - 1)m_N\right]}{E_{2,-1} - E_{2,0}} \qquad \text{(A2.2/32)}$$

C. Transition Energy

The energy of the transition between (m_N, F = 2, m_F = -1) and (m_N, F = 2, m_F = -2) is

$$W = W_{-1} - W_{-2} = (W^{(0)}_{-1} - W^{(0)}_{-2}) + (W^{(1)}_{-1} - W^{(1)}_{-2}) + (W^{(2)}_{-1} - W^{(2)}_{-2}) \tag{A2.2/33}$$

(i) Zeroth Order

$W^{(0)} \equiv W^{(0)}_{-1} - W^{(0)}_{-2}$ is the Zeeman energy of the unperturbed transition,

$$W^{(0)} = g'_F(x)\,\mu_o H_o \tag{A2.2/34}$$

where $g'_F(x)$ is given by Eq. 2.34.

(ii) First Order

From Eqs. A2.2/25 and 27,

$$W^{(1)} \equiv W^{(1)}_{-1} - W^{(1)}_{-2} = \tfrac{1}{2}\left(\frac{\gamma h}{2} m_N\right)\left[\frac{2x - 1}{\sqrt{1-x+x^2}} + 2\right] \tag{A2.2/35}$$

Expanding the quantity in square brackets for x < 1 we obtain, to order x^2,

$$W^{(1)} = \tfrac{1}{2}\left(1 + \frac{3}{2}x + \frac{9}{8}x^2\right)\frac{\gamma h}{2} m_N = g''_F(x)\,\frac{\gamma h}{2} m_N \tag{A2.2/36}$$

This is equivalent to the second term of Eq. 2.33, with $g''(x)$ defined by Eq. 2.35.

(iii) Second Order

$$W^{(2)} \equiv W^{(2)}_{-1} - W^{(2)}_{-2}$$

$$= \frac{\left(\frac{\gamma h}{2}\right)^2 \left(\frac{1-y}{2}\right) \left[2N(N+1) - 2m_N^2\right]}{E_{2,-1} - E_{2,-2}} + \frac{\left(\frac{\gamma h}{2}\right)^2 \frac{1}{4} (1+y)(1+w) \left[N(N+1) - m_N(m_N-1)\right]}{E_{2,-1} - E_{2,0}}$$

$$\begin{aligned} W^{(2)} = \frac{\gamma h}{2}\left[\frac{\gamma h}{\Delta W}\right] \Bigg\{ & \frac{1-y}{\sqrt{1-x+x^2} - (1-x)} \left[N(N+1) - m_N^2\right] \\ & + \frac{\frac{1}{4}(1+y)(1+w)}{\sqrt{1-x+x^2} - \sqrt{1+x^2}} \left[N(N+1) - m_N^2 + m_N\right] \Bigg\} \end{aligned} \qquad \text{(A2.2/37)}$$

CHAPTER 3

APPARATUS

3.1 Introduction

The molecular beam magnetic resonance (MBMR) apparatus used in this experiment is based on the traditional design developed by I. I. Rabi and discussed in detail by Ramsey (RAM56). A brief description of the MBMR technique has been given in Chapter 1. In this chapter we shall describe those aspects of the apparatus which are novel, or which are necessary for understanding the experiment.

A schematic view of the apparatus is shown in Fig. 3-1. Figure 3-2 is a photograph of the machine. A detailed list of dimensions and other data on the apparatus is provided in Appendix A3.1.

Although the apparatus is basically similar to other MBMR machines, many of its features were designed particularly for experiments on van der Waals molecules. The major problems influencing the design were production of the beam and separation of the molecules from a large background of atoms.

The optimum formation rate for molecular clusters in a jet beam occurs with a high stagnation gas pressure and a small nozzle aperture. If the nozzle is too small, however, potassium will condense in it and clog it (CHU72, p. 153). The combination of moderate aperture diameter (0.030 mm) and high gas pressure (35 psia) produces a large gas throughput into the source chamber, requiring large pumping capacity. Potassium can be "pumped" easily by condensation on a water-cooled surface, but the argon requires a high-speed vacuum pump. For this reason, the source chamber is connected directly to a ten-inch oil-

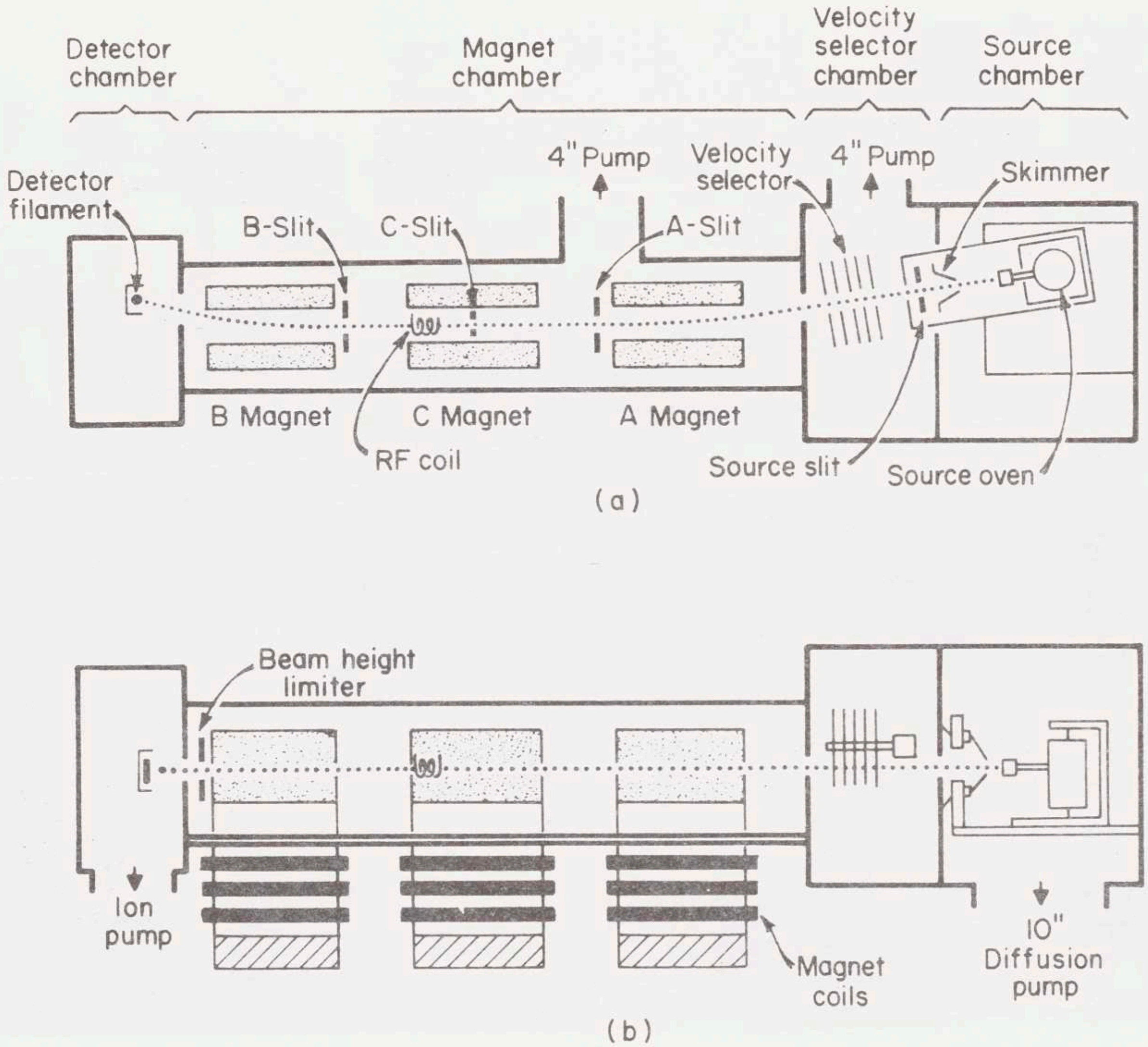

Fig. 3-1 Molecular Beam Apparatus--Schematic View.

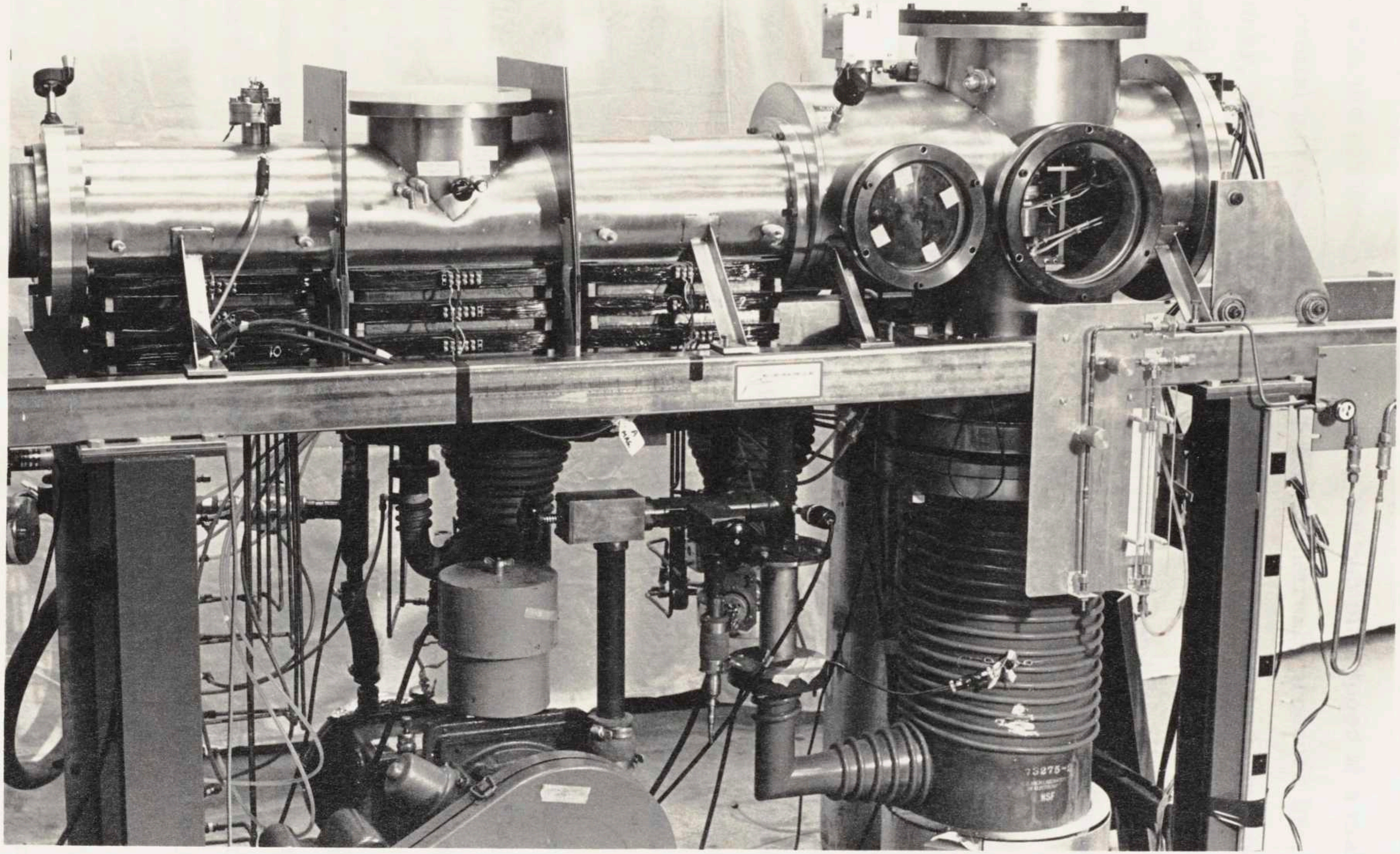

Fig. 3-2 Molecular Beam Apparatus--Photograph.

diffusion pump. The oven support was designed to minimize interference with the gas flow, in order to keep the pumping speed at a maximum. Differential pumping is used to keep the downstream pressure low. The skimmer, which acts as the first defining element for the beam, is mounted on a mechanism that isolates the source chamber from the velocity selector chamber. This arrangement allows the velocity selector chamber to be maintained at a pressure of 4×10^{-7} torr while the source chamber pressure ranges up to 6×10^{-4} torr.

The flanges separating the magnet chamber from the velocity selector and detector chambers are pierced by 3/8-inch diameter holes through which the beam passes. These holes may be sealed by sliding gate valves, allowing some of the chambers to be at atmospheric pressure while the others are evacuated. The gate valves contain plexiglas inserts, sealed by O-rings, that create a line of sight from the detector chamber to the velocity selector chamber; the ability to look down the machine is helpful when checking the magnet alignment.

Separating a small fraction of van der Waals molecules (less than 10^{-3}) from a large flux of potassium atoms presents a major experimental problem. The two species have the same spin and, due to the properties of jet beams, the same speed. As discussed in section 4.2, their deflections are therefore inversely proportional to their masses; this provides the primary separation mechanism. Good spatial separation requires A and B magnets with high deflecting powers. Consequently, the magnets are 10 inches long. With a gradient of 34 kG/cm, the maximum atom deflection for a typical beam velocity of 9×10^{4} cm/sec is 0.015 radians, corresponding to a displacement of 0.071-inch at the end of the magnet, or approximately 0.218-inch at the detector position.

Because magnetic deflection depends on the particles' velocities, separating the molecules from the atoms requires a very narrow velocity distribution in the beam. Although a supersonic jet produces a beam with an intrinsically narrow velocity distribution, a velocity selector is necessary to completely eliminate atoms with velocities outside the main distribution. The problem of species separation is discussed further in Chapter 4.

To minimize outgassing problems in the magnet chamber, the magnet system was designed with the magnet yokes and coils outside of the vacuum; only the iron pole faces lie within the vacuum envelope. The stainless steel floor of the magnet chamber contains rectangular iron inserts that provide a low-reluctance path for the magnetic flux. Locating the coils outside the chamber permits air cooling, eliminating the problem of water cooling within the vacuum.

For convenience, several large viewing ports are provided in the source and velocity selector chambers. Besides providing access when assembling the source or velocity selector, these ports are invaluable for finding out what has gone wrong during an experiment--a not unusual occurrence. The entire source mechanism is mounted on a stainless steel flange, which rolls away from the source chamber on a carriage on rails. This arrangement allows one to work on the source in relative freedom.

Because different beam species are selected for passage through the machine, the source mechanism is adjustable, allowing the beam to enter the A magnet at any desired angle. The source motions are described in sections 3.2A and 3.2H.

3.2 Source

A. Description

The source consists of the oven, the skimmer, heaters for the oven and skimmer, cooling plates to condense alkali vapor and to remove excess heat, and a moveable support. The parts of the source are adjustable: the oven can be translated horizontally and vertically, and rotated about its vertical axis; the source as a whole rotates about the A magnet to allow different spin states to be selected; and the skimmer has an independent lateral adjustment. A side view of the source is shown in Fig. 3-3.

The heart of the source is a cylindrical stainless steel oven in which heated alkali vapor and rare gas mix. The oven body, top, and nozzle are heated by independently controlled heaters. Heat loss is minimized by supporting the oven on two pointed stainless steel pins, and by surrounding it by thin stainless steel radiation shields. The shields are surrounded in turn by a water-cooled copper cylinder that absorbs the transmitted heat; without this cooling jacket the source chamber would become greatly overheated.

It is essential to keep the nozzle hotter than other parts of the oven, to prevent alkali from condensing on the nozzle and clogging it. Consequently, the nozzle is attached to the oven body by a short stainless steel tube, which provides enough thermal isolation to allow the nozzle temperature to be adjusted independently of the rest of the oven.

The conical stainless steel skimmer faces the nozzle approximately one centimeter downstream. To prevent its clogging, the skimmer is thermally isolated from its mounting plate by a thin stainless steel tube, and is heated. The skimmer protrudes through a flat, water cooled

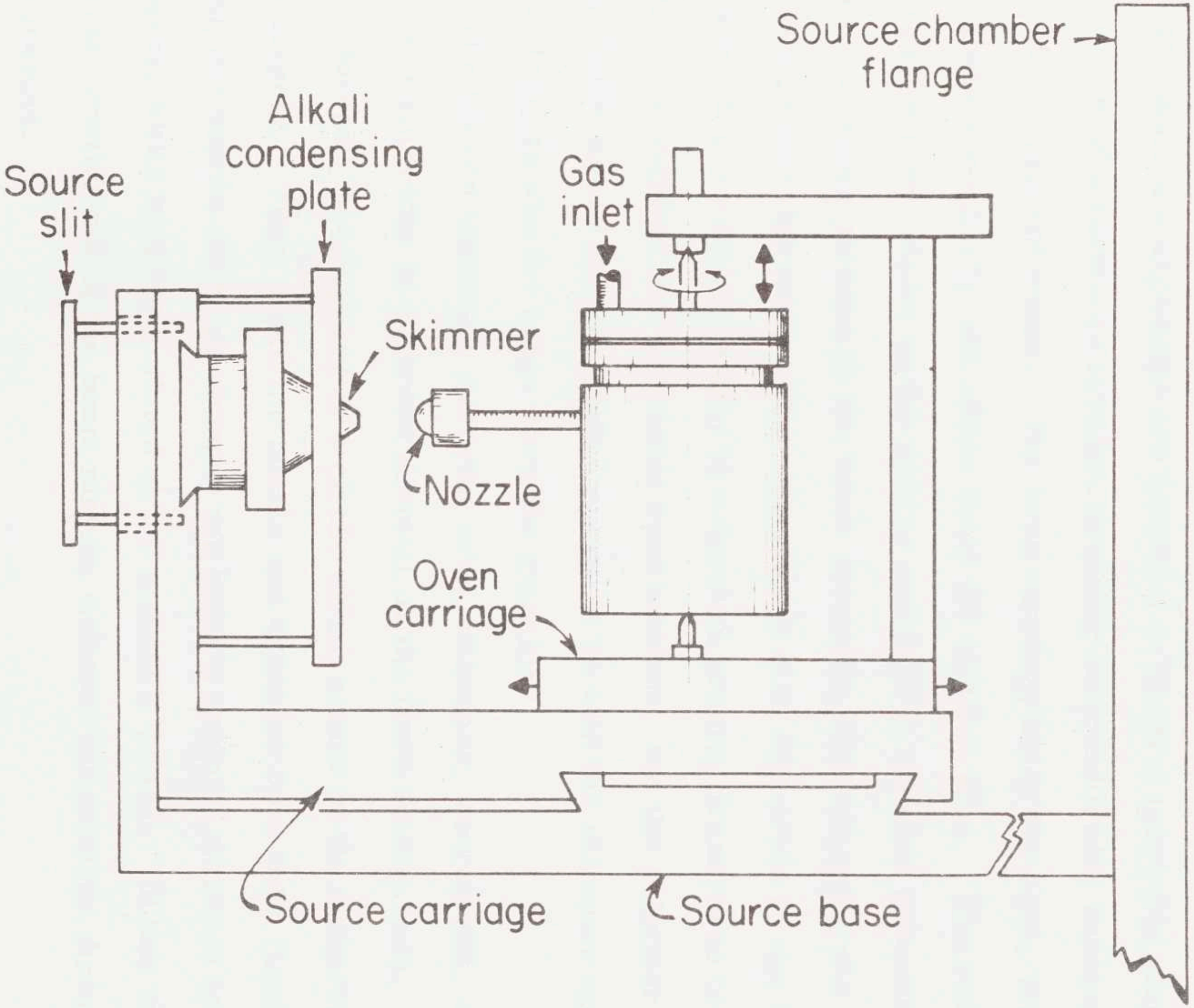

Fig. 3-3 Source Apparatus.

copper plate that condenses the excess alkali that fails to go through the skimmer aperture.

An adjustable slit is mounted downstream from the skimmer to initially collimate the beam. This slit removes most of the unwanted beam that contributes background noise by scattering into the detector can from the velocity selector and from other surfaces.

The source components are mounted on several moveable platforms, reminiscent of a relativity paradox involving railroad trains running on top of other railroad trains. The oven carriage holds the oven, which can translate vertically and rotate about its vertical axis. The oven carriage, in turn, slides on the source carriage in dovetail grooves that permit it to move parallel to the beam direction, thus changing the nozzle-skimmer distance. The skimmer is also supported by the source carriage; it moves horizontally in a dovetail groove, transverse to the beam. The vertical and rotational oven motions, and the skimmer translation, allow one to line the nozzle aperture up with the skimmer opening, and, in fact, to aim the beam down the machine.

The source carriage, carrying oven, skimmer, source slit, cooling plate, and all, rides in a curved dovetail on the fixed source base. The source dovetail is a segment of a circle whose center is the midpoint of the A magnet. Thus, when the nozzle and skimmer have been lined up, moving the source carriage changes the beam's angle of entrance into the A magnet, while keeping it aimed at the magnet's center. In this way, different constituents of the beam may be selected for passage through the A magnet.

B. Oven

A cross section view of the oven is shown in Fig. 3-4. The oven

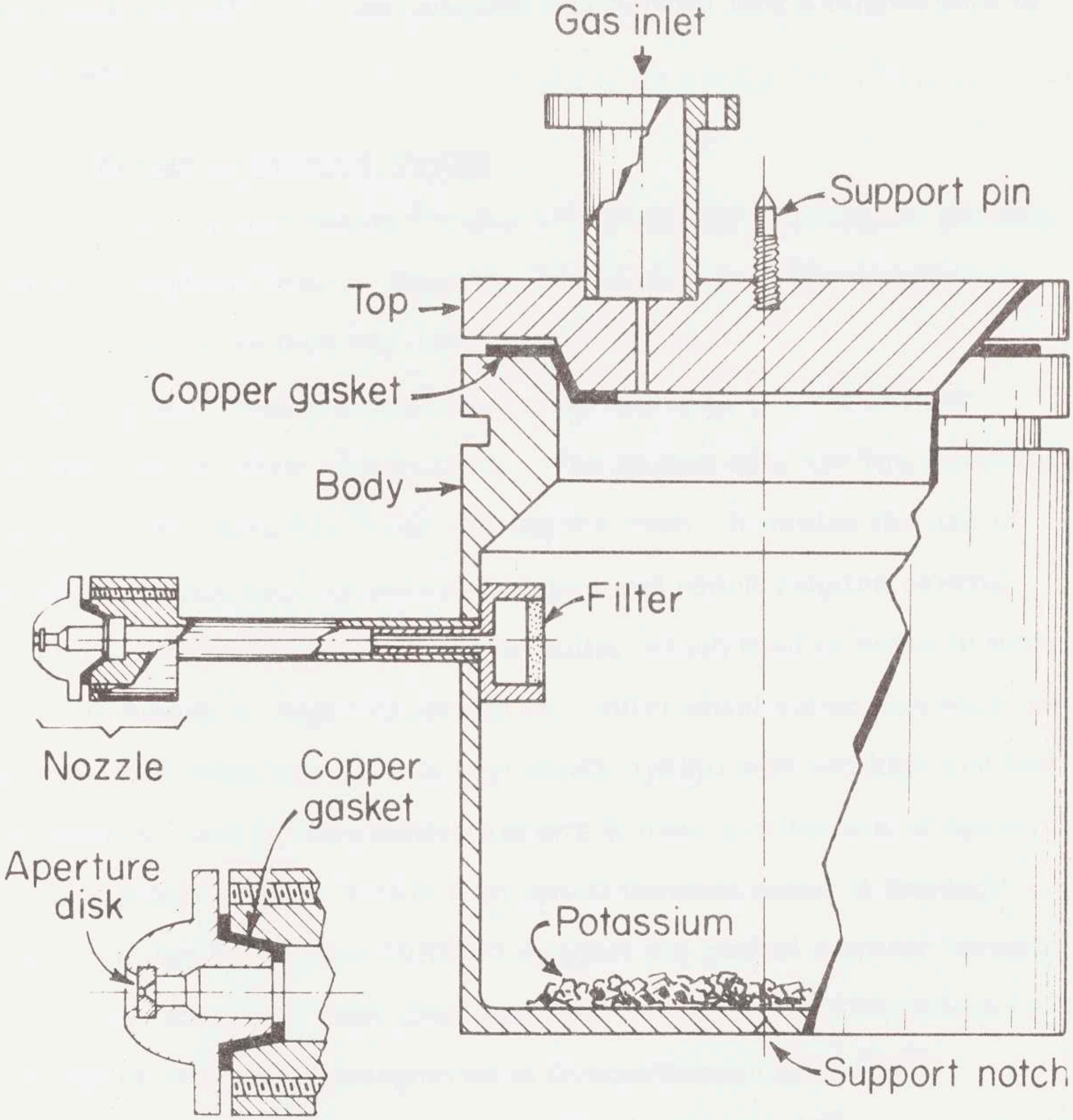

Fig. 3-4 Source Oven.

body is a stainless steel cylinder two inches in diameter and two inches long, with 1/16-inch thick walls. A thin, removable copper heating jacket clamps around the oven. This detachable heater allows the oven to be removed easily from the apparatus, and minimizes the oven's thermal mass. An indentation in the bottom of the oven accepts a pointed support rod; a second support rod screws into a tapped hole in the oven top.

C. Flange and Gasket Design

The oven top and nozzle flanges are sealed by thin copper gaskets squeezed in tapered seats. Once the parts have been drawn together, screws are not necessary for maintaining the seal.

This type of seal has been described previously (BRY59) but apparently has not been widely used. The gasket seal has the following advantages over other types for sealing the oven: it avoids the use of knife edges, which become dull or knicked and which require careful machining; it does without screws or bolts, which tend to seize in their holes when heated to high temperatures; differential expansion does not loosen the seal when the oven is repeatedly cycled between high and low temperatures; and by eliminating screws it uses a minimum of space, which is valuable when a nozzle with small thermal mass is needed. Brymer and Steckelmacher (BRY59) suggest the gasket seal for vacuum use; we have used a $1\frac{1}{2}$-inch diameter seal successfully with positive oven pressures of over two atmospheres at temperatures up to 630°C.

The mating flanges and seats are machined to a 10° taper. Their dimensions are not critical as long as the inside diameter of the seat is small enough to engage the male taper tightly when the gasket is in place. A specific pressure must be applied to the gasket to make it seal to the seat. The total area of the seat is proportional to the seat length; therefore, a longer seat requires a greater total sealing force. This force is transmitted radially to the oven and can spread the opening, preventing the flange and seat from mating. For this reason, the seat length should be short. The seat tapers used here are 1/32-inch and 1/16-inch long for flanges of 1/2-inch and $1\frac{1}{2}$-inch diameters, respectively. Copper gaskets 0.005" to 0.010" thick have been used successfully. Plain copper sheet seems to be as suitable as OFHC copper. At the time of writing, 0.005" gaskets are being used for the nozzle gaskets, and 0.007" for the top.

The top and nozzle flanges are attached by pressing them into their seats with clamps; after the seals are made, the clamps are removed from the oven. Greatly excessive torque on the clamping screws can damage the sealing surfaces irreparably, while insufficient torque will not effect a seal. For repeatability, therefore, the screws are tightened with a torque-limiting screwdriver. Typical values for the top and nozzle seals are given in Table T3.1.

Table T3.1

Gasket Seal Data

	Flange Diameter (inches)	Gasket Thickness (inches)	Number of Clamping Screws	Torque on Clamping Screws (inch-lbs)	Size of Clamping Screws
Oven top	$1\frac{1}{2}$	0.007	8	18 - 22	10-32
Nozzle	$\frac{1}{2}$	0.005	5	10	4-40

The gasket seal is formed by the gasket material cold welding to the stainless steel seat and flange. The flanges are removed by prying with jackscrews inserted in 4-40 holes tapped in the oven top and in the nozzle socket. Any copper remaining on the steel surfaces is removed by a solution of 40% HNO_3 and 3% HF.

D. Heaters

The oven body and the skimmer are heated by home-made cartridge heaters made of annealed tantalum wire wound in alumina tubes (Fig. 3-5). The heaters slip into metal tubes, and can be removed easily in case of failure. The primary cause of failure of this type of heater is breaking of the wire at its point of entrance. To prevent this, the heaters are made with stranded nickel lead-wires, as shown in Fig. 3-5.

The nozzle heater is wound on a 0.005"-thick molybdenum cylinder that slips over the nozzle. The cylinder is sandblasted to roughen its surface, then coated with Sauereisen No. 78 refractory cement.[1] 0.010-inch tantalum wire is wound over the cement and affixed by a second layer of cement. This heater has a very small mass and occupies little space. It has been highly reliable in operation to 650°C.

E. Nozzle

The nozzle aperture disk (Fig. 3-4) is permanently mounted in a removeable nozzle flange. This arrangement permits the use of different diameter apertures, and allows the aperture disks to be separated from the oven for cleaning. The aperture is a conical hole at the center of a circular metal disk. The disks are 3-mm in diameter and 0.010" thick; platinum and molybdenum aperture disks have been used.[2]

The disks are attached to the nozzle flanges by a metal-spinning technique. (Both brazing and electron-beam welding have proven

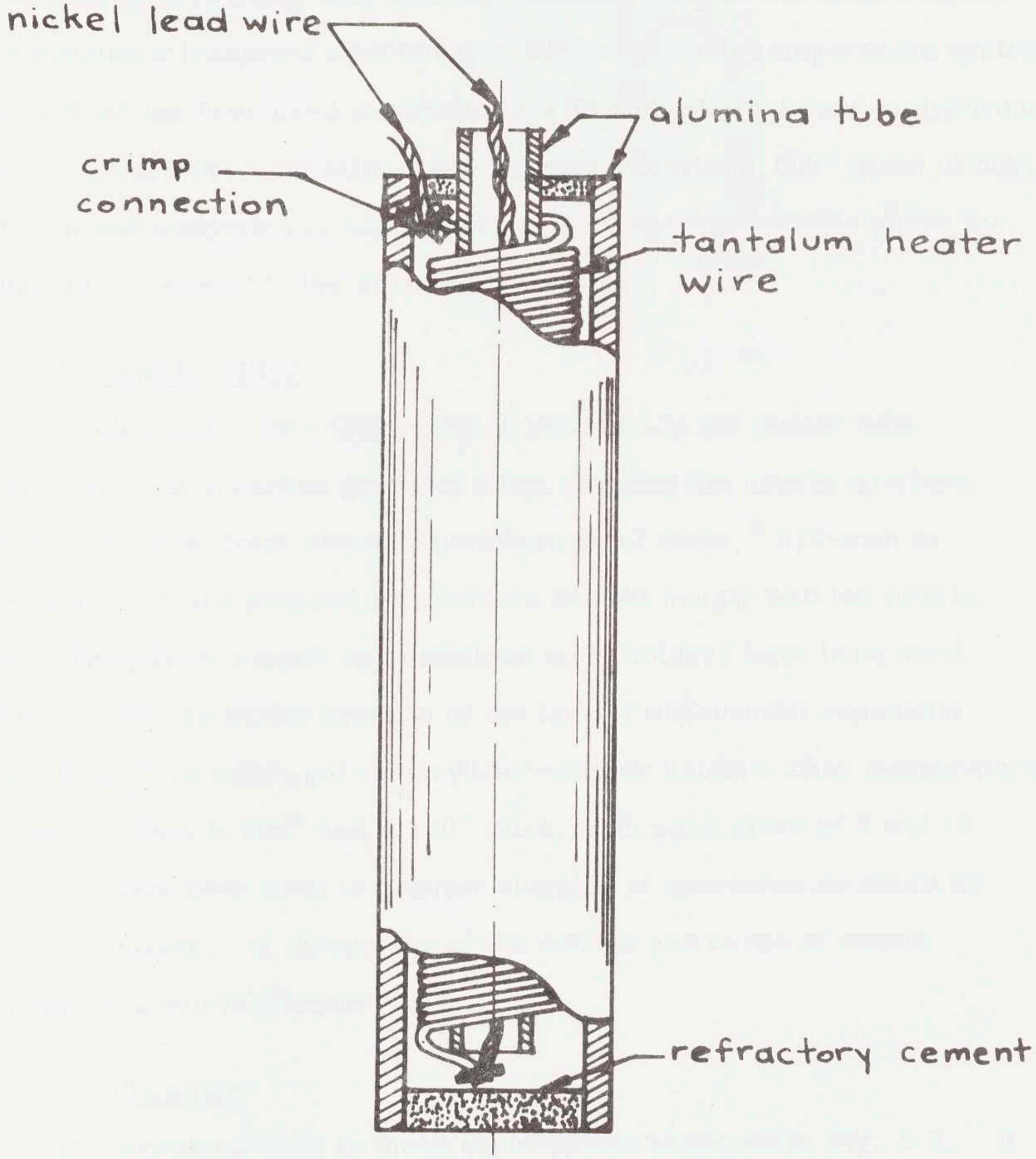

Fig. 3-5
Cartridge Heater

unsuccessful.) A recess 0.125'' in diameter and 0.015'' deep is machined in the end of the flange, to hold the disk. While flange and disk rotate in a lathe, the shoulder of the recess is pressed over the rim of the disk by a rotating ball-bearing assembly held in the lathe toolpost. This creates a leakproof seal that has withstood many temperature cycles. The method has been used successfully with both platinum and molybdenum disks. It does not work with disks that are too thin (0.002'' disks of both platinum and molybdenum have been tried): the disks wrinkle under the radial force created in the spinning operation.

F. Nozzle Filter

A removable filter (Fig. 3-6) is installed in the nozzle tube (Fig. 3-4) to keep carbon granules from clogging the nozzle aperture. Filters are made from sintered stainless steel disks,[3] 3/8-inch in diameter, that are pressed into holders that fit snugly into the nozzle tube. Beryllium-copper and stainless steel holders have been used. Stainless steel is better because of the lack of differential expansion: filter disks have fallen out of beryllium-copper holders after temperature cycling. Disks 0.062'' and 0.100'' thick, with pore sizes of 5 and 10 microns, have been used to prevent clogging of apertures as small as 0.001'' diameter. A discussion of the causes and cures of nozzle clogging is given in Chapter 4.

G. Skimmer

The skimmer used in these experiments is shown in Fig. 3-7. It is a hollow stainless steel cone, with included angles of 70° internal and 86° external, and a 0.030 mm diameter aperture.

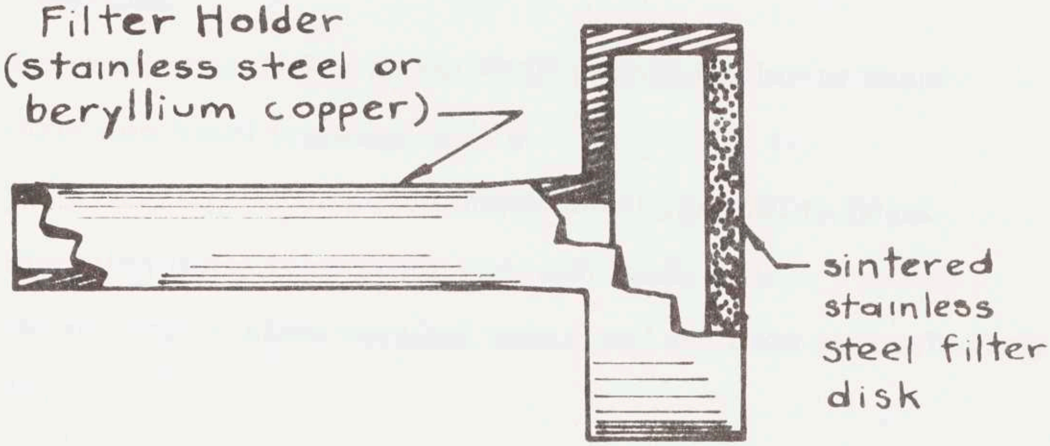

Fig. 3-6
Nozzle Filter

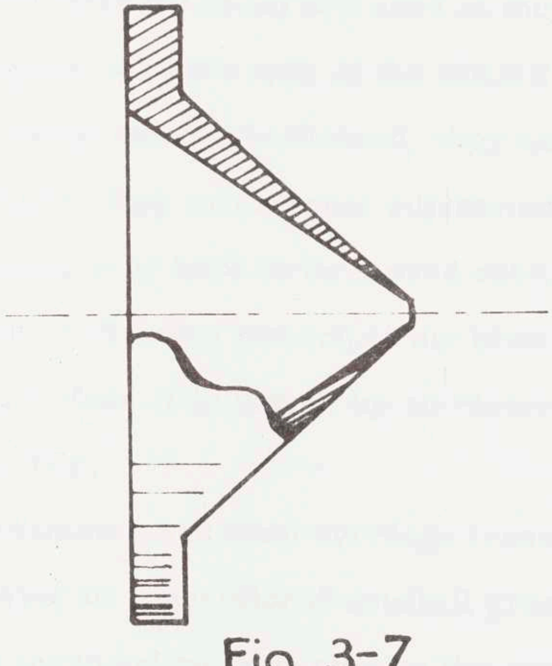

Fig. 3-7
Skimmer

H. Source Motions and Construction

As mentioned earlier, many parts of the source mechanism can be moved with respect to one another during the experiment. Five adjustments are available:

(a) Skimmer translation (horizontal) perpendicular to beam direction (total translation $\frac{1}{4}''$).

(b) Oven carriage translation (horizontal) parallel to beam direction (total translation approximately $\frac{1}{2}''$).

(c) Oven rotation about vertical axis (total rotation approximately 7°).

(d) Oven translation along vertical axis (total translation $3/16''$).

(e) Source carriage rotation about vertical axis through center of A magnet (total rotation approximately 1°--corresponding to horizontal motion of rear of source carriage of approximately $\frac{1}{2}''$).

Adjustments (a) to (d) are used at the start of a run to align the molecular beam with the axis of the MBMR apparatus. Once the maximum signal has been obtained, they usually need not be changed; for this reason, they are manual adjustments. The source carriage, on the other hand, may have to be moved several times during an experiment, to display the deflection pattern of the beam or to select a particular species; therefore it is driven by an electric motor installed in the source chamber.

The skimmer and oven carriage translations are accomplished by sliders moving in conventional dovetail grooves. The oven carriage is driven by a threaded rod mounted on the source carriage; the skimmer slider is moved by an eccentric circular cam also attached to an extension of the source carriage. The cam and the threaded rod are turned by flexible shafts coupled to stainless steel rods that pass through vacuum quick-connects[4] welded into the source flange. (Entirely rigid shafts would prevent the source carriage from moving laterally.) The use of O-ring sealed vacuum quick-connects for motion feedthroughs has proven quite satisfactory. They are relatively inexpensive, maintain a vacuum to 10^{-7} torr or less in this application, and, when properly lubricated and tightened, do not leak when the shaft passing through them is translated or rotated. We have found Apiezon M grease to be satisfactory for the quick-connects; Dow Corning 704 diffusion pump oil, however, seems to damage the O-ring material, causing shaft motion to wear the O-ring excessively.

The source carriage moves on a curved dovetail assembly that allows the source to move in a circular arc (Fig. 3-8). The seal between the source chamber and the velocity selector chamber is maintained as follows. Attached to the end of the source base is a vertical plate. A conical neoprene gasket seals this "backing plate" to the flange separating the source and velocity selector chambers. A second vertical plate is attached to the source carriage. (This plate, which contains the skimmer dovetail groove, supports the skimmer and the source slit.) The facing sides of these two plates are machined to form mating circular cylinders whose common axis coincides with the axis of rotation of the source carriage, that is, with a vertical line through the center of the A magnet. The faces touch, with the exception of a few gaps of up to 0.004". This large-area sliding seal provides sufficient vacuum isolation to maintain the pressure in the velocity selector chamber at less than 5×10^{-7} torr while the source chamber is at 6×10^{-4} torr.

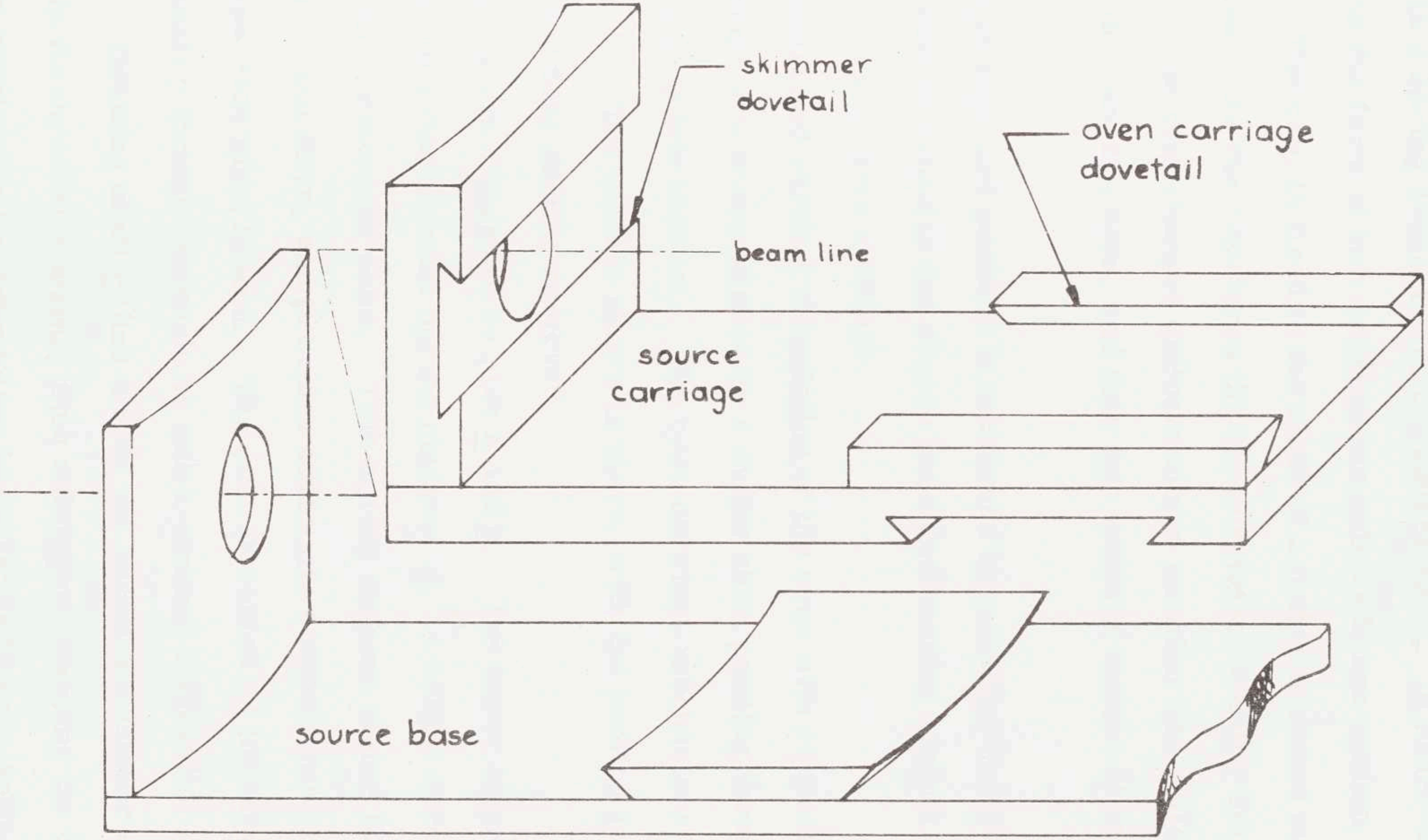

Fig. 3-8
Source Base and Carriage

A schematic view of the mechanism for moving the source carriage is shown in Fig. 3-9. The lever pivots on a fulcrum attached to the source base. One end of the lever is attached to the source carriage, the other to a spring connected to the source base. A heart-shaped cam[5] cut in the form of two Archimedes spirals bears against a cam follower. The cam is fixed to the shaft of a motor mounted on the source base. As the cam turns the lever rotates, moving the source carriage. The cam changes uniform motor rotation into uniform linear motion of the cam follower, and thus into uniform motion of the source carriage.

Source carriage position is measured by a spring-loaded linear potentiometer attached to the source base and bearing against an extension of the source carriage.

Rotation and vertical translation of the oven with respect to the oven carriage are accomplished by a single shaft passing through a source flange quick-connect. The oven carriage mechanism is shown in Fig. 3-10. The oven is shown in place, with the cooling jacket, heaters, and heat shields removed.

The oven is supported by pins a and b. The lower support pin, b, is attached to a commercial spring plunger, d,[6] a hollow screw containing a spring and a moveable point. This spring support allows the oven to be moved up and down, and provides automatic compensation for the oven's expansion when heated. The oven is raised or lowered by pushing shaft e forward through its quick-connect until miter gears f and g engage. Rotating shaft e then drives the beryllium-copper screw h up or down in its threaded housing, thus raising or lowering the oven.

The oven's angular orientation is controlled by the knife-edge i and

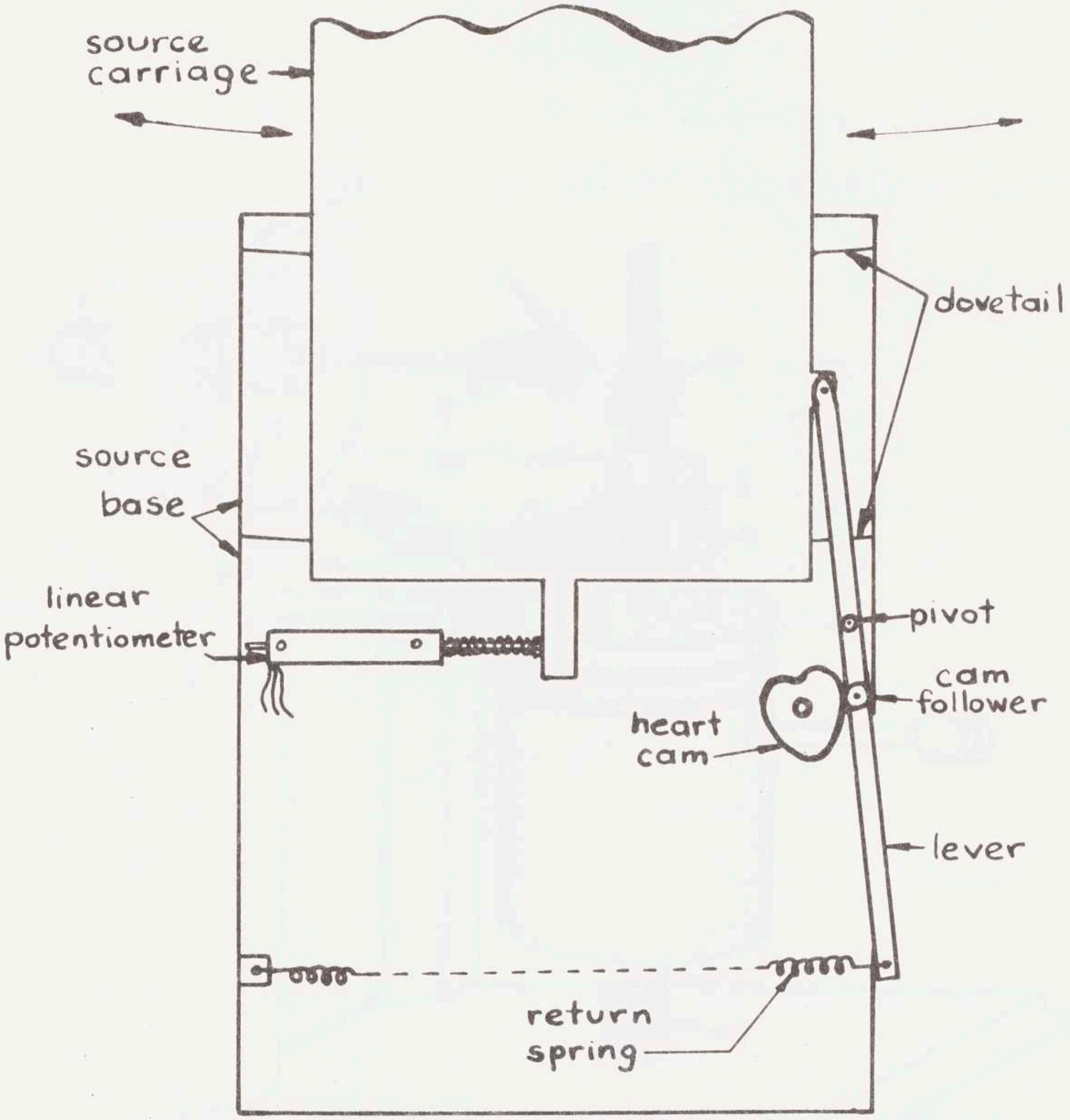

Fig. 3-9
Source Motion Detail
(top view)

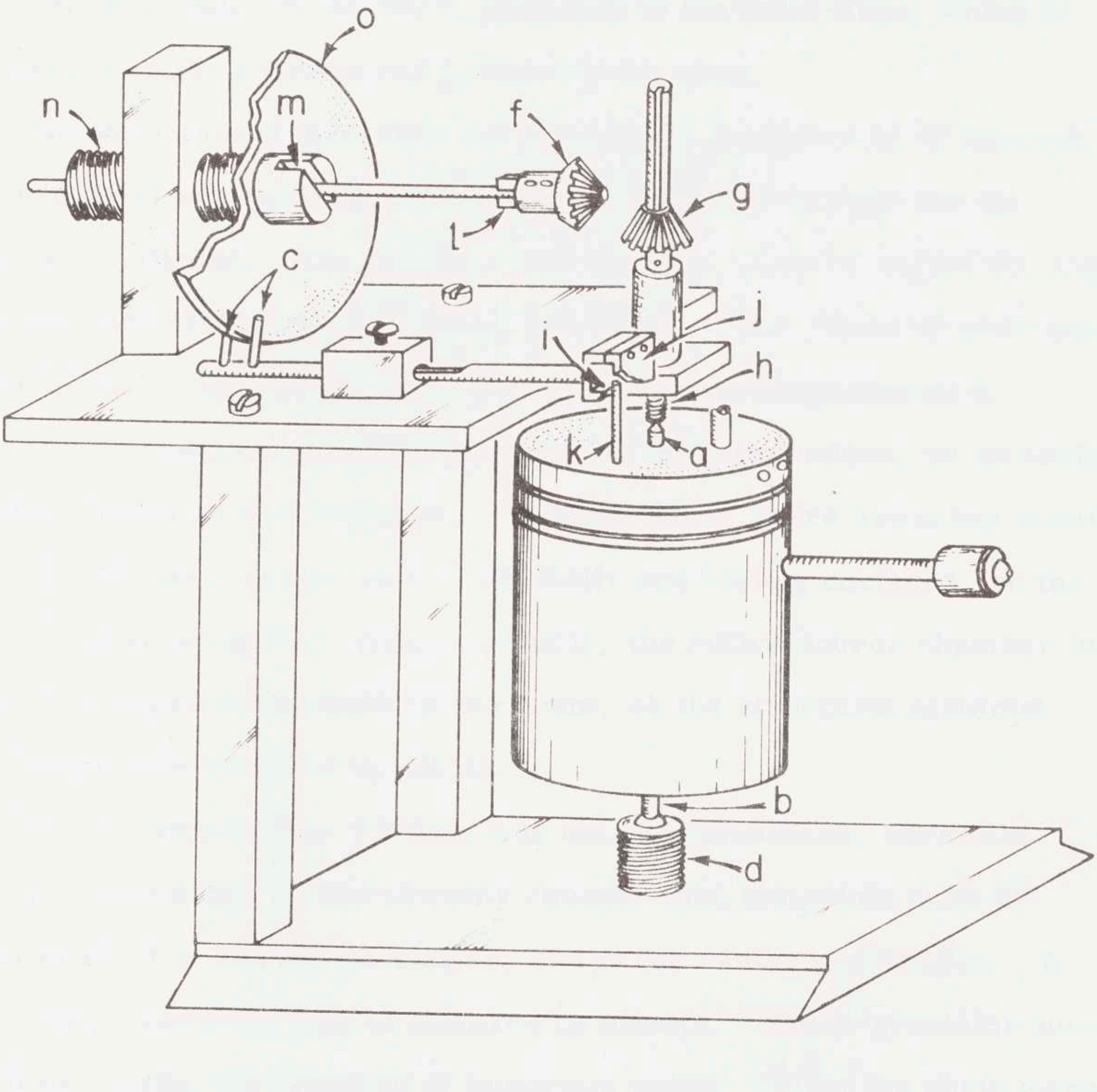

Fig. 3-10 Oven Carriage.

plate j, which together form a slot that engages the rotating-rod k. A thin stainless steel rod and a knife-edge are used here to minimize heat conduction from the oven. The oven is rotated by pulling shaft e back until the tabs ℓ engage slot m. Rotating shaft e drives the beryllium-copper screw n forward or back in its housing. Disk o, which is attached to screw n, moves with it. Since the disk engages the two rods c, it pushes or pulls on the shaft connected to the knife-edge, which in turn pushes on the rotation rod k, turning the oven.

The selection of materials for the source apparatus is of interest. Stainless steel was used for the oven because of its strength and its inertness to alkalis. The cooling surfaces were made of copper for high thermal conductivity and for ease of soldering. The choice of material for the support mechanism, however, was not so straightforward. Considerable machine work was involved in its construction, so an easily machined material was desirable. Furthermore, there are many moving parts, particularly in the form of dovetails and sliding surfaces, so the material must not gall or catch. Finally, the entire source chamber is exposed to scattered portions of the beam, so the structural material must be immune to attack by alkali.

The solution to this problem was found in aluminum, specially treated. Aluminum is considerably cheaper than materials such as stainless steel or beryllium-copper, and is far easier to machine. It galls easily, however, and is attacked by alkalis. These problems were solved by coating the surfaces of important parts. First the parts were hardcoated,[7] a low-temperature anodizing process that deposits a dense, hard layer of aluminum oxide on the surface. The aluminum oxide skin does not gall or catch, and is inert to alkali. However, although it is less porous than an ordinary anodized coating, alkali hydroxide could penetrate the pores and attack the underlying aluminum. To prevent this, the hardcoated surface was filled with a special sealant[8] and coated with a layer of Teflon for maximum lubricity.

I. Gas Handling System

Argon Zero gas,[9] containing less than 0.5 ppm hydrocarbons, is supplied from a tank with a standard two-stage regulator. It passes (Fig. 3-11) through a rotameter-type flowmeter,[10] then through a stainless steel U-tube filled with type 13X molecular sieves (zeolite),[11] and finally, through a quick-connect in the source flange, to the flexible stainless steel corrugated tube attached to the oven gas inlet. The corrugated tube ends in a beryllium-copper cup filled with steel wool and stoppered with a loose-fitting stainless steel filter. (The steel wool prevents alkali from migrating into the corrugated tube; the filter prevents steel wool strands from falling into the gas inlet in the oven top.) The flange on the cup mates with a stainless steel flange attached to the oven top, and thermally isolated from it, by a thin stainless steel tube. A Teflon O-ring creates the seal. The beryllium-copper cup and the O-ring are cooled by conduction through a copper braid that connects the cup to the water-cooled jacket surrounding the oven. The flexibility of the braid allows the oven to move.

The gas enters the oven through a 0.020" diameter hole drilled through the oven top. The length of the hole ($\frac{1}{2}$") prevents alkali vapor from escaping through the gas inlet; the diffusion time for the alkali against the incoming gas flow is much longer than the time for gas to flow through the inlet; therefore the alkali cannot flow "upstream."

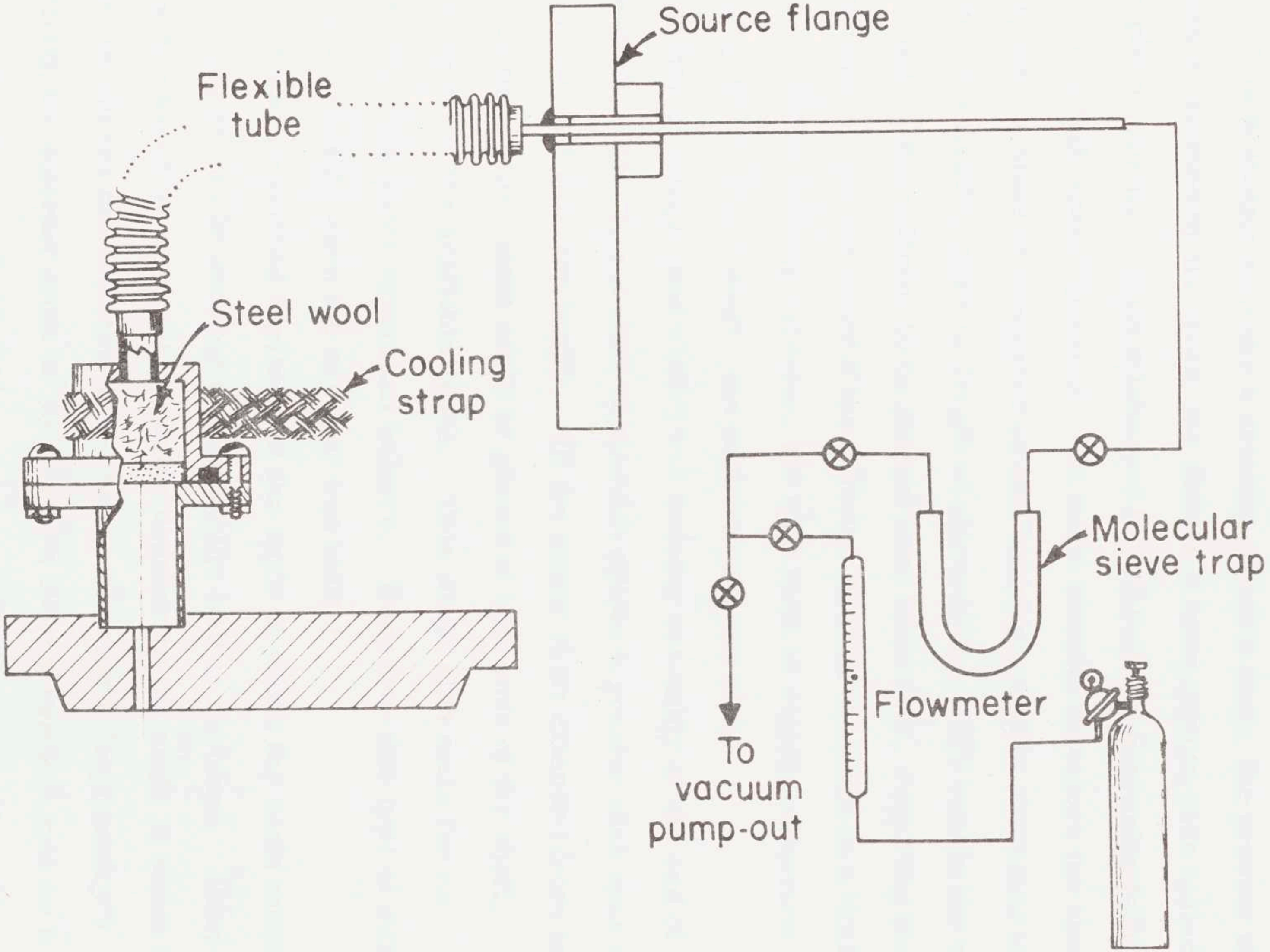

Fig. 3-11 Gas Handling System.

3.3 Velocity Selector

The velocity selector used in this experiment is of a conventional thin-disk design (PRI71B). It differs from others in its compactness and in its method of suspension.

It is desirable to make a velocity selector long: the greater the distance spanned by its disks, the slower it must turn to pass molecules of a given velocity. This minimizes the vibration and bearing failure caused by high speed operation. In many velocity selectors the shaft carrying the disks is supported on ball bearings, and is connected to the motor by a flexible shaft or length of piano wire. This causes the over-all length of the selector to be greater than necessary, requiring the disk separation to be restricted if the selector is to be installed in a limited space. In the present selector, the disk shaft is rigidly connected directly to the motor shaft; the support consists of the two motor bearings, and a third ball bearing assembly at the end of the disk shaft. The direct shaft connection allows a greater disk span for a given over-all selector length. (If the motor shaft extended from both ends of the motor, disks could be placed at both ends of the shaft, utilizing all of the available space. This would also make for an assembly with better dynamical balance. However, this type of motor was not available when the selector was built.)

It was mentioned earlier that the angle at which the beam enters the A magnet can be changed by moving the source carriage. Since the velocity passed by a velocity selector depends on the angle at which the beam traverses the selector (i.e., on the selector's "asymmetry") (PRI71B), the selector must be able to turn about a vertical axis so it can follow the source. A rotatable velocity selector also has the advantage that its asymmetry, and therefore its velocity resolution (PRI71 B), can be chosen at will. For these reasons the velocity selector is suspended on a rod passing through a vacuum quick-connect that is welded into the top of the velocity selector chamber. This suspension allows the selector to be rotated about a vertical axis, and also to be lifted out of the beam when it is not needed. The angular orientation of the selector is measured by a micrometer head mounted outside the velocity selector chamber.

The use of the velocity selector during an experiment is discussed in Chapter 4. An electronic tachometer for use with the velocity selector is described in Appendix A3. 2.

3. 4 Magnet System

A. Magnets

The A, B, and C magnets, and the magnet chamber, are constructed so that the magnet coils are outside of the vacuum. The chamber is made from 8-inch diameter stainless steel tube, with a flat floor $\frac{1}{2}''$ thick (see Fig. 3-1). The floor is stainless steel, with rectangular sections of Armco Magnet Iron welded in (see Fig. 3-12). Both sides of the floor were ground after welding. The iron sections provide low reluctance paths for magnetic flux: they act as links joining the inside and outside portions of the magnet yokes.

To get maximum deflecting power, one would like the A and B magnets to be as long as possible. However, the farther the detector is from the source, the smaller is its subtended solid angle and the smaller the signal received. Therefore a compromise must be made. The A and B magnets are 10'' long, as is the C magnet. (It is advantageous to make the C magnet long also, in order to prevent the fringing fields at its

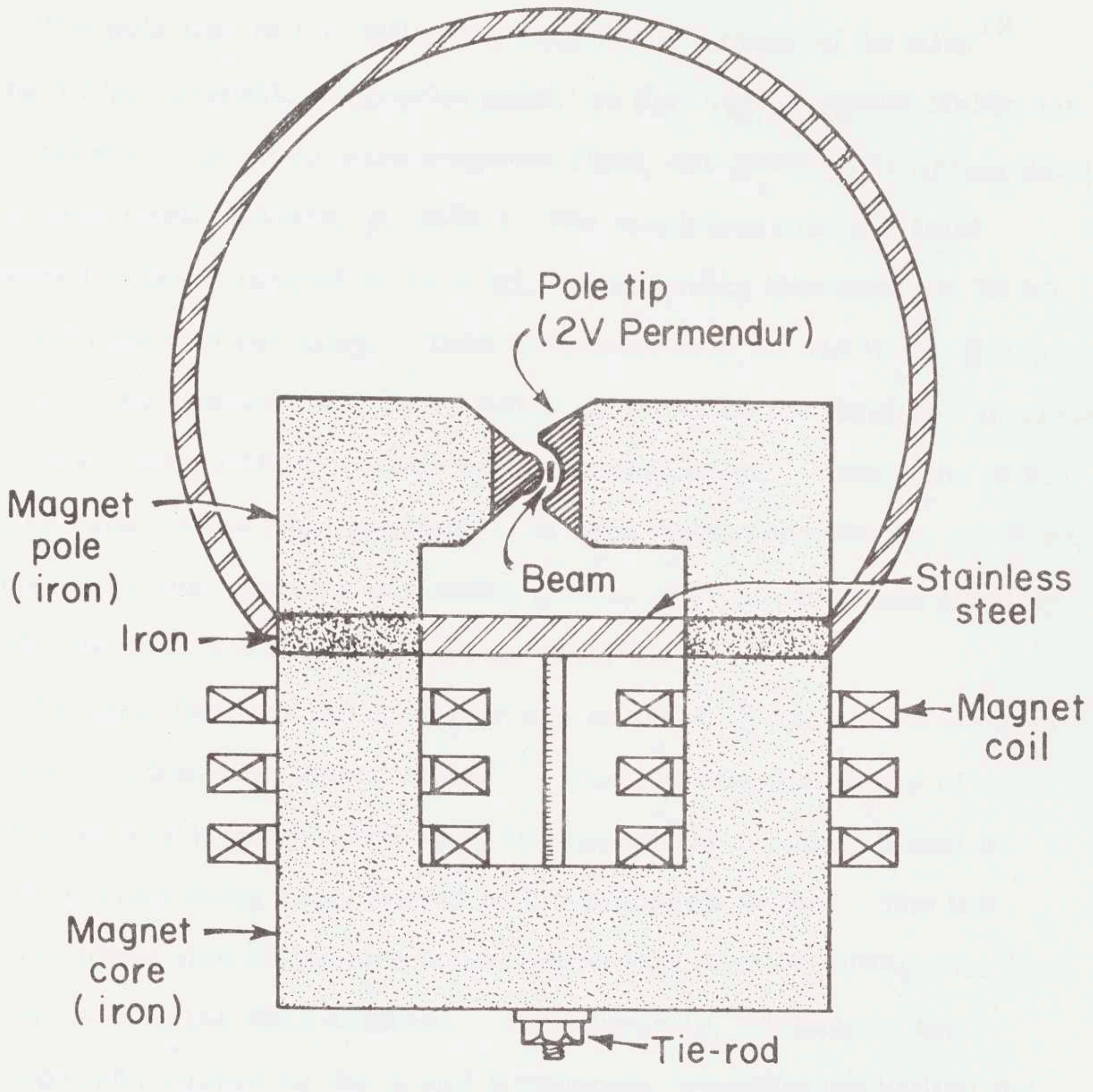

Fig. 3-12 Magnet Chamber (Cross Section).

edges from causing inhomogeneities in the field in the resonance region.) The magnets are separated by three inches, and the magnet chamber is as short as possible (40") to accommodate the magnets. (Unfortunately, the proximity of the A and B magnets to the C magnet causes serious inhomogeneities. This is discussed in Chapter 4.)

The pole tips of the deflecting magnets are made of an alloy[12] having a high magnetic saturation point, so that high magnetic fields can be sustained. (In a two-wire magnetic field, the gradient is proportional to the field itself (RAM56, p. 398).) The maximum average field measured in the B magnet is 19.4 kG, considerably less than the 24 kG saturation point of the alloy. This difference may be due to the sharp corners of the concave pole face, which concentrate the field and saturate before the average field reaches the saturation point. Saturation of the corners reduces the field gradient. At high field strengths the gradient, and therefore the magnet's deflection power, does not increase linearly with the field, and may even decrease (PRI73).

The pole faces of the C magnet are made of $1\frac{1}{4}$-inch thick slabs of 4750 steel, a low-remanence alloy.[13] The low coercive force of this material makes it particularly easy to degauss the magnet, which is important when doing experiments at low magnetic fields. The low coercive force also minimizes field components parallel to the pole face, thereby keeping the field uniform. Unfortunately, because of the inhomogeneity caused by the A and B magnets, we could not utilize the benefits provided by the special pole faces.

The A and B magnets are aligned with the machine axis by means of push rods inserted in threaded holes at either end of the magnets. The rods extend out of the magnet chamber through vacuum quick-connects, allowing the magnets to be moved while under vacuum. Thus the magnets may be precisely aligned using the atomic beam itself to define the axis. The C magnet, which has a half-inch gap between its pole faces, can be pre-aligned accurately enough by eye, and does not have any external adjustments.

B. Beam Collimation

The beam is primarily defined by slits attached to the magnets. They are shown in Fig. 3-1, and in a scale drawing in Fig. 3-13. The A and B slits limit the beam width and restrict the beam to the center line of the apparatus. The C slit, whose opening is adjustable, also limits the beam width; more important, it prevents scattered atoms from appearing at the detector as noise. It serves as a variable attenuator.

Because the field gradients in the A and B magnets are not uniform, a beam that starts as a straight vertical line will reach the detector in the form of a curve: its constituents will have been spread out horizontally. Consequently, a vertical detector filament will sample several overlapping species. To enable the filament to resolve individual species, the beam height is restricted by a horizontal slit 1/8'' high attached to the downstream end of the B magnet. This allows the filament to see only the central portion of the vertical beam.

Clearly, the beam passes close to the defining slits. Therefore the slits must be made of non-magnetic material to prevent Majorana flops, spin inversions caused by an atom or molecules traversing a region in which a magnetic field varies rapidly in space. For this reason all slits are made of beryllium-copper.

The A (and the B) slit is made of 0.005-inch thick beryllium-copper sheet honed to a knife-edge. The slit jaws are screwed to an aluminum

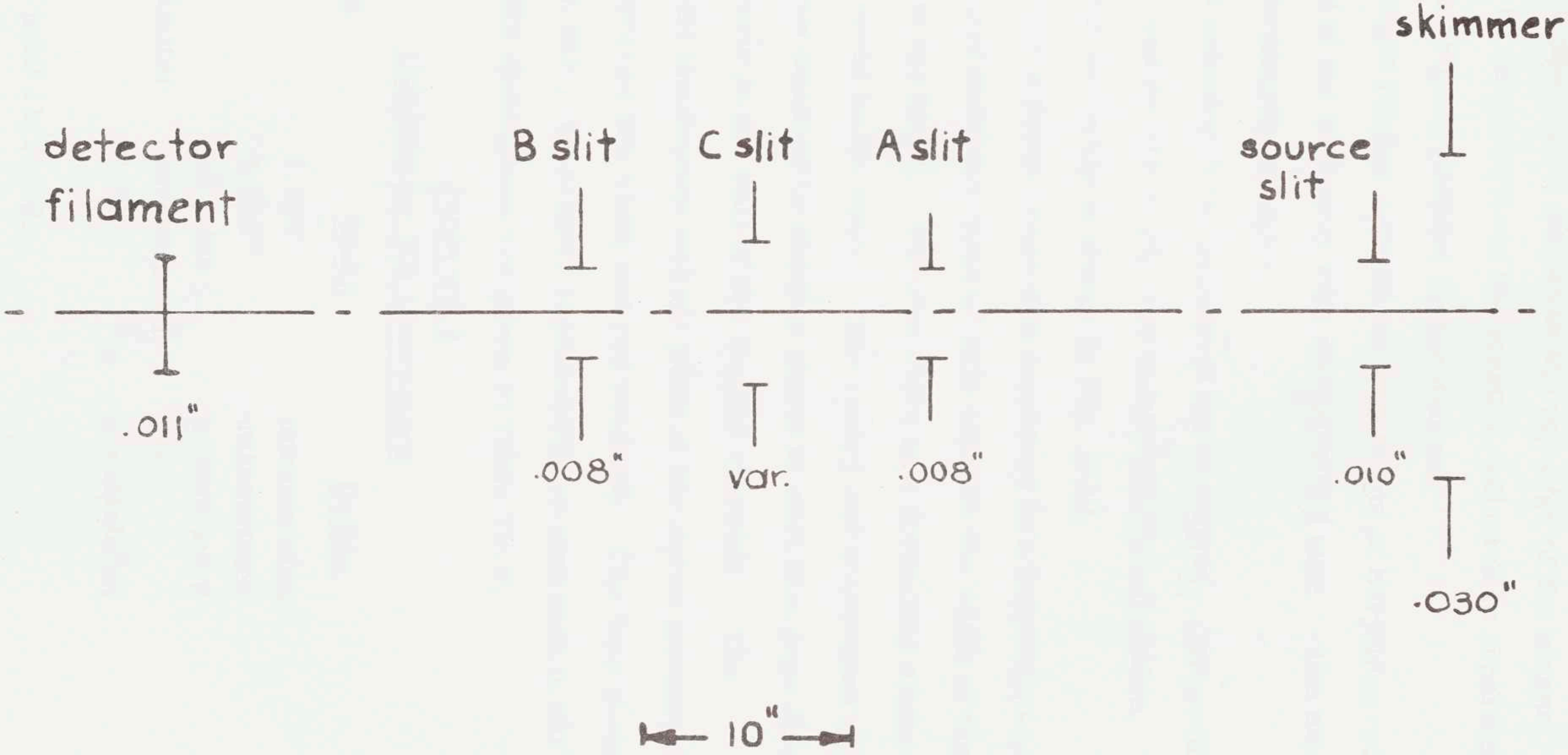

Fig. 3-13 Beam-Defining Elements.

bar that drops over dowel pins affixed to the top edge of the magnet. The slit assembly can be removed from the magnet, adjusted in separation, and returned to its original position on the magnet.

The beam-height limiter consists of two strips of beryllium-copper attached to the end of the B magnet with double-sided tape. The size of its opening is not ordinarily changed.

The C slit is mounted at the middle of the C magnet. Its position in the magnet gap, and its slit width, are independently adjustable. A diagram of the C slit assembly is shown in Fig. 3-14.

The slit itself is a double-edge slot machined in a beryllium-copper rod. Turning the rod about its vertical axis changes the width of the opening presented to the beam. The rod rides in a dovetailed slider which moves transverse to the beam. The rotary and transverse motions are driven by screws attached by flexible shafts to rods that pass through vacuum quick-connects in the wall of the magnet chamber. The dimensions of the slit mechanism and the pitch of the screw threads determine the relation between slit width and rod rotation. One turn of the rod opens the slit 0.008"; therefore, repeatability to less than 0.001" is easily achieved. Slit dimensions are given in Table T3.2.

Table T3.2

Collimating Slit Dimensions

Slit	Width	Height
A	0.008"	unrestricted
B	0.008"	unrestricted
C	variable	unrestricted
height limiter	unrestricted	1/8"
source	0.010"*	unrestricted

*0.017" until 11/12/73.

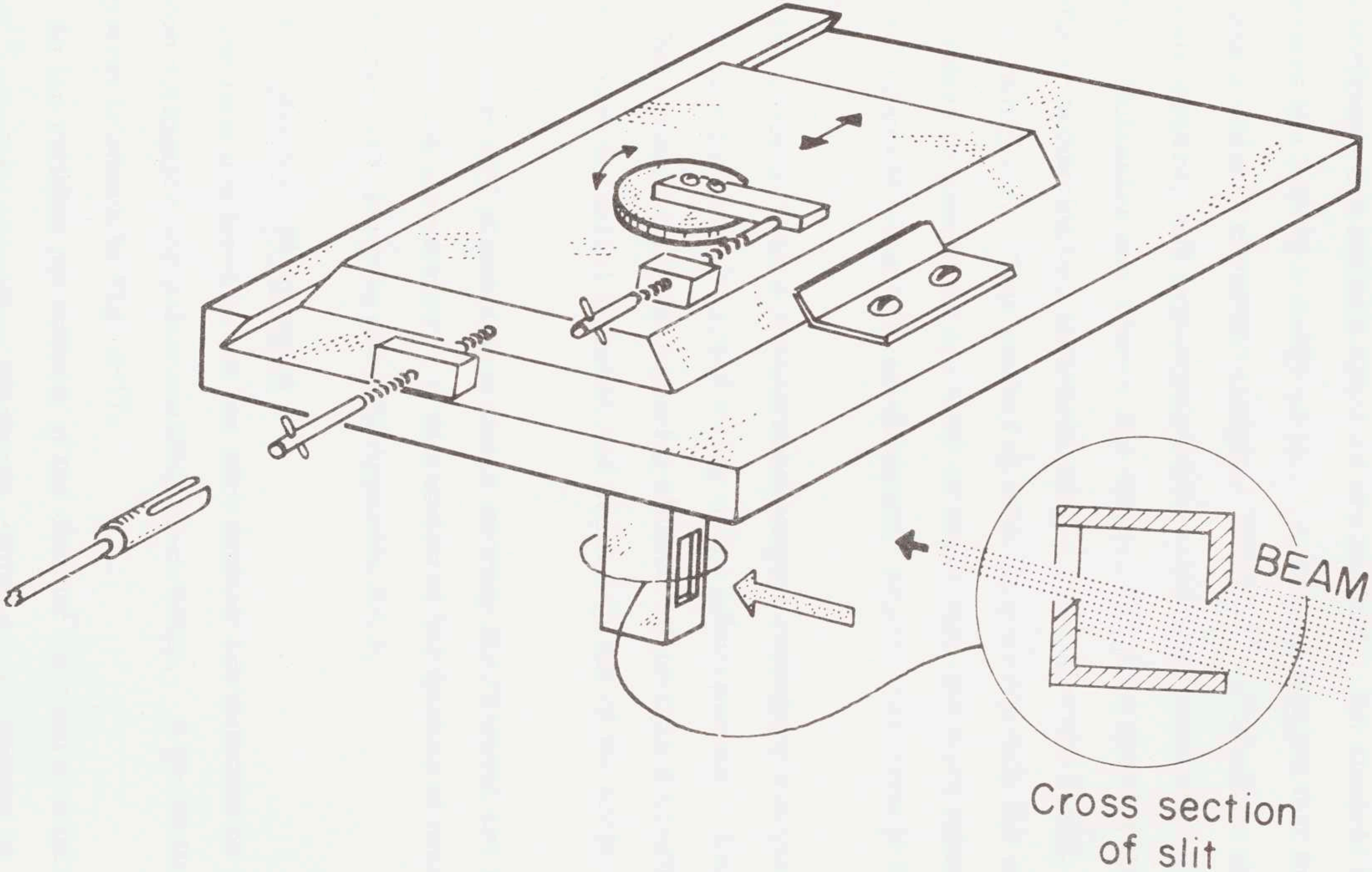

Fig. 3-14 Adjustable Collimating Slit.

3.5 Beam Detection

A. Detector

The beam is detected by a conventional hot-wire detector. Alkali atoms striking a hot iridium filament are ionized. An electric field accelerates the ions to a wedge-shaped permanent magnet that focuses them onto a channel electron multiplier (CEM).[14] Potassium atoms, potassium dimers, and argon-potassium molecules are detected by this method. Molecules and dimers are dissociated when they hit the filament, each dimer producing two potassium atoms, and thus two counts at the electron multiplier. This method of ionization works only for atoms whose ionization potentials are near or lower than the work function of the metal filament--namely, alkali atoms; argon, therefore is not detected.

The electric field and permanent magnet constitute a mass spectrometer that may be tuned to any of the alkali metals. This helps reduce background noise by rejecting alkalis, other than potassium, that are present in the metal filament and which boil out of its surface upon heating.

At least 40% of potassium atoms striking the filament are registered by the detection electronics. A discussion of the method of measuring the detection efficiency is given in Appendix A3.3.

B. Detection Electronics

The ions produced by the hot wire ionizer are detected by an electron multiplier and pulse-counting electronics. A block diagram of the system is shown in Fig. 3-17.

An ion striking the cathode of the channel electron multiplier (CEM)[14] releases secondary electrons, which are multiplied by the CEM

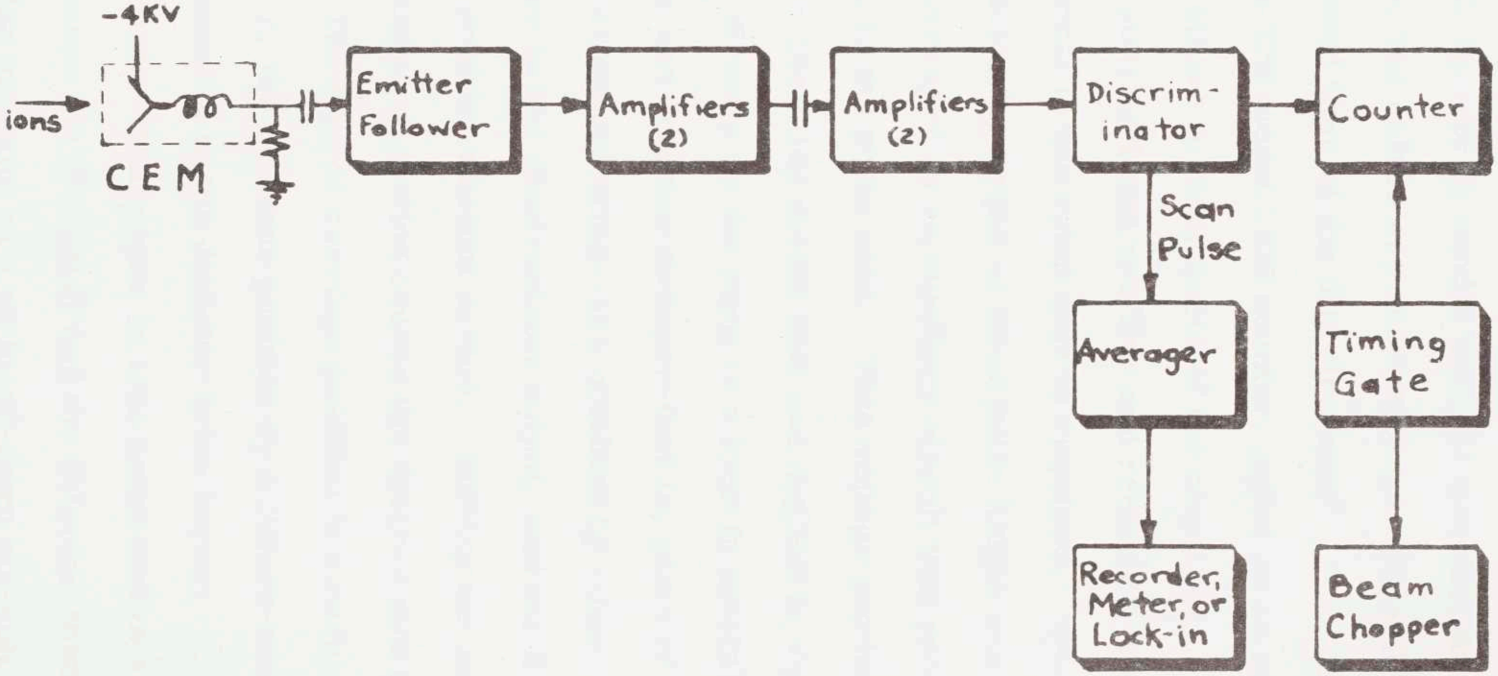

Fig. 3-15
Detection Electronics

and appear as a pulse of charge at the anode. An emitter follower circuit mounted immediately outside the detector chamber matches the high-impedance CEM to the 50-ohm counting electronics. The pulses are amplified by four or five E. G. and G. model AN101 amplifiers and sent to an E. G. and G. model TR104S discriminator. In the amplification stage, the pulses are shortened by a capacitor (differentiator) to reduce the dead time of the discriminator. The discriminator output is counted by a TSI model 1535 counter, gated by an adjustable timing circuit that allows measurement of the count rate.

When plotting beam profiles and resonance spectra, an analog output proportional to the count rate is required. The discriminator provides a scanning output of fixed pulse height and length. These pulses are averaged by an auxiliary circuit that produces a voltage proportional to the pulse rate. This voltage can be measured by an electrometer (Keithley model 602) and applied to a pen recorder, or it can be used directly as the input to a lock-in amplifier.

Source and detector sweeps--that is, plots of beam intensity versus source or detector position--are obtained by connecting the Y input of an X-Y recorder to the electrometer output, and the X input to the appropriate position readout device. Moving the source or detector through its range of motion causes the desired plot to be traced by the recorder. The source carriage position is measured by a linear motion potentiometer, the detector position by a fifteen-turn precision potentiometer connected to the detector drive screw.

The counter timing gate is also connected to a beam chopper mounted between the B magnet and the detector chamber. The chopper is a metal flag mounted on a stripped-down six-volt relay body. By synchronizing the counter and the beam chopper, one can measure the ratio of beam intensity to background filament noise.

The gain of the CEM is between 5 x 10^6 and 1 x 10^8, depending upon the CEM accelerating voltage (4.0 to 4.3 kV) and the multiplier's age. It has been reported (PRI71A) that exposure to oxygen increases the gain of a CEM. When oxygen was bled into the detector chamber, the CEM gain appeared to increase by a factor of five to ten for a few days, then decreased to its previous value. (The oxygen affects the hot wire filament, quickening its response to a change of beam intensity. This effect is discussed in Chapter 4.)

An indirect method is used to determine the counting efficiency of the CEM and its associated electronics. The CEM output cannot be compared directly with the detector efficiency measurement discussed in Appendix A3.3 because the CEM gain decreases rapidly at count rates over 10^5 per second, while it is extremely difficult to measure beam currents of less than 5 x 10^{-12} amperes (3 x 10^7/sec) with the electrometer. Therefore the counting efficiency is determined by measuring the pulse height distribution of the detector. Four or five amplifiers, each with a gain of 4, are used. The discriminator level is varied and a plot is made of count rate against minimum pulse height. The derivative of this curve gives the pulse height distribution. (In other words, the discriminator is used as a coarse-grained single channel analyzer.) If the peak of the distribution is well above the lowest threshold level of the discriminator, one can be sure of counting virtually all of the detector pulses; otherwise, more amplification or a higher CEM accelerating voltage must be used.

3.6 Resonance Coils

The cylindrical resonance coils are mounted between the C magnet pole faces, one on either side of the C slit. They are wound of copper wire, and are supported on the machine axis by Teflon holders. The coil dimensions are given in Table T3. 3.

Table T3. 3

Resonance Coil Dimensions

Coil	Position	Length (cm)	Number of turns	Inside diameter (cm)
long	near B magnet	4. 0	16	0. 9
short	near A magnet	2. 8	15	0. 9

APPENDIX A3.1

APPARATUS DIMENSIONS

SOURCE CHAMBER

Oven

Diameter	2 inches
Height	$3\frac{3}{8}$ inches overall
Material	stainless steel 304 and 347

Oven Filter

Diameter	$\frac{3}{8}$ inch
Pore size	5 and 10 microns
Material	sintered stainless steel

Nozzle Aperture

Diameter	30 - 50 microns
Material	platinum and molybdenum

Source Chamber Pump

Size	10-inch oil diffusion
Baffle	water cooled, optically dense
Net pumping speed	1800 liters/sec

VELOCITY SELECTOR CHAMBER

Velocity Selector

Selector length	3.820 inch
Number of teeth	360 per disk
Fractional open space (η)	0.48

Velocity Selector Chamber Pump

Size	4-inch oil diffusion
Baffle	water cooled 90° elbow
Pumping speed	1250 liters/sec

MAGNET CHAMBER

A and B Magnets

Number of coils	6
Turns/coil	840 nominal (790 minimum)
Wire size	#20
Bead radii	3/16-inch convex, 7/32-inch concave
Bead spacing	0.144-inch
Length	10 inches
Maximum magnetic gradient	34 kG/cm

C Magnet

Length	10 inches
Pole spacing	0.500-inch
Pole height	3 inches
Coils	same as A and B magnets

Beam Defining Elements

A and B slit width	0.008-inch
Height limiter	1/8-inch
Skimmer diameter	0.030-inch
Source slit width	0.010-inch

Magnet Chamber Pump

Size	4-inch oil diffusion
Baffle	none
Pumping speed	1250 liters/sec

APPENDIX A3.2

VELOCITY SELECTOR TACHOMETER

The usual method of measuring a velocity distribution is to allow the selector's hysteresis motor to come into synchronism at a number of frequencies, and to measure the detector count rate at each frequency. This is a slow procedure, and does not work at low frequencies, where the motor power supplies cannot supply enough current to keep the motor in synchronism. To speed the process, measurements were made by allowing the selector to coast from high to low speed while plotting the detector count rate and the selector speed on an X-Y recorder. The instantaneous selector speed was determined by an electronic tachometer.

The schematic diagram for the tachometer is shown in Fig. A3.2-1. A light-emitting diode (LED) and a phototransistor are mounted on the velocity selector frame. A section of the selector shaft is painted black with Aquadag, except for a narrow stripe of shiny stainless steel. Once each revolution, the LED reflects from the stripe to the phototransistor; the resulting pulse is amplified by Q3 and applied to IC1. IC1 produces, for any size or shape input pulse within certain limits, a rectangular pulse of constant length and height. The average output voltage from ICl, then, is proportional to the rate of input pulses, or to the velocity selector rotational rate. The output of IC1 is averaged and applied to the horizontal axis of an X-Y recorder; the vertical axis measures a voltage proportional to the detector count rate (see Chapter 4).

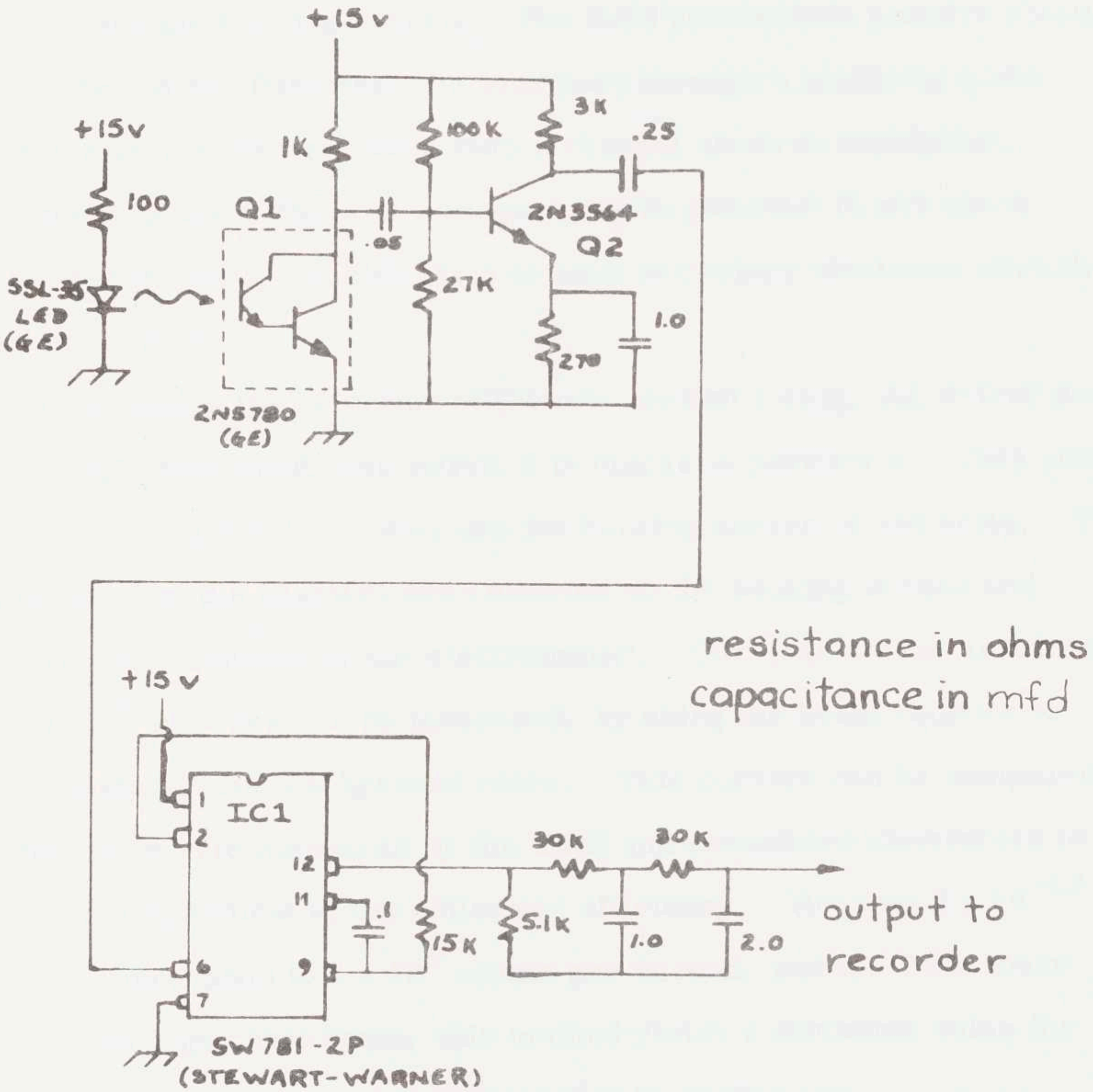

resistance in ohms
capacitance in mfd

Fig. A3.2-1
Velocity Selector Tachometer

APPENDIX A3.3

DETECTOR EFFICIENCY MEASUREMENT

A schematic diagram of the hot wire detector is shown in Fig. A3.3-1. During normal operation the heated filament is in an approximately uniform electric field created by the grounded box surrounding the filament, and the backing screen. The field accelerates positive alkali ions emitted by the filament; the ions pass through a magnetic mass spectrometer that focuses them onto a channel electron multiplier. The cathode of the CEM is at a large negative potential (4 kV) which accelerates the ions, causing them to emit secondary electrons when they strike the cathode.

To measure the detection efficiency, switch 1 (Fig. A3.3-1) of the power supply is opened, and switch 2 is placed in position b. This puts the filament at ground potential and the backing screen at -30 volts. The ions emitted by the filament are collected on the backing screen and measured as a current by the electrometer. Currents as low as a few times 10^{-13} amperes can be measured, by using the beam chopper to discriminate against background noise. This current can be compared with the count rate measured by the CEM and associated electronics to obtain a measurement of the collection efficiency. Because 5×10^{-13} amperes correspond to 3×10^{6} counts per second, and the CEM loses gain at such high count rates, this method yields a minimum value for the efficiency. Data measured using this technique are

Current = $1.8(2) \times 10^{-13}$ A = 1.2×10^{6} counts/sec

Count rate = $0.46(4) \times 10^{6}$ counts/sec

Efficiency ≈ 40%

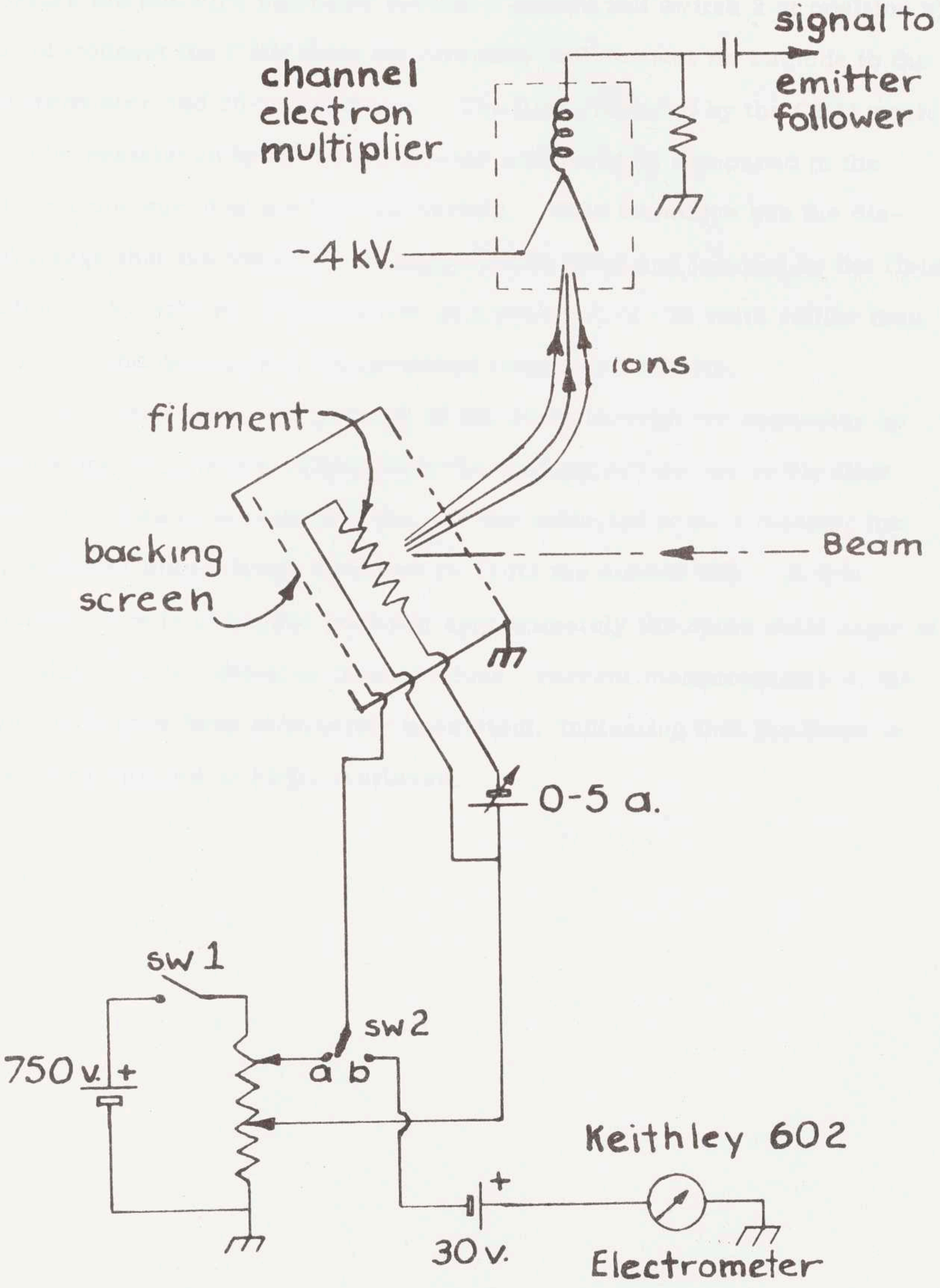

Fig. A3.3-1 Hot Wire Detector.

Another possible method of measuring the detection efficiency is to operate the hot wire normally (switch 1 closed and switch 2 at position a), but disconnect the CEM from its circuitry and connect its cathode to the electrometer and 30-volt battery. The ions collected by the CEM would then be registered by the electrometer and could be compared to the current measured at the backing screen. This technique has the disadvantage that the ions are no longer accelerated and focused by the field at the CEM cathode, which is now at a potential of -30 volts rather than -4 kV. The method has not produced conclusive results.

One may check the passage of the beam through the apparatus by comparing the current collected by the backing screen (as in the first efficiency measurement) with the current collected from a monitor hot wire placed immediately downstream from the source slit. A thin monitor wire is used that subtends approximately the same solid angle at the source as the detector filament does; current measurements at the two wires have been completely consistent, indicating that the beam is not being blocked or badly scattered.

NOTES

(1) Sauereisen Cements Company, Pittsburgh, Pa. 15238.

(2) Ted Pella Company, P.O. Box 510, Tustin, Cal. 92680.

(3) Mott Metallurgical Company, Farmington, Conn.

(4) A. and N. Corporation, P.O. Box 190, Spencer, Mass. 01562.

(5) Cam made to order by Allou Engineering Co., 220 Felton Street, Waltham, Mass. 02154 from gear blank purchased from Pic Design Corp., P.O. Box 335, Benrus Ctr., Ridgefield, Conn. 06877.

(6) Thomas Smith Co., 288 Grove St., Worcester, Mass. 01605.

(7) Duralectra Inc., 61 North Avenue, Natick, Mass.

(8) Duplex Seal of potassium dichromate followed by nickel acetate, Duralectra, Inc. (Note 7).

(9) Airco Industrial Gases, Union Landing Road, Riverton, New Jersey 08077.

(10) Fischer and Porter Co., Warminster, Pa. 18974. Flowmeter FP - 1/16" - 10-G-S Model 10A1017A.

(11) Linde molecular sieves, manufactured by Union Carbide Corp., Materials Systems Division, Moorestown, New Jersey.

(12) 2V-Permendur Alloy (49% iron, 49% cobalt, 2% vanadium), used in the A and B magnet pole tips, was supplied by Teledyne Vasco Inc., P.O. Box 36, Springfield, Mass. 01107.

(13) Type 4750 steel, manufactured by Allegheny-Ludlum Steel Co. was kindly provided by the LINAC group of the M.I.T. Laboratory for Nuclear Science.

(14) Model B419BL, Mullard, Inc., 100 Finn Court, Farmingdale, New York 11735.

CHAPTER 4
EXPERIMENTAL METHODS

Three major hurdles were overcome in making this experiment work: production of a molecular beam containing van der Waals molecules, separation of the molecules from a large background of atoms, and observation of the molecular spectrum. In this chapter we discuss the methods used to accomplish these goals.

4.1 Nozzle Clogging

Production of potassium-argon molecules was delayed for many months by clogging of the oven nozzle, apparently by granules of carbon. One of the difficulties often faced when producing alkali jet beams is the tendency for the vapor to condense and clog the nozzle. Condensation can usually be prevented by maintaining the nozzle as the hottest part of the oven, and can sometimes be reversed by overheating the nozzle to evaporate the condensed metal and reopen the hole. In this experiment, however, such remedies were of no avail; difficult clogging problems were encountered which were unrelated to potassium condensation in the nozzle.

The oven was initially run without rare gas (a top with no gas inlet was used); it operated without clogging with nozzles as small as 0.001-inch diameter. With argon flowing through the oven, however, nozzles below 0.002-inch diameter clogged quickly, sometimes minutes after a potassium beam was found, and sometimes before one could be found. 0.004-inch nozzles were the smallest that could be used without clogging. (Clogging is diagnosed by a drop in the argon flow rate, as measured by the flowmeter in the supply line. Lack of a beam might simply mean that the apparatus was not lined up properly.) If the argon was flowed through an unheated oven containing potassium, the nozzle did not clog.

Under a 100 power microscope the clogging material appears black and porous. It does not decompose in moist air, as a potassium oxide would, and it is insoluble in water and nitric and hydrochloric acids, ruling out most metal compounds, particularly those of the alkali metals. The material seems most likely to be carbon.

It was thought that hydrocarbons were carried into the oven by the argon stream, and reacted with the potassium to form carbon. The following steps were taken to eliminate this possible source of carbon:

1. The gas supply system was constructed entirely of copper tubing, and nickel-gasket connectors were used.
2. A Teflon O-ring was used in the gas inlet connection to the oven top, instead of the previous Viton O-ring.
3. Pure potassium (99.95+%)[1] in a sealed glass ampoule was placed in the oven along with a stainless steel slug. The ampoule was broken by shaking the oven while it was filled with argon. This procedure prevented the introduction of hydrocarbons with the potassium, and prevented the potassium from oxidizing.
4. Research grade argon (0.5 ppm hydrocarbons) was used. Later this was changed to argon zero gas.
5. The argon was further purified by passing it through a molecular sieve trap (type 13X molecular sieves) cooled to dry ice temperature, and then bubbling it through a container of NaK,[2] a liquid alloy of sodium and potassium that should react with any hydrocarbon impurities.

None of these remedies stopped the clogging. (The NaK trap turned out to be more trouble than it was worth: on two occasions NaK was sucked into the supply lines, necessitating extensive--and careful--cleaning.)

The most probable explanation for the origin of the carbon is that it comes from the stainless steel of the oven. It is well known to workers in the field (MAU67, p. 40) that liquid metals in contact with steel surfaces can dissolve carbon out of the steel. Under this hypothesis, the carbon was carried to the nozzle by the argon stream in granular form, rather than being deposited there by chemical reaction. The clogging problem was eliminated by installing in the nozzle tube a sintered stainless steel filter, described in section 3.2F and Figs. 3-4 and 3-6. Filter disks of several sizes (0.062-inch and 0.100-inch thick; 5 and 10 microns pore diameter) successfully stopped the clogging and allowed the use of nozzles as small as 30 microns diameter. When a new oven body was used, however, the small nozzles clogged on several occasions. This may have been due to poorly fitting filters or to a large quantity of carbon in the fresh steel of the new oven, much of the carbon in the original oven having been leached out during months of operation. Clogging in the new oven was reduced by plating the oven, in particular the inside surfaces of the body, with electroless nickel, which creates a non-porous skin on the steel, sealing the carbon in.[3]

At the time of writing, the NaK trap has been eliminated, polyethylene tubing is used for part of the gas system, and the molecular sieve trap is allowed to remain at room temperature. High purity potassium is used, as is argon zero gas. The potassium ampoules are broken in air by tapping with a hammer. The potassium remains largely unoxidized because the glass of the ampoule sticks to the potassium after it is broken, protecting almost the entire surface from contact with air.

4.2 Separation of Beam Constituents

A. Introduction

The beam emerging from the oven contains potassium atoms, argon atoms, potassium-argon molecules, argon dimers, and singlet- and triplet-state potassium dimers. In order to study the molecules by magnetic resonance, they must be separated spatially from the other constituents of the beam; this is accomplished by the deflecting magnets. Molecules make up a small fraction (less than 10^{-3}) of the beam, and are divided among many vibrational and rotational states; therefore the molecular resonance signal is very weak. To achieve a satisfactory signal-to-noise ratio, the noise background due to stray atoms must be reduced. Background suppression requires strong particle deflection as well as careful collimation and velocity selection of the beam.

Magnetic deflection is discussed in the next section. The procedures for separating and detecting particular beam species are described in section 4.2C. These procedures are determined in part by the need for a narrow resonance linewidth, which is discussed in section 4.3.

B. Beam Deflection

The fields and field gradients in the deflecting magnets are perpendicular to the axis of the apparatus. The gradients are primarily horizontal. The deflection angle of a particle emerging from such a magnet (see Fig. 4-1) is given by

$$\theta = \frac{\mu_z (\nabla H) L}{m v^2} \tag{4.1}$$

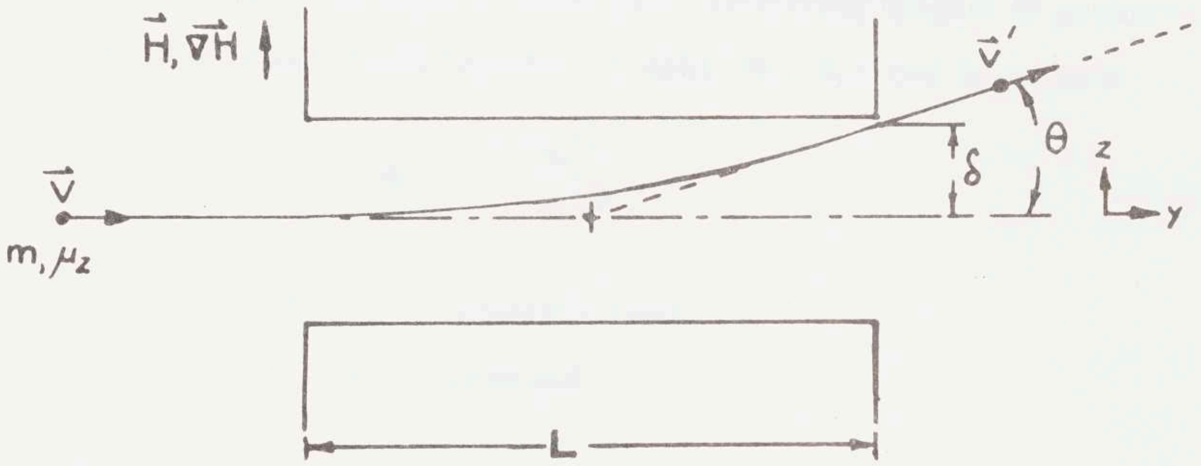

$$\theta = \frac{\mu_z(\nabla H) L}{m v^2}$$

$$\delta = \theta \frac{L}{2}$$

Fig. 4-1 Beam Deflection in Inhomogeneous Magnet.

θ = angular deflection of particle from original direction of travel

μ_z = component of particle's magnetic moment along the field

∇H = magnetic field gradient

L = length of magnet

m = particle mass

v = particle speed

Because the field gradient in a "two-wire" deflecting magnet is proportional to the magnetic field (RAM56, p. 432), Eq. 4.1 can be written

$$\theta = C \frac{\mu_z H}{m v^2} \tag{4.2}$$

H = magnetic field

C = constant

If the particle's initial velocity is directed toward the center of the magnet at an angle θ with respect to the magnet's axis, and if the particle is deflected through that angle θ, it will leave the magnet <u>on</u> the axis, not merely parallel to it. This becomes important when the source angle is varied. For each source angle, the selected particles must pass between the A and B slits, which lie on the machine axis (see Fig. 3-1); they automatically do this if the source nozzle is always aimed at the center of the A magnet.

Central to the method of separating molecules from atoms is the equality of speeds in the beam, that is, the fact that all species in a supersonic beam, regardless of mass, have the same average speed, v_o. Important also is the narrowness of the velocity distribution, which means that very few particles have speeds differing by more than 10% from the average.

As mentioned earlier, the beam consists of the following species: argon atoms and dimers, which possess no magnetic moment (and which go undetected, in any case); and four species containing potassium: potassium atoms (spin $\frac{1}{2}$), potassium-argon molecules (spin $\frac{1}{2}$), potassium dimers in the singlet spin state (spin 0), and potassium triplet dimers (spin 1). In addition, we distinguish between potassium atoms whose speeds are within the main velocity distribution (close to the average beam speed v_o), and "fast" potassium atoms, those few atoms with speed $\sqrt{2}\, v_o$. (The fast atoms undergo the same deflection as molecules of speed v_o, and are used to align the apparatus and to locate the resonance frequency.) Table T4-1 lists the beam species and their masses, speeds, magnetic moments, and deflections. For the purposes of this table and the following discussion, argon and potassium atoms are assumed to have

Table T4-1

Constituents of Atomic Beam

Species	Atomic Weight (M = 40)	Speed (v_o = av. beam speed)	Magnetic Moment (μ_o = Bohr magneton)	Angular Deflection $D \equiv \frac{C\mu_o}{M v_o^2}$
Ar atoms	M	v_o	0	0 (not detected)
Ar dimers	2M	v_o	0	0 (not detected)
K atoms	M	v_o	μ_o	DH
KAr molecules	2M	v_o	μ_o	$\frac{1}{2}$ DH
Fast K atoms	M	$\sqrt{2}\, v_o$	μ_o	$\frac{1}{2}$ DH
K_2 singlet dimers	2M	v_o	0	0
K_2 triplet dimers	2M	v_o	$2\mu_o$	DH, 0 (for $\lvert m_s \rvert = 1, 0$)

the same atomic weight (40). This is correct to $2\frac{1}{2}\%$, entirely adequate for experimental purposes. One can draw from Table T4.1 several conclusions:

1. In the same H field, potassium-argon molecules (sometimes referred to as "molecules") are deflected half as much as potassium atoms of speed v_o ("atoms").
2. Fast potassium atoms (speed $\sqrt{2}\ v_o$; called "fast atoms") are deflected the same amount as the molecules.
3. For the same deflection, molecules and fast atoms require twice the magnetic field that atoms do.
4. Singlet potassium dimers (called "dimers") are undeflected by the magnets.
5. Triplet potassium dimers with $|m_s| = 1$ travel along the same path as potassium atoms; those with $m_s = 0$ along the singlet dimer path. (Since the binding energy of triplet K_2 is 290^oK (CHU72, p. 27), compared with 5950^oK for the singlet dimers (HER50, p. 543), the triplets should not be present in significant amounts; in any case they are indistinguishable by deflection from atoms or singlet dimers.)

Using these properties, we have developed procedures for separating and observing the beam constituents. In reality the MBMR apparatus consists of two "particle filters": the source filter, made up of the source and the A magnet; and the detector filter, consisting of the B magnet and the detector. By varying the A magnet current and the source carriage position, the source filter can be set up to pass a given beam species along the machine axis. Similarly, the detector filter can be arranged, by adjusting the B magnet current and the detector position, to detect any constituent of a beam that was originally travelling along the machine axis.

A bit of nomenclature is necessary. The configuration in which the filters are set up will be written in the form 'i - j', where *i* indicates the species passed by the source filter, and *j* that passed by the detector filter. The species are labelled as follows:

a = atom = potassium atom

m = molecule = potassium-argon molecule

f = fast = fast potassium atoms

0 = no deflection (magnet current zero; source or detector on axis)

d = dimer = singlet potassium dimer (magnet current *non*zero; source or detector on axis)

x = variable (filter is tuned through its range of species)

'j*' = flop-in (detector filter is adjusted to detect particles of type 'j' that have undergone a spin-flip in the C region, i.e., a flop-in resonance; used for molecules, atoms, and fast atoms)

A picture of the beam constituents can be obtained by making a source or a detector sweep, as described in section 3.5B: the source carriage (or the detector) is moved through its range of motions while the other filter elements remain fixed; a plot is made of the detector count rate as a function of source (or detector) position. The different species in the beam appear as peaks in such a plot.

Two filter configurations are shown schematically in Fig. 4-2. Configurations such as 0-x and x-0, in which the detector or the source carriage is moved through the range while the other filter passes the

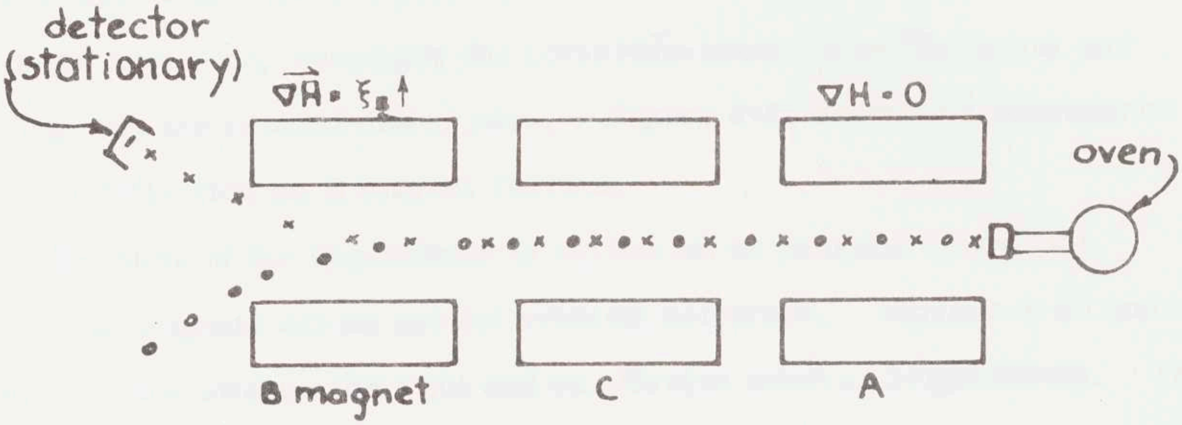

(a) 0-a configuration

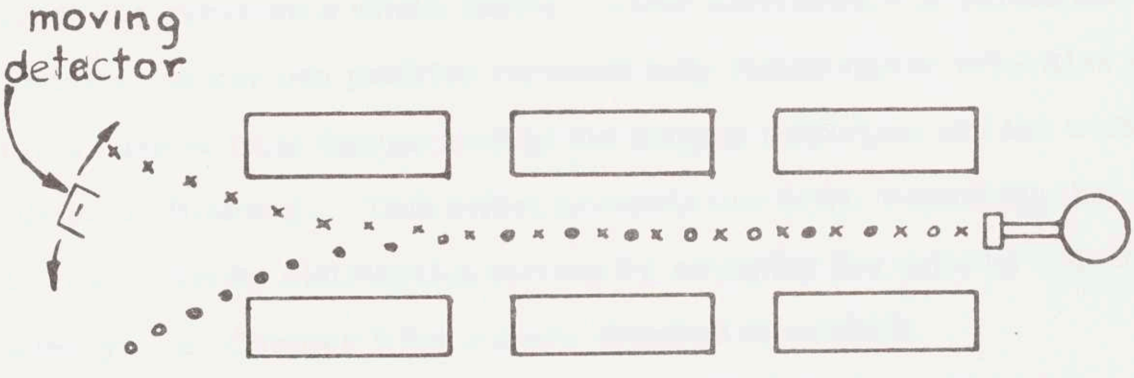

(b) 0-x configuration

Fig. 4-2 Source/Detector Configurations.

entire beam, are used to check the alignment of the machine and to calibrate the A and B magnet deflections. Figure 4-3 shows plots of typical such source and detector sweeps.

The outside lobes in Figs. 4-3a--c are caused by potassium atoms in the two possible spin states ($m_s = +\frac{1}{2}$ and $-\frac{1}{2}$). The smaller central peak is due to undeflected potassium dimers. In Fig. 4-3d the A magnet has been turned on, removing the potassium atoms from the beam and leaving only the central dimer peak. Figure 4-3e shows the dependence of beam deflection on B magnet current.

Because of the dependence of deflection on particle speed, the deflecting magnets act as spatial velocity selectors. Figures 4-3b and c show detector sweeps for a jet and an effusive source, respectively. The wider velocity distribution of the effusive beam is clearly demonstrated by the much wider deflection profile of Fig. 4-3c. It should be noted that, although the curve as a whole shows a wider distribution of velocities, the detector at any one position receives only atoms whose velocities lie within a narrow band determined by the magnet deflection and the width of the detector filament. This effect prevents one from measuring the molecular velocity distribution merely by sweeping the velocity selector frequency; see Chapter 5 for a more detailed discussion.

Figure 4-4 shows some of the filter configurations used in the search for molecules and observation of their spectra. (A complete recipe for setting up the apparatus is given in Appendix A4.1.) The detector sweeps that would be obtained from these configurations are shown beside them. (Source sweeps are not made when the velocity selector is in use because moving the source would change the effective selector asymmetry, introducing an extraneous modulation of the beam

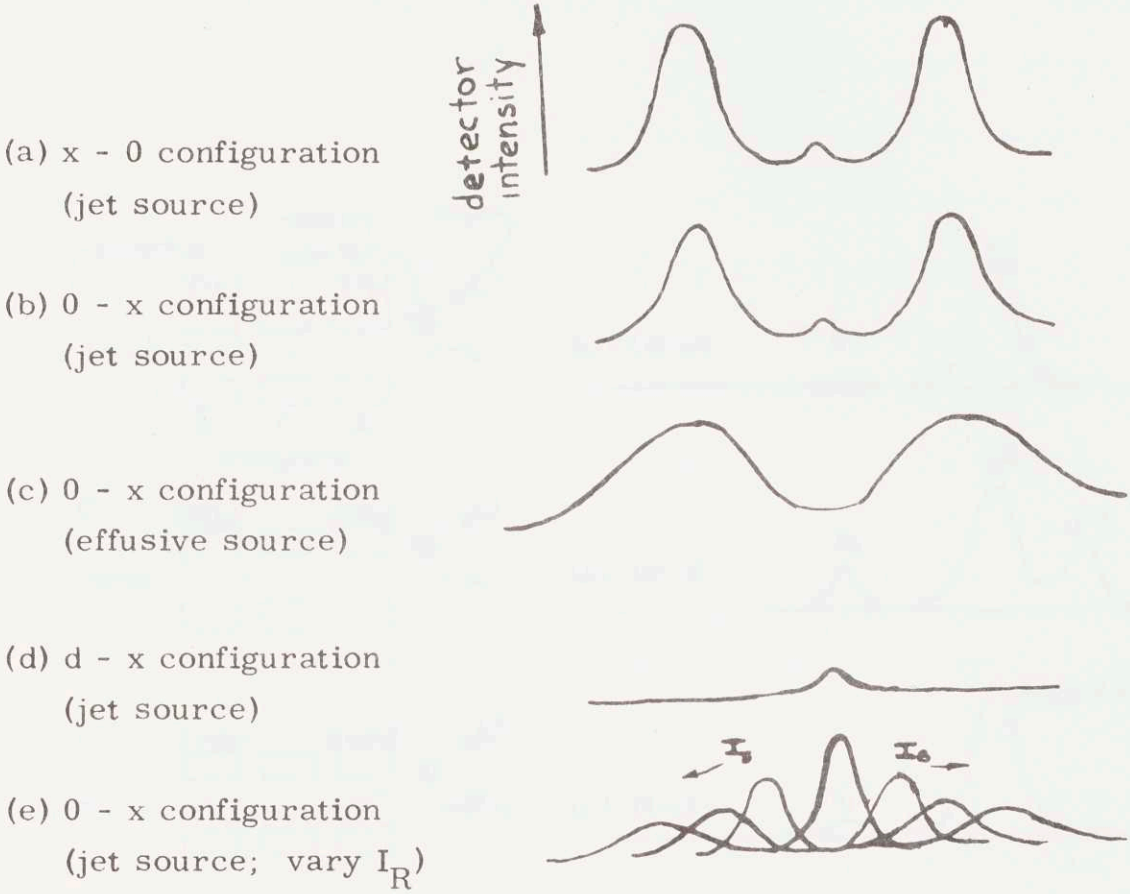

KEY

Plot	Configuration	I_A	I_B	Source Position	Detector Position
(a)	x - 0	fixed	0	varied	center
(b)	0 - x	0	fixed	center	varied
(c)	0 - x	0	fixed	center	varied
(d)	d - x	fixed	fixed	center	varied
(e)	0 - x	0	varied	center	varied

Fig. 4-3 Source and Detector Beam Profiles.

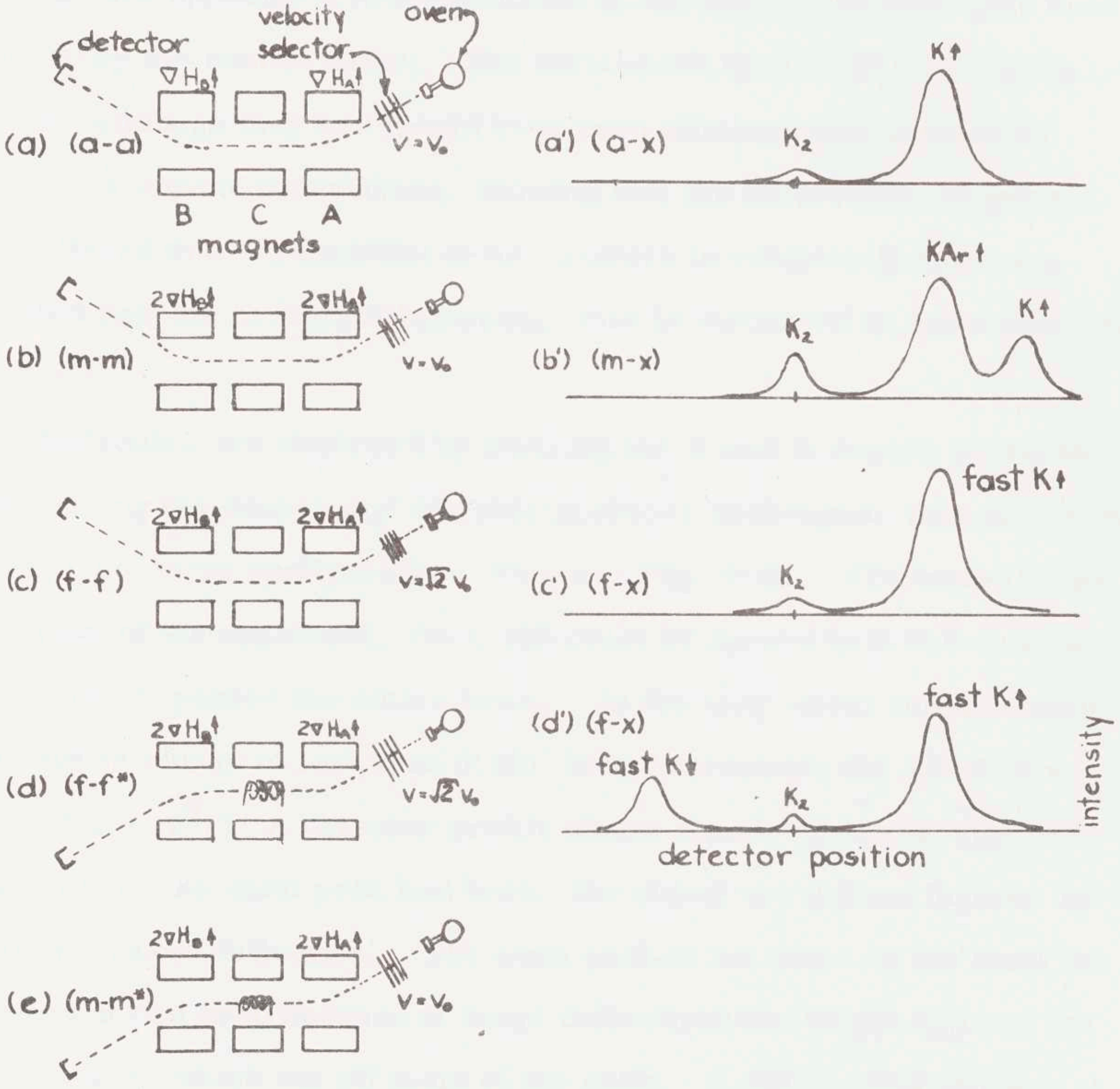

Fig. 4-4 Filter Configurations and Detector Beam Profiles.

intensity.) A discussion of these detector profiles will clarify the operation of the apparatus.

In Fig. 4-4a the apparatus has been adjusted to detect potassium atoms in one spin state. A detector profile, obtained by sweeping the detector position, shows a large off-center atom peak. No corresponding peak appears opposite it because atoms in the other spin state have been removed by the source filter. The small peak at the center is due to dimers; although they too should have been eliminated by the source filter, they appear nonetheless, showing that the filters are not perfect. It is believed that the inability of the magnets to completely filter out unwanted species is due to scattering; this is discussed in more detail in Chapter 5.

Molecules are observed by doubling the A and B magnet currents while leaving the source and detector positions unchanged: this places the filters in the m-m configuration, shown in Fig. 4-4b. (To increase the sensitivity of the apparatus, the C slit must be opened to 0.010-inch or more, until it passes the entire beam. In the atom-atom configuration the C slit is closed to less than 0.001-inch, attenuating the beam by a factor of 2×10^4.) A detector profile shows a molecule peak approximately where the atom peak had been; the atoms are pushed farther out by the increased deflection. The atom peak is not twice as far from the center as it had been because at large deflections the atoms run into the magnet walls, which cut off most of the peak. A dimer peak appears at the center of the plot, and a fourth peak occurs where one would expect spin-flipped atoms; the latter is believed due to atoms that have undergone Majorana flops between the A and B magnets.

Increasing the velocity selector frequency by a factor $\sqrt{2}$ (in practice, from 140 Hz to 200 Hz) passes fast atoms through the machine. These follow the same trajectory as the molecules and create a peak at the molecule position (see Fig. 4-4c'). The flop-in resonance position is found by turning the C magnet on and adjusting the rf frequency to resonance, as described in Appendix A4.1. Some of the fast-atom spins will be flipped, creating a peak at the flop-in position as shown in Fig. 4-4d'; the detector can then be moved to the maximum of this peak. The fast-atom resonance lineshape is used for measuring, and for minimizing, the linewidth of the resonance apparatus, as described in section 4.3.

Returning the velocity selector frequency to its original value (i.e., 140 Hz) leaves the apparatus ready to record molecular spectra.

4.3 Observation of Atomic and Molecular Spectra

A. Apparatus

To observe an atomic or molecular spectrum using the MBMR technique, one supplies radio-frequency power to the resonance coil and plots the beam intensity as a function of the rf frequency. (One could vary the strength of the C field instead of the frequency of the rf, but magnetic fields are difficult to measure accurately and adjust precisely.) In this experiment the rf is amplitude modulated, and phase sensitive detection is used to increase the signal-to-noise ratio. The frequency of the rf generator is swept electrically, and the spectrum is automatically plotted on an X-Y recorder. A block diagram of the system is shown in Fig. 4-5. Table T4.2 lists the instruments used. The rf modulator is a mercury-wetted reed relay driven by a transistor circuit that is triggered by the lock-in amplifier reference signal. The ramp generator that sweeps the frequency synthesizer consists of a ten-turn

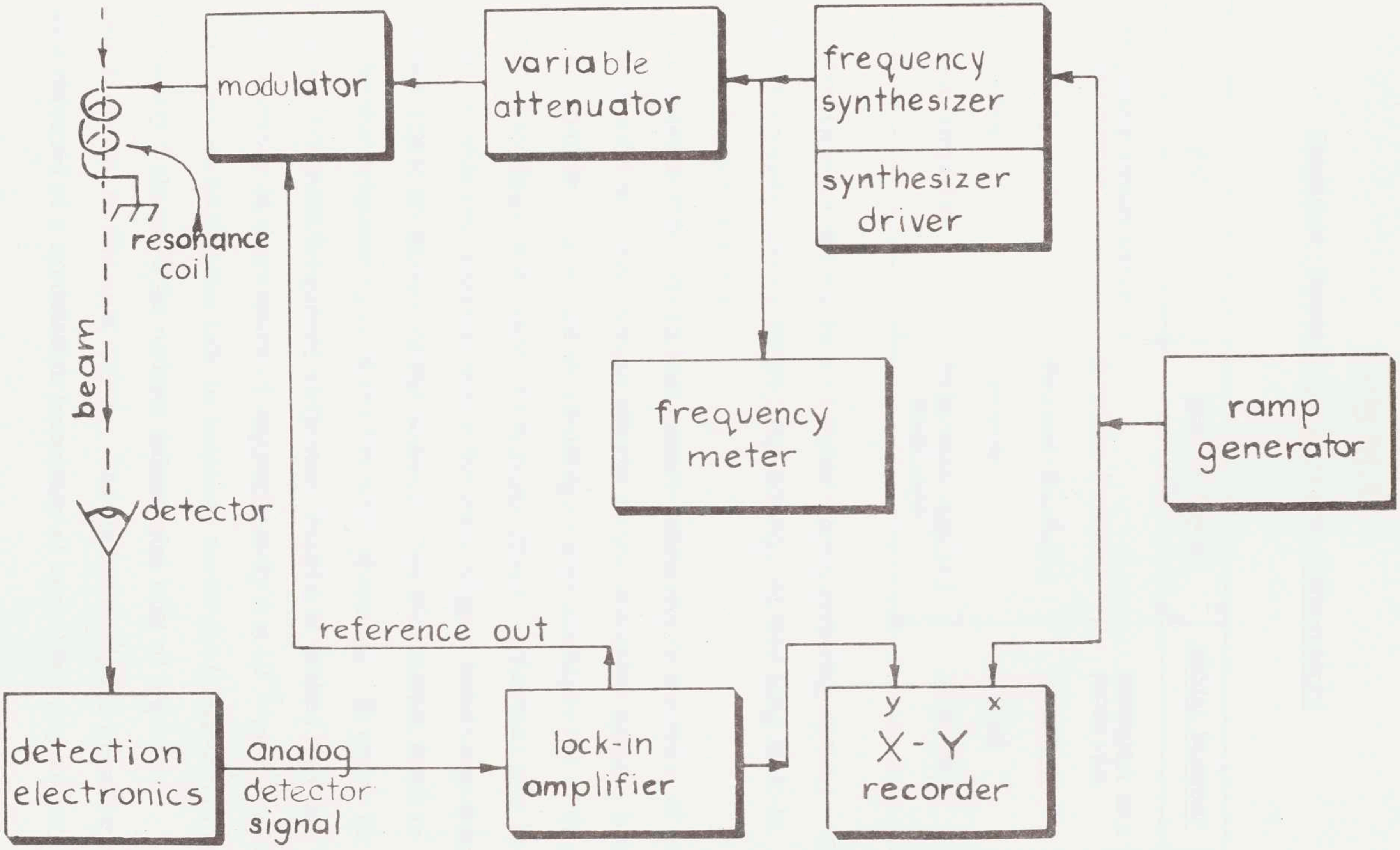

Fig. 4-5 Electronics for Spectrum Observation.

Table T4.2

Spectrum-Recording Electronic Components

Unit	Manufacturer	Model Number
Frequency synthesizer and driver	Hewlett-Packard	HP5100A and HP5110A
Frequency meter	Hewlett-Packard	HP5300A
Attenuator	Texscan	SA-58
Lock-in amplifier	Princeton Applied Research	PAR JB-5

linear potentiometer driven by a variable-speed reducing motor. This permits the frequency to be swept very slowly, so that long lock-in integration times can be used.

The noise in this experiment comes primarily in the form of non-stochastic bursts of counts whose effects on the detection system last up to several seconds. It would be advantageous to modulate the rf at a high rate, to average over each burst many times. (Another way to look at this is that one wants to move the lock-in pass band away from the characteristic frequency of the noise.) The modulation limit is imposed by the response time of the hot wire filament. In order to increase the filament frequency response, oxygen is leaked into the detector chamber at a pressure of approximately 2×10^{-6} torr. Using this technique we have been able to increase the rf modulation rate from approximately 5 Hz to 70 Hz without substantial loss of signal or apparent increase in filament noise. The optimum signal-to-noise ratio has been obtained at a modulation frequency of approximately 20 Hz.

B. Locating the Primary Resonance

In order to observe the molecular spectrum, one must place the detector in position to receive flopped-in molecules, and locate the approximate frequency of the transition. The molecular signal is too weak to be used for this preliminary adjustment; the fast atom resonance, however, is admirable for the purpose. As discussed in Chapter 2, the center of the molecular spectrum ($m_N = 0$) coincides approximately with the atomic Zeeman frequency. Furthermore, the fast atoms are deflected along the same path as the molecules; thus they provide references for both frequency and deflection.

Part E of Appendix A4.1 describes the method of locating the fast-atom flop-in resonance. In addition to the primary resonance ($\Delta m_F = 1$), other atomic transitions can be found; these are discussed in section 4.3D, along with methods for distinguishing them from the primary resonance. The next section describes the use of the fast atoms in minimizing the apparatus linewidth.

C. Apparatus Linewidth

The inherent linewidth of the MBMR apparatus is determined principally by the length of the resonance coil and the velocity of the beam (see Appendix A4.2). For a beam with a narrow velocity distribution the full width at half maximum (FWHM) of the line is approximately

$$\Delta\nu = 0.8 \frac{v_o}{L} \qquad (4.3)$$

where

$\Delta\nu$ = FWHM (Hz)

L = coil length

v_o = average particle velocity

Field inhomogeneities in the resonance region increase the linewidth and alter the shape of the line. In effect, they cause atoms in different parts of the coil to resonate at different frequencies; the total lineshape becomes a superposition of several different lines, each with a width given by Eq. 4.3. When examining complex spectra, one wants an apparatus line narrow enough to resolve the spectral structure, and symmetrical enough to reveal the shape of the spectrum without imposing an extraneous shape of its own. For these reasons it is desirable to make the magnetic field in the C region as homogenous as possible.

Considerable pains were taken in the construction of the C magnet to make the pole faces as smooth and as parallel as possible. A measurement of the C field with the magnet out of the apparatus showed that the field strength varies by less than 0.2% over the central region (1 x 6 inches) of the 3 x 10-inch pole face. As described in Chapter 3, the pole tips are made of low-coercive force alloy, to minimize tangential fields. The pole faces were surface-ground, and are spaced apart by four aluminum blocks lapped to within 0.0005-inch of the same height. Unfortunately, it was found that when the C magnet is installed in the MBMR apparatus, a great deal of magnetic flux leaks from the A and B magnets into the C magnet, broadening and skewing the line.

The linewidth has been reduced by three tactics. First, time variations of the C field were eliminated by carefully current-regulating the A, B, and C magnet power supplies. (The A and B magnet currents have to be specially regulated because small changes in them affect the C field via the flux linking the magnets.) Second, the flux leakage was considerably reduced by installing magnetic shields between the C magnet and the A and B magnets. These shields are described in Appendix A4.4. Third, the remaining inhomogeneity is minimized by adjusting the A and B magnet currents. This must be done each time the apparatus is set up, and is the last magnet adjustment made before recording the molecular spectrum.

To minimize the linewidth, one uses the two resonance coils mounted in the C magnet. The fast-atom Zeeman frequency is measured with each coil, the difference between the frequencies giving a measure of the C field gradient. The A and B magnet currents are adjusted to make the resonance frequencies as nearly equal as possible. This is the condition for zero linear gradient along the C magnet, and produces the narrowest linewidth. A parabolic variation of field strength with distance is still possible, and in fact limits the narrowness of the line: contrary to the prediction of Eq. 4.3, a very long coil does not yield a narrower line, for it samples increased field differences between its center and its ends. (Strictly speaking, one would expect the narrowest line to occur when the field minimum is at the center of the coil used for the spectral measurement. In practice, one simply varies the A and B currents until the minimum linewidth is obtained.) The small changes in the A and B currents required to reduce the linewidth do not affect the beam deflection significantly, particularly at high field strengths where the deflection begins to saturate. We have found that the A and B magnets must be operated at approximately the same field strength in order to get the narrowest line.

Using the procedures described above, we have obtained fast-atom lines as narrow as 20 - 23 kHz, corresponding to linewidths of approximately 16 kHz for molecules (or atoms) moving with speed v_o. This is completely adequate for resolving the molecular spectrum, whose major structures are separated by approximately 75 kHz.

When measuring the apparatus linewidth or observing spectra, one must be careful not to power broaden the line. Power broadening is avoided by increasing the rf voltage from zero until the flop-in signal reaches a maximum, then decreasing it slightly.

The condition for maximum resonance signal corresponds to the electron spin performing a 180° precession about the (rotating) rf magnetic field. Because molecules spend a longer time in the resonance coil than fast atoms, they require a weaker rotating field in order to make a 180° precession during their stay. Therefore, the rf voltage is reduced by a factor $1/\sqrt{2}$ when changing from fast atoms to molecules.

D. Subsidiary Atomic Resonances

The primary atomic resonance is due to a Zeeman transition in ^{39}K between states ($F = 2$, $m_F = -1$) and ($F = 2$, $m_F = -2$), that is, with $\Delta F = 0$, $\Delta m_F = -1$. Up to four other atomic transitions, described below, can be observed, and it is important to distinguish them from the primary resonance, for several reasons. First, only the molecular spectrum coinciding with the primary atomic transition is intense enough to be observed; searching for it in the neighborhood of the subsidiary resonances would be fruitless. Second, adjusting the rf power to one of the subsidiary resonances could power broaden the primary atomic resonance and the molecular transitions. Finally, one must be aware of the existence of these transitions when observing the molecular spectrum without a velocity selector: the subsidiary resonances can superimpose extraneous maxima on the spectrum.

One subsidiary resonance is due to the $F = 2$ ($m_F = -1 \rightarrow -2$)

transition in ^{41}K, which makes up 6% of naturally occurring potassium. The hyperfine separation in ^{41}K is 254 MHz (RAM56, p. 255), compared with 462 MHz for the more abundant (93%) ^{39}K. As shown in Appendix A4.2, the lower hyperfine frequency increases the Zeeman frequency in a given magnetic field. Because the ^{41}K transition has the same quantum numbers as the ^{39}K primary transition, it has the same dependence on rf power, that is, it is easily overdriven and power broadened; its low intensity is due not to a smaller transition probability, but to the small number of ^{41}K atoms in the beam.

Up to three transitions in ^{39}K can be observed for which $\Delta m_F > 1$: $F = 2$, $m_F = 0 \rightarrow -2$, $1 \rightarrow -2$, and $2 \rightarrow -2$. Their frequencies are calculated in Appendix A4.2. Because $\Delta m_F > 1$, these transitions are forbidden by magnetic dipole selection rules; they proceed by two photon processes, with small probability. Consequently, the resonances have low intensities, and cannot be overdriven by the frequency synthesizer used in this experiment; this characteristic is used to identify these resonances.

The method for identifying a weak resonance is as follows. Increase the rf voltage from zero. If the flop-in signal reaches a maximum and begins to decrease at a moderate voltage (less than $\frac{1}{2}$ volt p-p in a 2'' resonance coil at 15 MHz) the resonance is probably the $\Delta m_F = 1$ transition in ^{41}K; look at a lower frequency for the primary resonance. If, instead, the signal intensity increases monotonically as the rf voltage is raised to a high value, the resonance is one of the $\Delta m_F > 1$ transitions in ^{41}K; the primary resonance is at a higher frequency.

APPENDIX A4.1

RECIPE FOR APPARATUS ADJUSTMENT

A. Initial Alignment

The following procedure assumes that the apparatus is operating with an alkali beam.

1. Set detector and source carriage on axis.
2. Open C slit wide (more than four turns).
3. Remove velocity selector from beam path.
4. Adjust oven and skimmer to achieve optimum alignment. Monitor with detector signal. Keep count rate below 700,000 per second by attenuating the beam with the velocity selector; lower selector into beam path, set frequency at 140 Hz, and rotate selector to reduce count rate to desired value.
5. Adjust detector position (slightly) to maximize signal.
6. Narrow C slit until it intersects the beam. Adjust its lateral position to remaximize signal. This lines up C slit with beam axis.
7. Close C slit completely.
8. Remove velocity selector from beam.
9. Open C slit (to less than 0.001", i.e., 1/8 turn of adjusting knob) until detector count rate is approximately 105/second.

B. Atom Peak

1. Set I_A to 0.8 amps (approximately).
2. Move source carriage to obtain maximum signal.
3. Place velocity selector in beam, set frequency to 140 Hz, and rotate selector to maximize signal. (This sets asymmetry

approximately at zero.)

4. Set I_B to 1.0 amp (approximately).
5. Move detector to maximize signal. Apparatus is adjusted to a-a configuration. (If desired, sweep detector to obtain beam profile.)

C. Fast-Atom Peak

1. Double I_A and I_B.
2. Open C slit to 0.010'' or more.
3. Set velocity selector frequency to 200 Hz ($\cong 140\sqrt{2}$).
4. Readjust detector position if necessary to maximize signal. Apparatus is now adjusted to detect fast atoms.

D. Molecule Search

1. Reduce velocity selector frequency to 140 Hz. (Sets up molecule configuration.)
2. Sweep detector to obtain beam profile.
3. Adjust C slit width, and magnet currents, velocity selector frequency, and oven position slightly to maximize the height of the molecule peak and increase the separation between molecules and atoms.

E. Locating Resonance

1. Increase the velocity selector frequency to 200 Hz (return to fast atoms).
2. Using the built-in Hall probe as a monitor, set the C field to the value corresponding to the desired resonance frequency. The relation between magnetic field and Zeeman frequency is given in Appendix A4.2.

3. Tune rf synthesizer to resonance frequency. Use sufficient rf voltage on resonance coil; this depends upon frequency and coil size.
4. Adjust C-magnet current slowly until detector count rate decreases, indicating flop-out resonance.
5. Move detector to flop-in position.
6. Adjust detector accelerating voltages (filament bias and backing screen potentials) to maximize signal.
7. Reduce velocity selector frequency to 140 Hz (or frequency found in D. 3).
8. Sweep synthesizer frequency to observe molecular spectrum.

APPENDIX A4.2

ATOMIC ZEEMAN FREQUENCIES IN POTASSIUM

The energy levels of a ground-state alkali atom in a magnetic field are given by the Breit-Rabi formula, Eq. A4.2/1 (RAM56, p. 86). This formula is valid for any atom with total electronic angular momentum $J = \frac{1}{2}$ $(\vec{J} = \vec{L} + \vec{S})$; in ground-state alkalis, $L = 0$, $S = \frac{1}{2}$.

$$W(F, m) = -\frac{\Delta W}{2(2I+1)} - \frac{\mu_I}{I} H_o m \pm \frac{\Delta W}{2} \sqrt{1 + \frac{4m}{2I+1} x + x^2} \qquad \text{(A4.2/1)}$$

$W(F, m)$ = energy of state (F, m)

I = nuclear spin ($I = 3/2$ for potassium)

F = $I \pm \frac{1}{2}$ = total angular momentum

m = m_F = magnetic quantum number

ΔW = hyperfine separation

H_o = magnetic field strength

x = $(g_s - g_I)\, \mu_o H_o / \Delta W$

g_I = $-\mu_I / I\mu_o$

μ_o = Bohr magneton $\left(\frac{\mu_o}{h} = 1.398 \text{ MHz/Gauss}\right)$

Fuller and Cohen give the following values for potassium (FUL65, p. 67):

$\mu_I = +0.3915\, \mu_N$ (^{39}K) $\qquad \Delta W = 461.720$ MHz (^{39}K)

$\mu_I = +0.2153\, \mu_N$ (^{41}K) $\qquad \Delta W = 254.018$ MHz (^{41}K)

and

μ_N = nuclear magneton $\left(\frac{\mu_N}{h} = 762.295 \text{ Hz/Gauss (RAM56, p. 418)}\right)$

In this experiment we observe transitions from states with ($F = 2$, $m = m_o$) to the state ($F = 2$, $m = -2$). The frequency of such a transition is, using Eq. A4.2/1,

$$\nu_{m_o, -2} = -\frac{2\mu_I}{3} H_o (m_o + 2) + \frac{\Delta W}{2}\left[\sqrt{1 + m_o x + x^2} - 1 + x\right] \qquad \text{(A4.2/2)}$$

The chart below lists the frequencies of transitions in ^{39}K with m_o = -1, 0, 1, and 2, and for transitions in ^{41}K with m_o = -1. The primary atomic transition in this experiment is (F = 2, m = -1) to (F = 2, m = -2) in ^{39}K.

H_o (Gauss)	^{39}K							^{41}K
	Δm = -1	Δm = -2		Δm = -3		Δm = -4		Δm = -1
	ν (MHz)	ν (MHz)	ν/2 (MHz)	ν (MHz)	ν/3 (MHz)	ν (MHz)	ν/4 (MHz)	ν (MHz)
19.61	15	29.03	14.52	42.27	14.09	54.82	13.71	16.17
25.45	20	38.30	19.15	55.26	18.42	71.15	17.79	22.05
36.28	30	56.23	28.11	79.82	26.60	101.44	25.36	34.45
46.19	40	73.42	36.71	102.72	34.24	129.14	32.28	47.56
55.32	50	89.93	44.97					61.19
63.83	60	105.87	52.94					75.19

APPENDIX A4.3

APPARATUS LINEWIDTH

The resonance linewidth of an MBMR apparatus is primarily determined by the transit time of beam particles through the resonance coil. The transition probability P for a particle that spends a time T in the coil is (RAM56, p. 119)

$$P = \frac{\omega_1^2}{(\Delta\omega)^2 + \omega_1^2} \sin^2\left[\tfrac{1}{2}\sqrt{(\Delta\omega)^2 + \omega_1^2}\; T\right] \qquad \text{(A4.3/1)}$$

where $\Delta\omega = \omega_o - \omega$

ω_o = resonance frequency

ω = frequency of applied (rotating) rf field

$\omega_1 = \gamma H_1$ = precession frequency of particle with gyromagnetic ratio γ about rotating magnetic field of strength H_1. (Thus ω_1 is proportional to the applied rf voltage.)

P is a function of ω, and depends upon the values of ω_1 and T as parameters. Since $T = L/v_o$, where L = coil length and v_o = particle velocity, Eq. A4.3/1 applies only to beams with narrow velocity spreads.

P can be written

$$P = \frac{1}{1 + y^2} \sin^2\left[\frac{\omega_1 T}{2}\sqrt{1 + y^2}\right] \qquad \text{(A4.3/2)}$$

where $y = \frac{\Delta\omega}{\omega_1}$. At resonance $\omega = \omega_o$, so $\Delta\omega = 0$ and $y = 0$, thus

$$P(\omega_o) = \sin^2\left(\frac{\omega_1 T}{2}\right) \qquad \text{(A4.3/3)}$$

To calculate the full width at half maximum of the line, we must find the frequency ω for which $P(\omega) = \frac{1}{2} P(\omega_o)$. Defining

$$x = \sqrt{1 + y^2} \qquad \text{(A4. 3/4)}$$

we have the condition

$$\frac{1}{x^2} \sin^2 \left(\frac{\omega_1 T}{2} x\right) = \sin^2 \left(\frac{\omega_1 T}{2}\right) \qquad \text{(A4. 3/5)}$$

or

$$\sin \left(x \frac{\omega_1 T}{2}\right) = x \sin \left(\frac{\omega_1 T}{2}\right) \qquad \text{(A4. 3/6)}$$

Solving this equation for x determines $\frac{\Delta\omega}{\omega_1}$, which in turn gives the full width at half maximum $\Delta\nu$, in hertz:

$$\Delta\nu = 2 \frac{\Delta\omega}{2\pi} = \frac{2\omega_1}{2\pi} y = \frac{2\omega_1}{2\pi}\sqrt{x^2 - 1} = \frac{2}{\pi} \frac{1}{T} \left(\frac{\omega_1 T}{2}\right) \sqrt{x^2 - 1} \qquad \text{(A4. 3/7)}$$

Since we specify the product $\omega_1 T/2$, Eq. A4. 3/7 determines $\Delta\nu$ in terms of T, or L/v_o.

The values of $\Delta\nu$ for several values of $\omega_1 T/2$ are given below, with the corresponding resonance transition probability.

$\frac{\omega_1 T}{2}$	$\Delta\nu \cdot T$	$P(\omega_o)$
$\frac{\pi}{2}$	0.799	1
$\frac{\pi}{4}$	0.866	$\frac{1}{2}$
$\frac{\pi}{6}$	0.878	$\frac{1}{4}$
$\frac{\pi}{10}$	0.883	0.1

APPENDIX A4.4

MAGNET SHIELDS

Flux leakage into the C magnet from the deflecting magnets is reduced by two magnetic shields that separate the C magnet from the A and B magnets. Figure A4.4-1 shows a cross section of the magnet chamber, with one of the shields in place. The shields are made in two parts, one fitting around the outside of the magnet chamber, the other inside. They consist of three layers of 0.020-inch thick metal sheet, separated by two sheets of 1/32-inch plastic. The inside sections are made of mu metal, while the outside sections are cold rolled steel; neither metal is annealed. Half-inch diameter holes through the inside sections provide passage for the beam.

Prior to installation of the shields the narrowest atomic linewidth attainable was 60 kHz. With the shields in place, adjusting the A and B magnet currents can produce atomic resonances between 18 and 25 kHz wide, which is comparable to the natural linewidth of 18 kHz predicted in Appendix A4.3 for a coil 4.0 cm long and a beam velocity of 9×10^4 cm/sec.

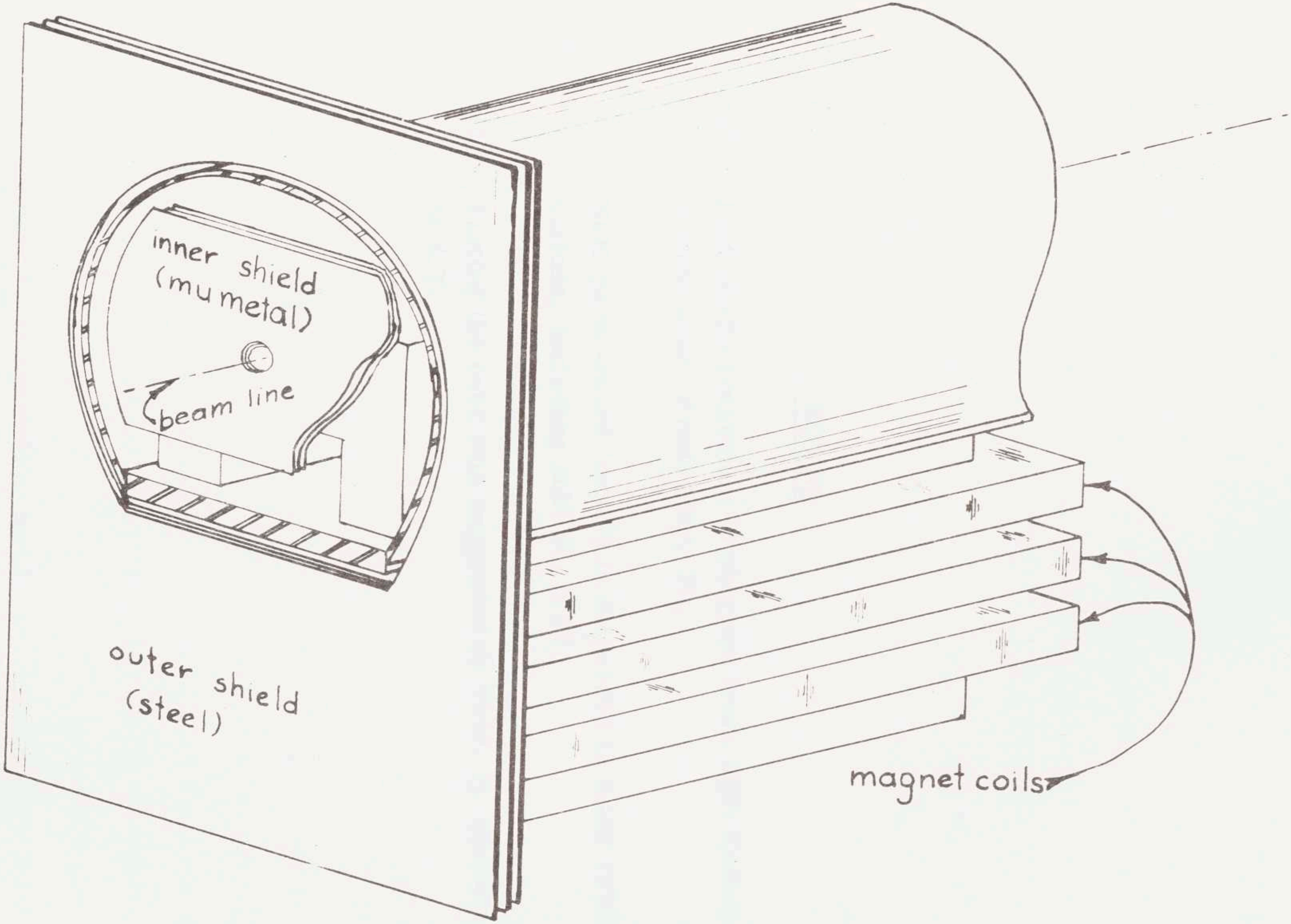

Fig. A4.4-1 Magnet Shield.

NOTES

(1) High purity potassium is obtained from MSA Research Corporation, Evans City, Pa.

(2) NaK (pronounced "nack") is discussed in many publications, including MAU67, p. 29.

(3) Plating the oven was suggested by Prof. A. Bement, M. I. T.

CHAPTER 5

RESULTS AND CONCLUSIONS

5.1 MBMR Apparatus Operating Characteristics

A. Molecule--Atom Separation

A prerequisite for observing the molecular spectrum is the ability of the apparatus to separate molecules from the large flux of atoms in the beam. The requirements for separation--velocity selector, narrow slits, beam height limiter, strong magnetic deflection--are discussed in Chapter 4. The degree of separation is observed by adjusting the source and detector filters to pass molecules (that is, by placing them in the m-m configuration of section 4.2B) and recording the beam intensity while sweeping the detector through its range of motion. Figure 5-1 is such a plot, taken with $I_A = 1.9$ A and $I_B = 1.8$ A; the oven temperature was 500^oC. It shows that the fraction of atoms at the molecule position is less than 2%.

B. Molecule Fraction in Beam

The fraction of molecules in the beam is measured by comparing the molecule flux in the m-m configuration with the atom flux in the a-a configuration. Because the atom flux is so intense, however, the beam must be attenuated by the C slit to avoid saturating the detector; the amount of attenuation must then be measured. Specifically, the following technique has been used. The apparatus was adjusted to the m-m configuration with the C slit 0.010-inch wide (not obstructing the beam), and the molecule count rate was recorded. The C slit was then closed almost completely and the A and B magnets were adjusted to pass atoms to the detector; that is, the apparatus was changed to the a-a configuration. In doing this, neither the source nor the detector was moved, so

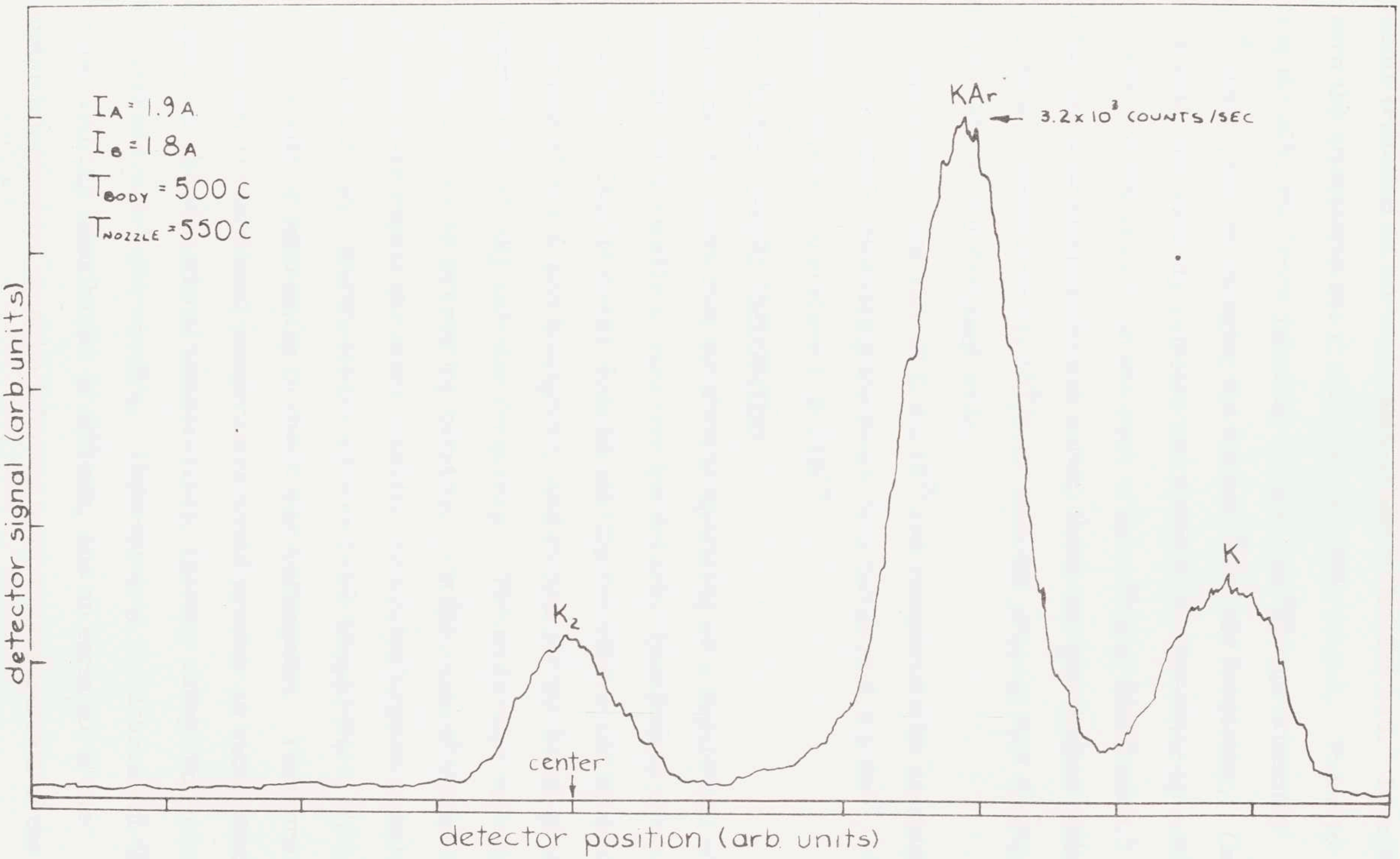

Fig. 5-1 Beam Profile in Molecule Configuration.

the atoms travelled on the same path as the molecules had. In order to measure the attenuation the C slit was opened in stages. Prior to opening the slit, the beam intensity was reduced to approximately 2×10^4 counts/sec by changing the velocity selector frequency. (In other words, the velocity selector was used as an attenuator by selecting atoms with speeds away from the peak of the velocity distribution.) After the selector attenuation was noted, the C slit was opened until the count rate was approximately 10^5/sec; then the process was repeated until the C slit was 0.010-inch wide.

A molecule count rate of 3.2×10^3 was compared with an atom rate of 1.43×10^5 after attenuating the beam by a factor of 8.2×10^{-3}. The molecule fraction is therefore 1.8×10^{-4}.

C. Beam Velocity Distribution

In order to verify that the oven is operating as a supersonic source, it is sometimes desirable to measure the velocity distribution of the atomic beam. This is easily done by placing the source and detector on axis, turning off the A and B magnets, and measuring the beam intensity as a function of velocity selector frequency. The molecular velocity distribution is also an interesting quantity. On the basis of equilibrium kinetic theory we expect the more massive molecules to have a narrower velocity distribution, and therefore a lower beam temperature, than the atoms; it would be interesting to check this assumption. Furthermore, the molecular translational temperature would provide an upper limit for the rotational and vibrational temperatures, thereby aiding interpretation of the observed molecular spectra. Unfortunately, measurement of the molecular velocity distribution is difficult, and an estimate of the molecular temperature must be inferred from a measurement of the K_2

dimer velocity width.

As mentioned in section 4.2, the fact that the deflecting magnets act as velocity selectors prevents one from readily measuring the molecular velocity distribution. Chu (CHU72,p.139), for example, measured the velocity distribution of CsHg and Cs in a jet beam and found the two species to have the same relative velocity width. We have found a similar result in a measurement of KAr. It is believed that both results are artifacts of the magnetic deflection.

Measuring the distribution of a deflected beam merely by changing the velocity selector frequency yields a velocity distribution characteristic of the magnets. However, a technique does exist for measuring the distribution of a deflected atom beam: with the source placed on axis and I_A set to zero (but $I_B \neq 0$), the detector position is adjusted to maximize the observed beam intensity for each velocity selector frequency. A plot made by this method is shown in Fig. 5-2a. An effusive source, having a broad velocity distribution, was used. Figure 5-2b was obtained under the same conditions, but with the detector held fixed at the position for maximum intensity; clearly it does not reflect the velocity distribution of the source. For Fig. 5-2c, I_B was set to zero and the detector was placed on the machine axis. In this configuration the velocity distribution may be observed directly.

Unfortunately, this technique is not applicable to molecules because both the source filter and the detector filter are necessary for separating the molecules from the atoms, and both would have to be adjusted as the velocity frequency was changed. Moving the source, however, would change the effective asymmetry of the velocity selector, altering the observed velocity. In order for this method to work, the

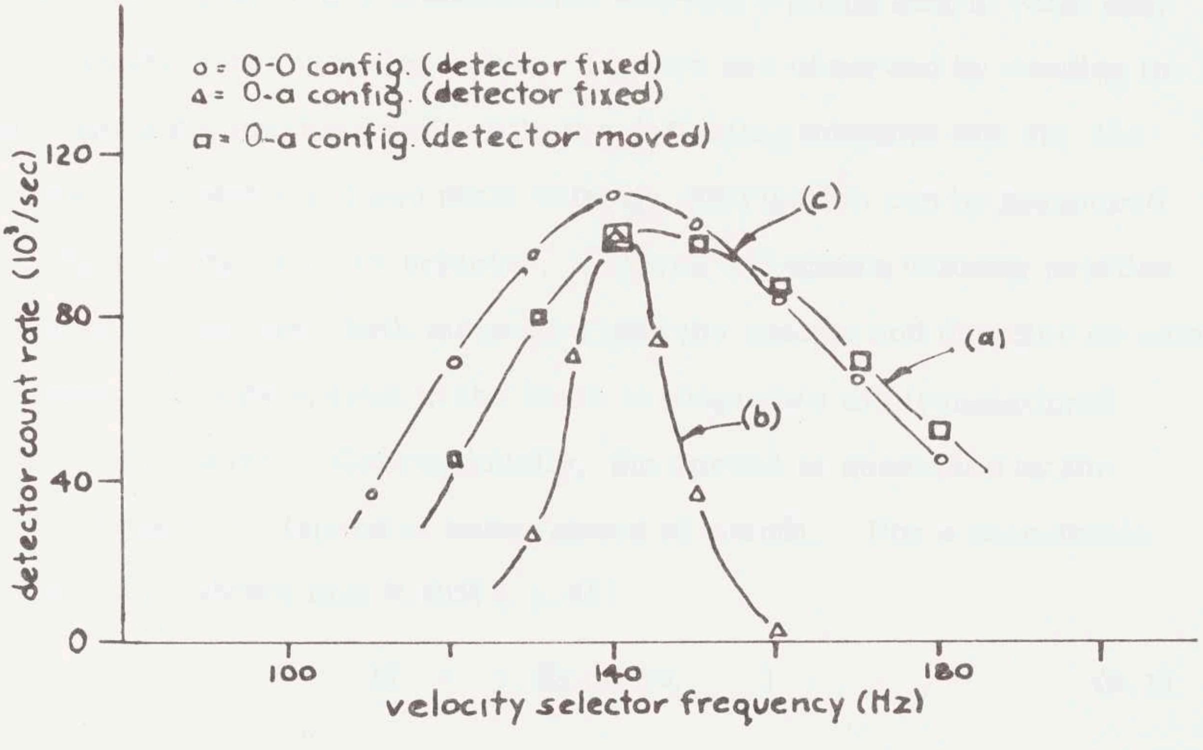

Fig. 5-2 Velocity Distribution Measurements.

velocity selector rotation and the source position would have to be precisely calibrated with respect to each other. An alternative procedure would be to adjust the A and B magnet currents to maximize the molecule count rate as the velocity selector frequency was changed. This method has not been tried.

An estimate of the relative translational temperatures of molecules and atoms can be obtained indirectly, by measuring the K_2 dimer velocity distribution: the dimers have the same mass as the van der Waals molecules, and if translational thermal equilibrium is valid they will have the same velocity width. Dimers are observed by sending the beam along the machine axis while the deflecting magnets are on; the dimers are undeflected and their velocity distribution can be measured directly with the velocity selector. Figure 5-3 shows velocity profiles of atoms and dimers, both measured with the source and detector on axis.

The velocity spread in the beam is related to the translational beam temperature. Conventionally, the spread is described by the Mach number M = (speed of beam/speed of sound). For a monatomic gas it can be shown that (CHU72, p. 42)

$$M = 1.82\,(u/\Delta v_{beam}) \tag{5.1}$$

where u = beam speed

Δv_{beam} = FWHM of beam velocity distribution

The source and beam temperatures, T_o and T_b, are related by (SHA53, p. 80)

$$\frac{T_b}{T_o} = \frac{3}{M^2} \tag{5.2}$$

Gordon et al. (GOR71) have pointed out that Eqs. 5.1 and 5.2 hold for

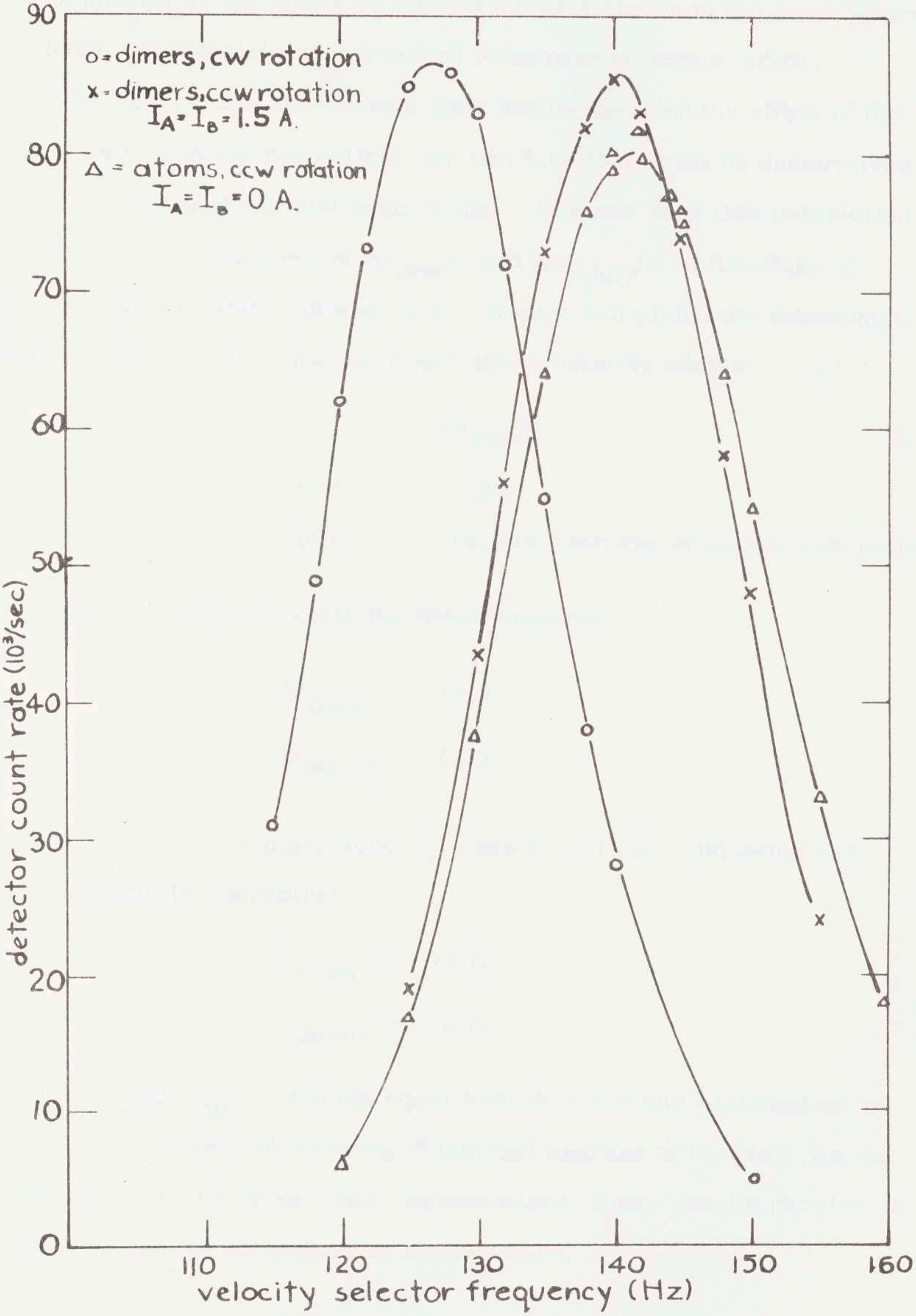

Fig. 5-3 Velocity Distribution Measurements of Atoms and Dimers.

dimers as well as for atoms in the downstream region of the beam where rotational, vibrational, and chemical relaxation no longer occur.

The observed beam velocity distribution includes the effect of the 10% velocity selector resolution; the two functions must be deconvolved in order to obtain the actual beam width. Chu has done this calculation (CHU72, p. 133); his plots of $\Delta v_{obs}/u$ and $\Delta v_{beam}/u$ as functions of Mach number are shown in Fig. 5-4. Figure 5-3 yields the following values for the experimental atom and dimer velocity widths:

	$\Delta v_{obs}/u$
atom:	16%
dimer:	15.25% (average of cw and ccw plots)

From Fig. 5-4 we then obtain the Mach numbers

$$M_{atom} = 13.7$$

$$M_{dimer} = 14.7$$

for a source nozzle temperature $T_o = 600\ C = 875\ K$. Equation 5.2 gives the beam temperatures

$$T_{atom} = 14\ K$$

$$T_{dimer} = 12\ K$$

That T_{atom} and T_{dimer} are not equal indicates that our assumptions of thermal equilibrium and freezing of internal degrees of freedom are not entirely consistent with the data; nevertheless, these results provide us with an estimate of the molecular temperature.

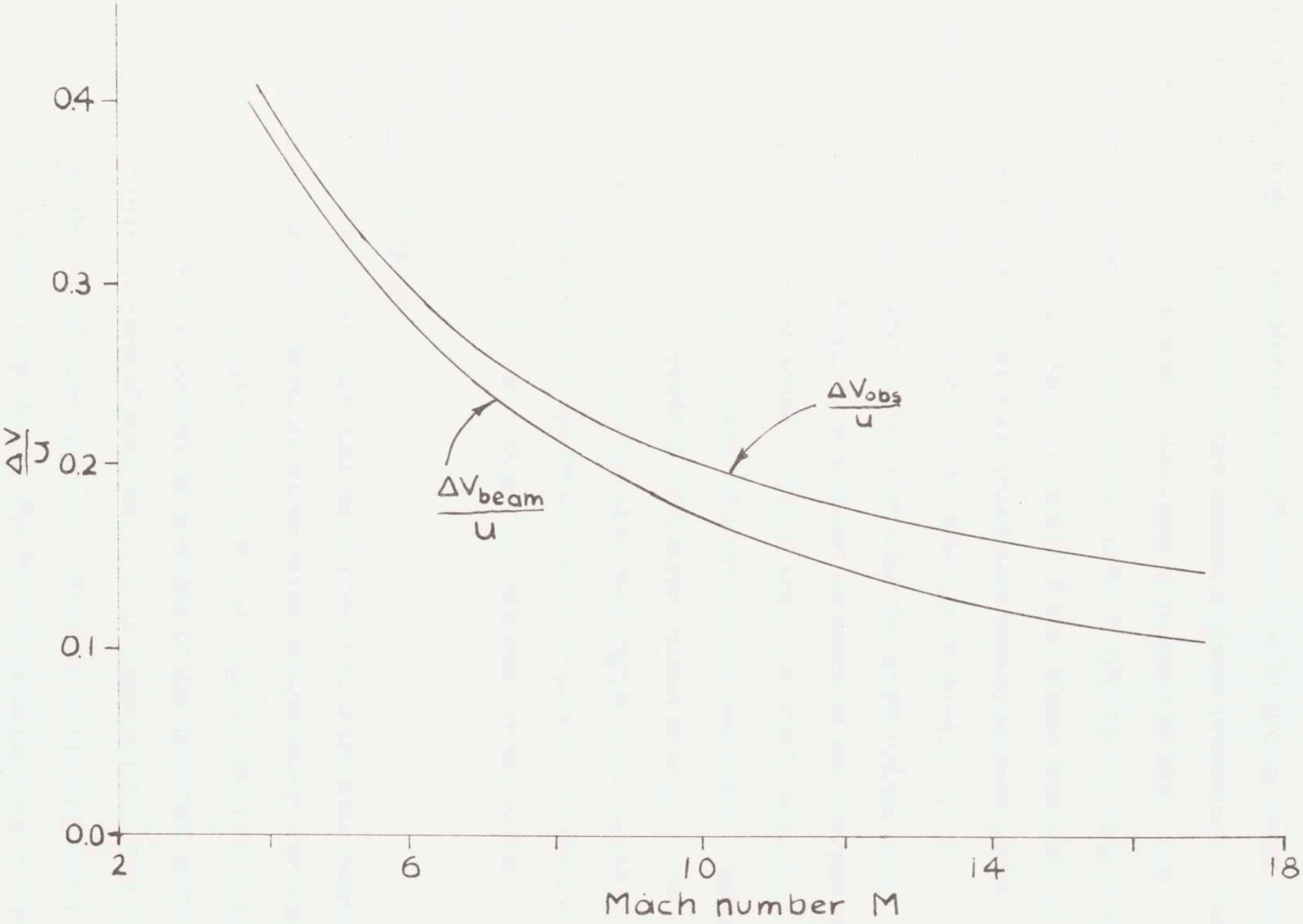

Fig. 5-4 Relation Between Mach Number and Beam Velocity-Distribution Width.

5.2 Molecular Spectra

Observations of the molecular spectrum have been made using two approaches: high-resolution measurements in a frequency range approximately 250 kHz on either side of the atomic Zeeman frequency, using a 4 cm-long resonance coil with a linewidth of roughly 20 kHz; and relatively low resolution measurements up to 2 MHz to one side of the Zeeman frequency, using a shorter coil (2.8 cm) whose linewidth is between 40 and 60 kHz. The high-resolution measurements yield so-called "near" spectra (close to the Zeeman frequency and the center of the molecular spectrum), which resemble the hypothetical curve predicted in Fig. 2-8; from them a direct estimate of the average spin-rotation constant can be obtained. The 2 MHz, or "far", spectra include contributions from all internal states of the molecule. Because few states contribute to transitions with large values of m_N, a wide-linewidth coil is used to increase the observed signal at the expense of resolution. By fitting the far spectrum with a computer calculation based on Eqs. 2.39--2.42, one can get an estimate for the radial dependence of γ.

A. Near Spectrum

Figure 5-5 shows an experimentally observed molecular spectrum. The error bars are limits between which three independently recorded spectra lie. (The three spectra were taken at slightly different magnetic fields and were matched as closely as possible to the spectrum shown.) It will be noted that the central peak ($m_N = 0$) is asymmetric; this is a feature found in almost all near spectra. Because of the imperfect separation of molecules from atoms, the central peak contains a contribution from atomic Zeeman transitions; the hyperfine shift and the

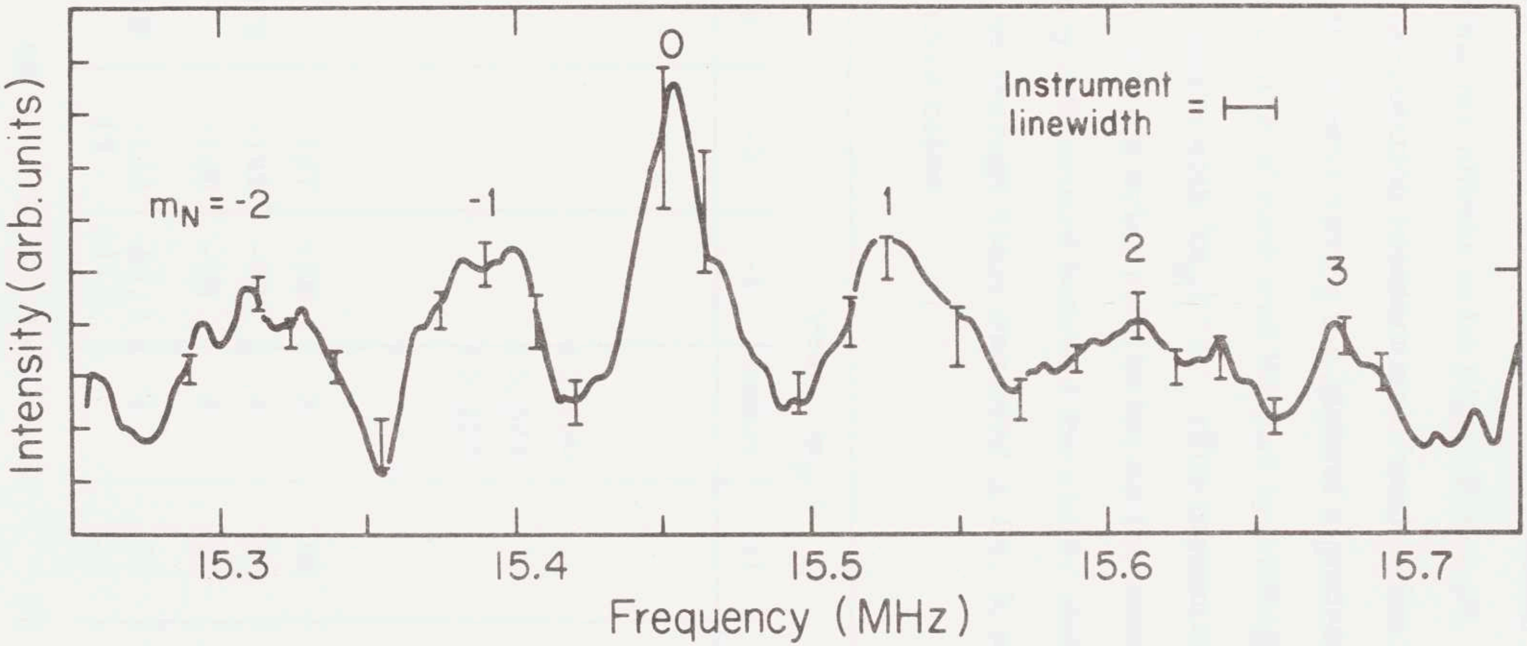

Fig. 5-5 Experimental KAr Spectrum.

second-order frequency terms discussed in Chapter 2 combine to shift this atomic resonance with respect to the molecular $m_N = 0$ transition, causing the asymmetry. Measurements at higher magnetic fields would increase the hyperfine shift and decrease the contribution of second-order terms, thereby enabling the effects to be better resolved.

The average spin-rotation constant was found in the following way. The three experimental curves having the highest signal-to-noise ratio were selected. The center of each was located by folding the graph in half and matching the peaks with $|m_N| > 1$. (The asymmetry of the central peak prevents it from being used to locate the center of the spectrum.) The frequency differences between the center and the side peaks were measured and the average value was used in Eq. 2.33 to obtain $\bar{\gamma}$. The actual data are given below.

	Peak: m_N =						
	-3	-2	-1	center	+1	+2	+3
Frequency of Spectrum Center (MHz)							
Curve 1				15.460			
Curve 2				15.522			
Curve 3				15.615			
Frequency from Center (kHz)							
Curve 1		-147	-68	0	65	147	220
Curve 2	-229	-142	-70	0	68	143	223
Curve 3		-140	-70	0	68	145	222
Av. Freq. from Center (kHz)	-229	-143 ±4	-69.3 ±1.3	0	67 ±2	145 ±2	221.7 ±1.7
Difference Freq. (kHz)	86	73.7	69.3	67	78	76.7	

Average Difference = 72.9 (value for $m_N = -3$ excluded).

The frequency difference between peaks appears to increase with increasing $|m_N|$; the reason for this is not clear, and requires more precise measurements to be established conclusively. In any case, the average frequency difference actually reflects the separation of the outermost peaks ($m_N = -2$ and $m_N = 3$), since in taking the average the differences are added, giving the total separation, and then divided by the number of peaks less one. Thus the average is dominated by the large m_N peaks whose centers are less precisely determined than those with smaller m_N. Therefore in calculating $\bar{\gamma}$ we shall weight the central peaks more heavily, and shall take as the average separation 72 kHz. With a Zeeman frequency of approximately 15.5 MHz, Eqs. 2.33 and 2.34 give

$$x = 0.1223$$

Using this value in Eq. 2.35 with $\Delta\nu = 72$ kHz, we find $\bar{\gamma} = 239.9$ kHz. Because the centers of the molecular resonance peaks are determined to no better than ~ 1.5 kHz, the separation is uncertain by at least that amount, or 2%. We find that

$$\bar{\gamma} = 240(5) \text{ kHz}.$$

B. Far Spectrum

Two examples of far spectra are shown in Fig. 5-6. Spectrum (a) was recorded with a 28 KHz apparatus linewidth, (b) with a 35 kHz linewidth. In neither case does the spectrum extend more than 1.4 MHz from the central peak. This is in contrast to the following result: since a maximum of 36 rotational states are permitted in KAr, and the average peak separation found in the previous section is approximately 72 kHz, the spectrum can extend as far as 2.6 MHz from its center. The narrowing of the spectrum is most likely due to two effects discussed in Chapter 2: a low rotational temperature will decrease the population of high N states, reducing the intensity of large-m_N peaks, while a decrease in γ with increasing N will move the outer peaks closer to the center. These effects are connected: low temperature, for which few high-N states are populated, would reduce the effect of the radial dependence of γ. Furthermore, depending upon experimental conditions, the tail of the spectrum, due to weakly populated states, can be lost in background noise.

It was originally thought, based on an incomplete theory of the molecular spectrum, that the total width of the far spectrum could provide values for the molecular rotation and vibration temperatures. As will be shown in the next section, however, the spectral width is relatively insensitive to temperature variations, so observations of the far spectra are not particularly informative about the molecular temperature. Because the original theory neglected second-order terms, it was presumed that the spectrum was symmetrical about the central peak, and observations of only the low-frequency side of the spectrum were made. In the next section we show that the second-order terms create a substan-

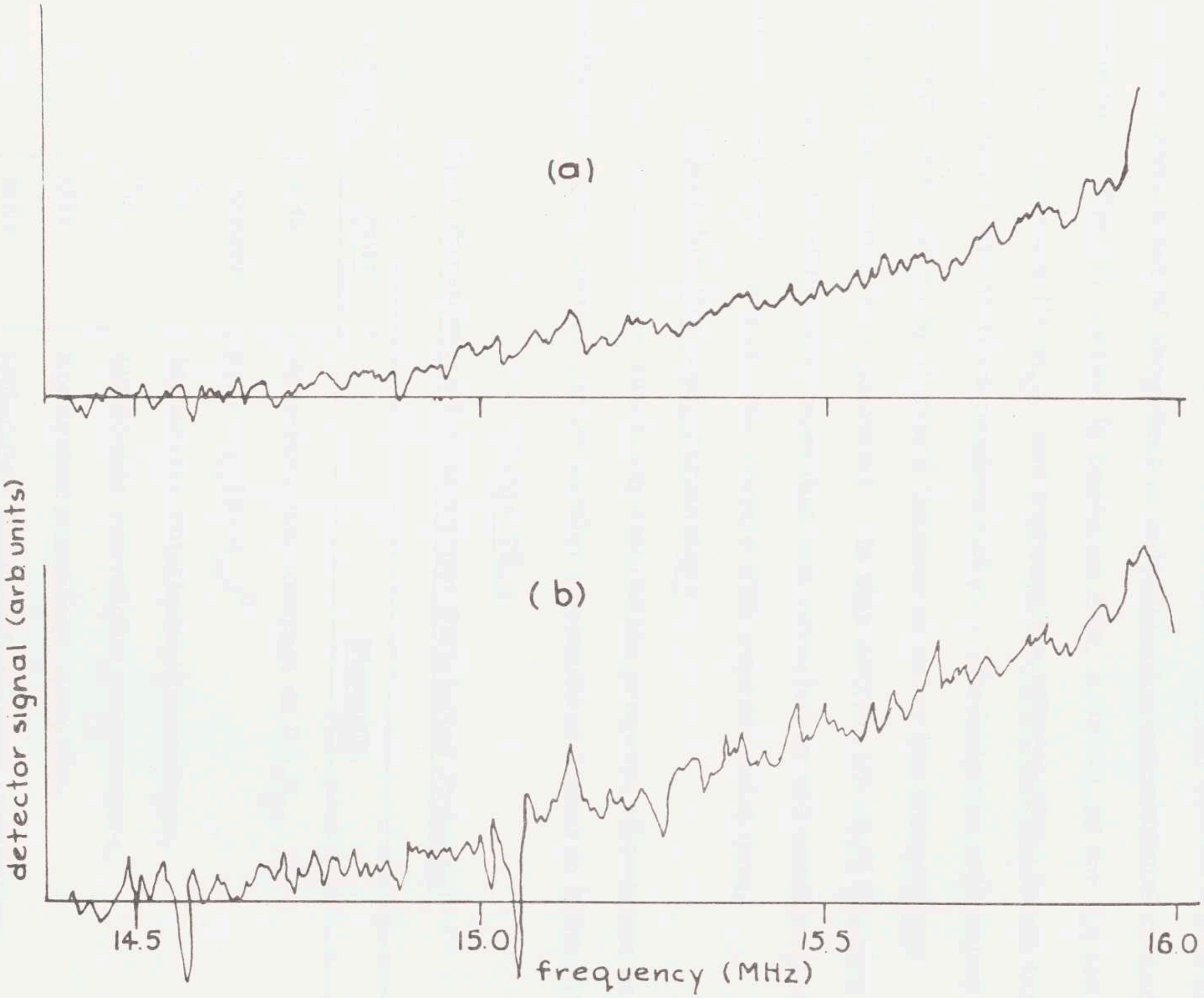

Fig. 5-6 Experimental KAr Spectra.

tial asymmetry in the spectrum, so that further observation of the entire far spectrum would be useful.

C. Computer Simulation of the Molecular Spectrum

Dr. David Pritchard, in collaboration with Dr. Richard Freeman, has developed a set of programs to calculate the experimental molecular spectrum. The calculation is based on Eqs. 2.39--2.42 for the transition frequency of a state (N, m_N), and includes the effects of the beam temperature and of the state-dependence of γ. The latter is calculated by the programs written by Richard Goldhor to solve the Schrodinger equation for a molecular potential. In this section we shall discuss several aspects of the spectrum that are revealed by the computer calculations, and shall compare the results with experimental data.

(i) Adjustable Program Parameters

The van der Waals spectrum simulation program allows one to specify the experimental and molecular parameters listed in Table T5.1.

Table T5.1

Input Parameters for Spectrum Simulation Program

Symbol	Units	Meaning
γ_o	kHz	Spin-rotation constant at $R = R_m$.
n	integer	$\gamma(R) = \gamma_o (R/R_m)^n$
T_r	^oK	Molecular rotational temperature.
T_v	^oK	Molecular vibrational temperature.
δ_{app}	kHz	Apparatus resonance linewidth
ν_Z	MHz	Molecular Zeeman frequency (transition frequency for $N = 0$, $m_N = 0$ state).

(ii) Calculated Spectra

The effect of the second-order terms in ν, proportional to N^2, can be demonstrated by setting n = 0 in the program, eliminating the dependence of γ on R. Figure 5-7 is a plot of the resulting spectrum for a central frequency $\nu_Z = 15.1$ MHz. All peaks are sloped toward high frequencies, as predicted by Eq. 2.41.

The second-order terms can be suppressed, and the radial dependence of γ emphasized, by calculating the spectrum for a high Zeeman frequency (that is, for a high magnetic field), and using $n \neq 0$; Fig. 5-8 shows such a spectrum, for which $\nu_Z = 100$ MHz and n = -8. The outer peaks slope symmetrically toward the central ($m_N = 0$) peak, which is itself quite narrow and symmetrical, in contrast to the case of Fig. 5-7.

The effect of temperature on the spectrum is shown in Fig. 5-9. The extent of the total spectrum, particularly on the low frequency side, is not appreciably affected by changing the temperature from 20°K to 10°K. The peaks near the center of the spectra, however, are made much sharper by lowering the temperature; this is due to decreased "smearing" of the peaks by high-N states with smaller values of γ.

It will be noticed in Figs. 5-8 and 5-9 that the high frequency peaks are more distinct than the low frequency ones. This is due to the second-order terms of ν cancelling the radial dependence of γ: for large N, γ decreases, pulling the high-frequency peaks toward lower frequency, while the N^2 term in ν pulls the peaks to higher frequency. For the low-frequency peaks these effects add rather than cancel, for here the decrease of γ pulls the peaks toward higher frequency.

The effects of temperature on the near spectrum can be seen clearly in Fig. 5-10. The ratio of peak height to total spectrum height

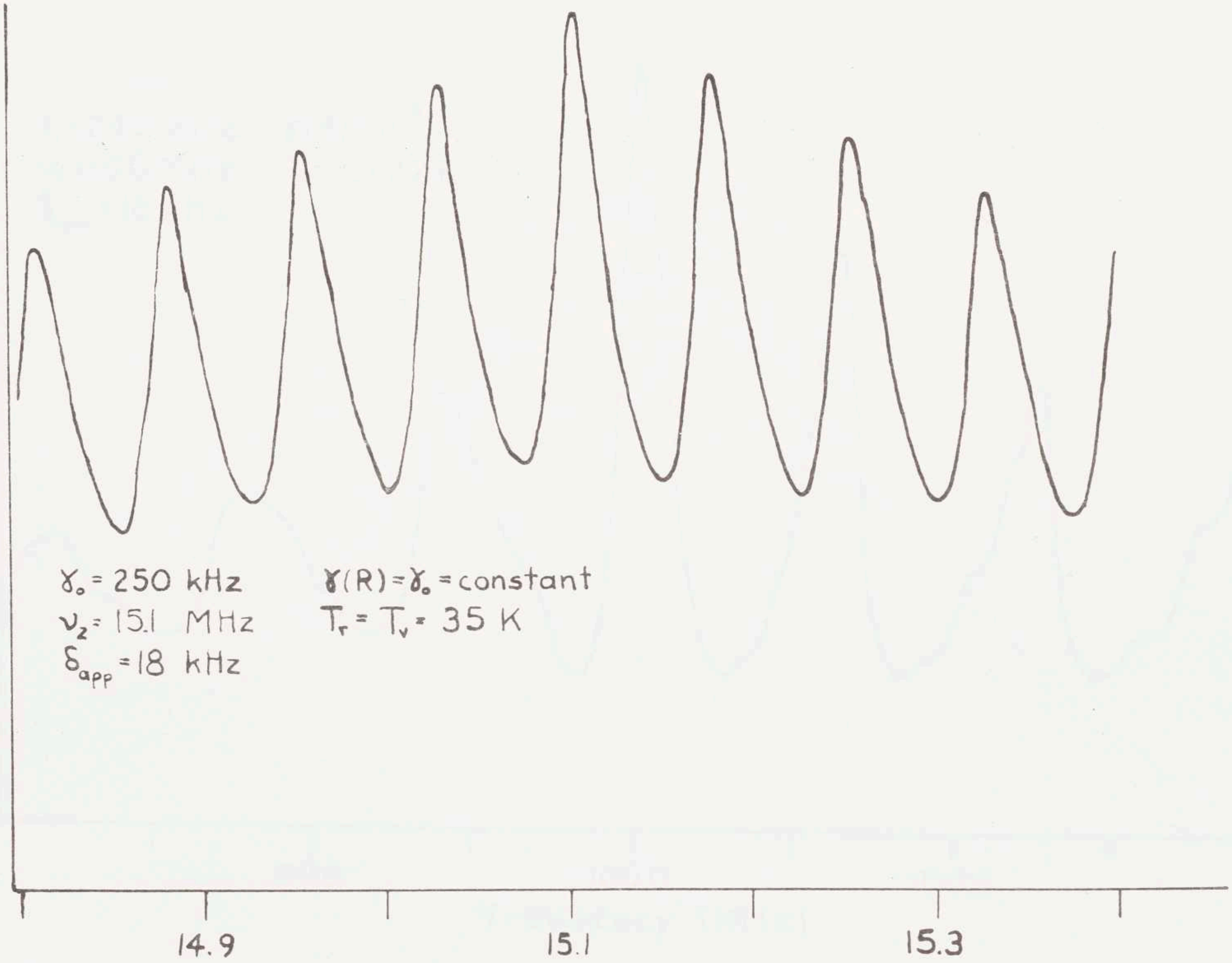

Fig. 5-7 Computer-Generated KAr Spectrum (γ = Constant).

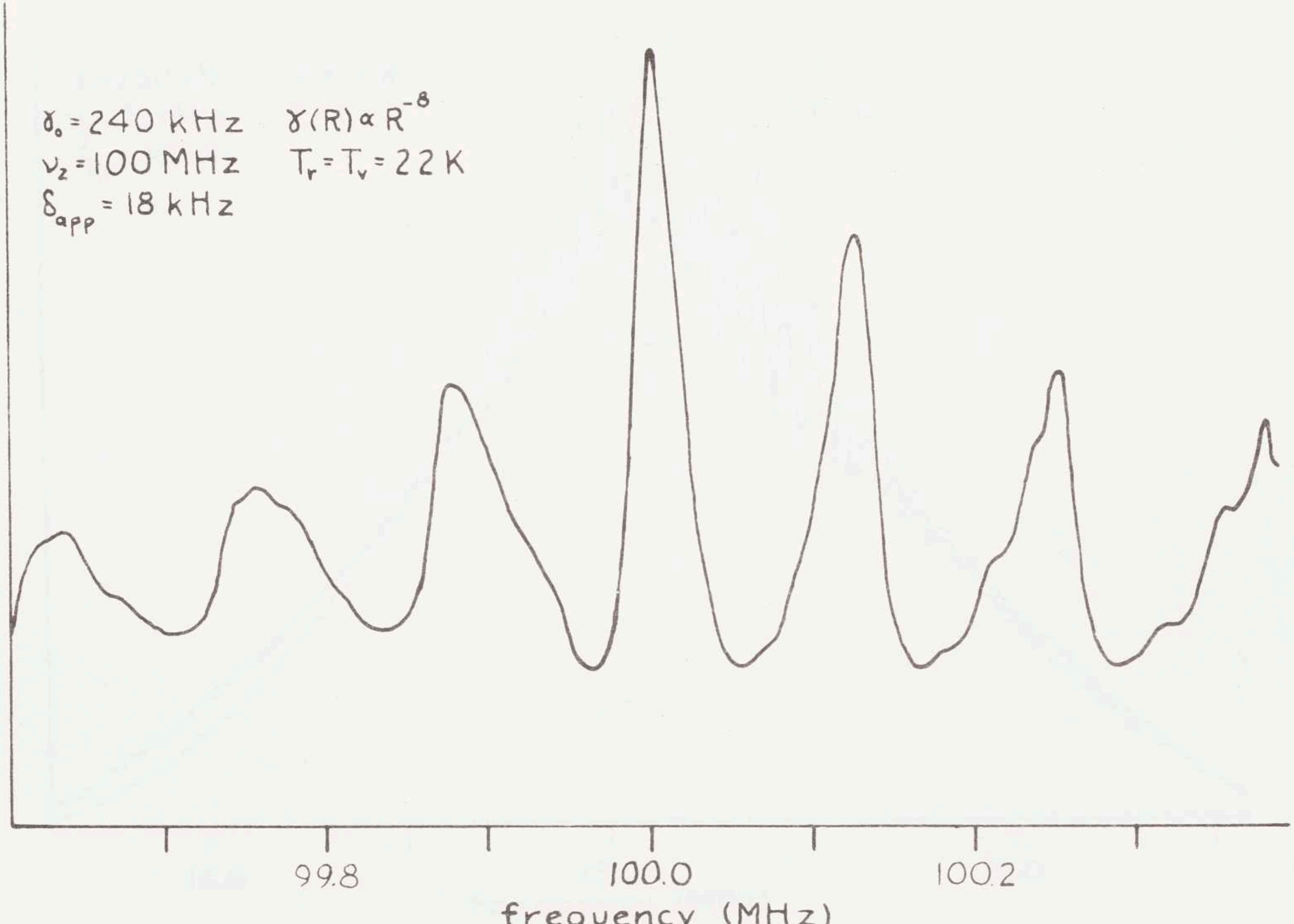

Fig. 5-8 Computer-Generated KAr Spectrum (Second-Order Terms Suppressed).

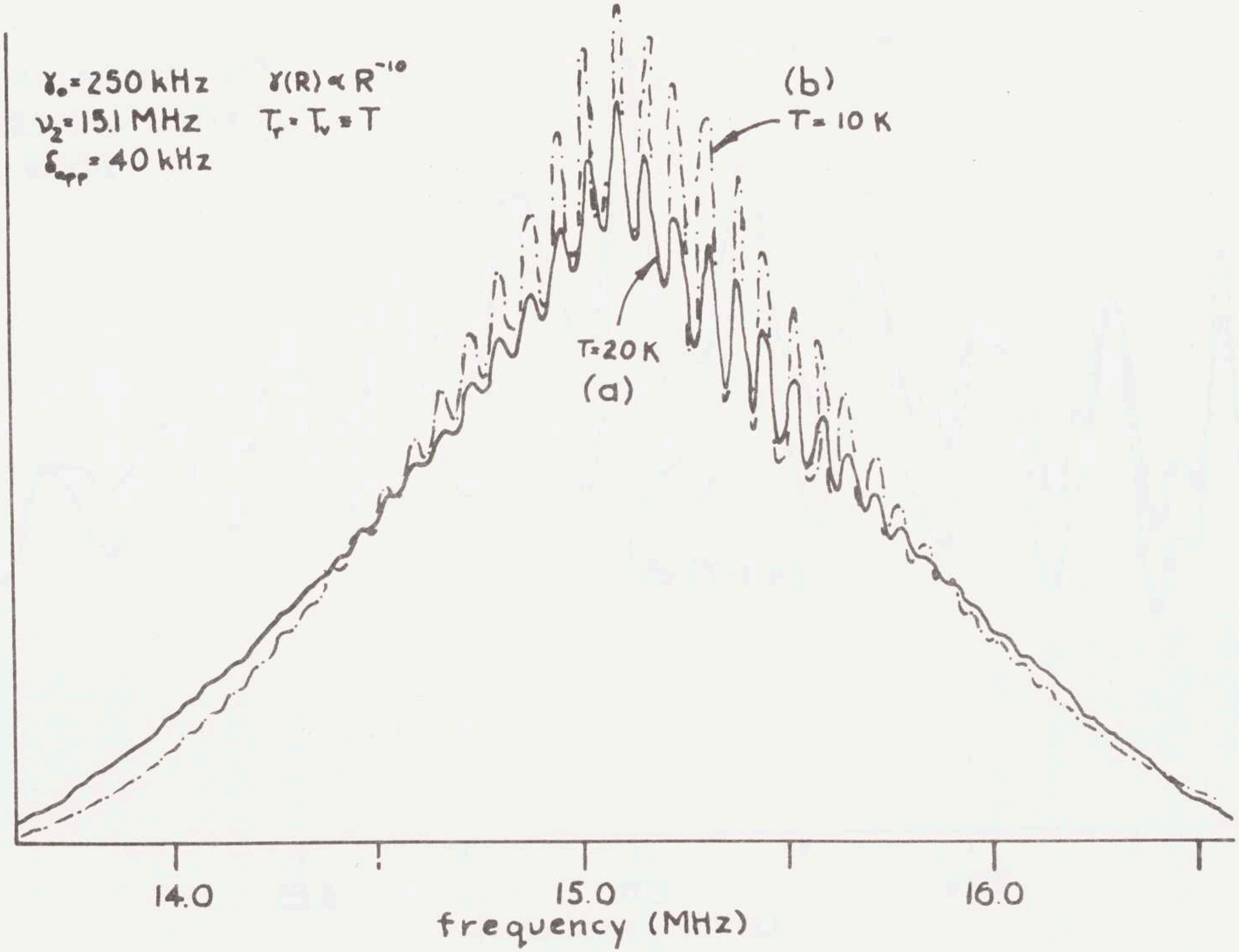

Fig. 5-9 Computer-Generated KAr Far Spectrum.

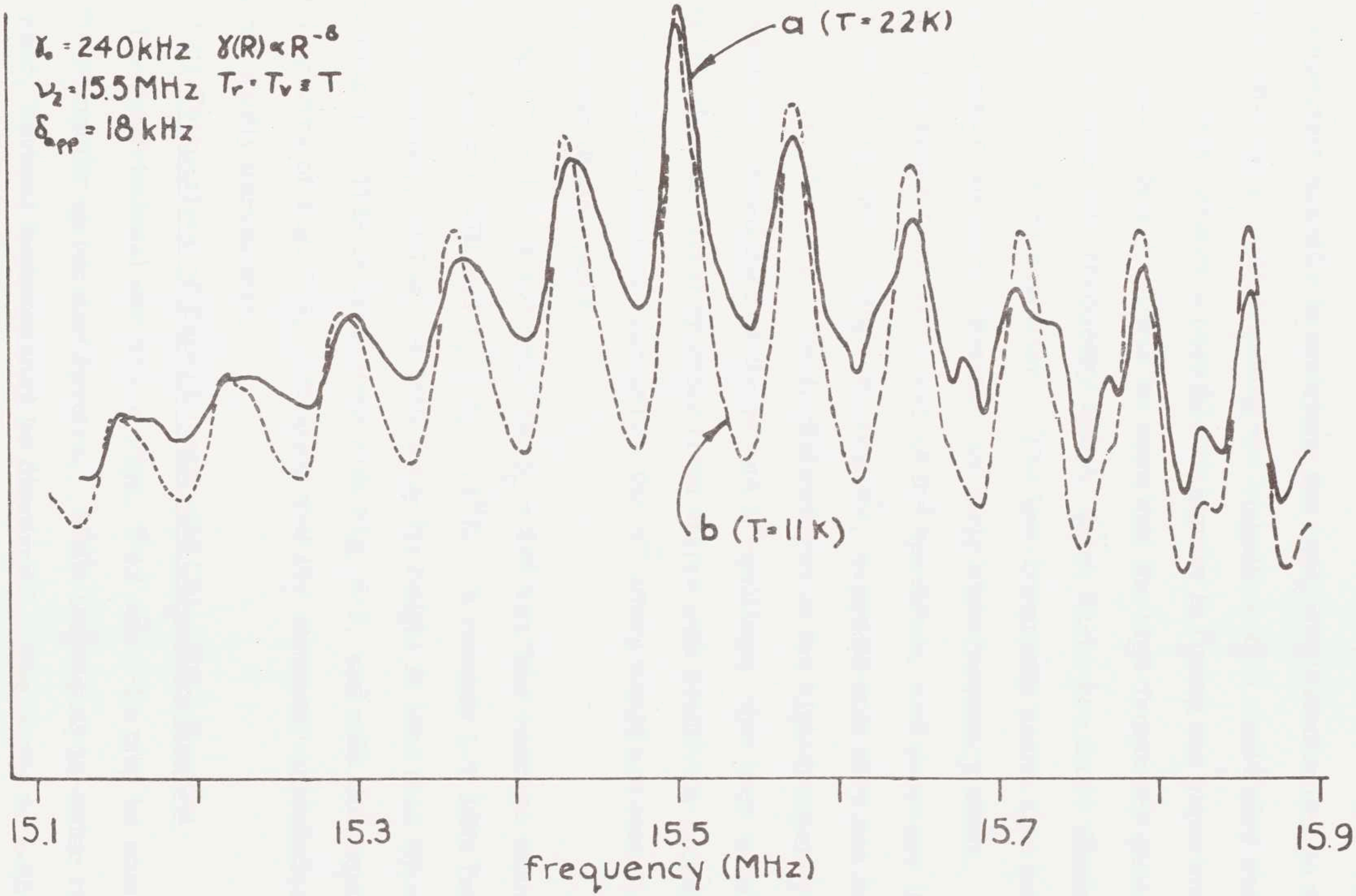

Fig. 5-10 Computer-Generated KAr Near Spectra.

is much greater in the 11 K spectrum (a) than in the 22 K spectrum (b), all other parameters being equal. The relative peak-to-valley distance is an important quantity in matching the computer calculations to the experimental data. (Decreasing the magnitude of n would also sharpen the peaks; this creates a possible ambiguity in fitting the experimental and theoretical data.) It will be seen that the high-frequency peaks have "knees" on their low-frequency sides; these knees are more distinct in the high temperature spectrum. The low-frequency peaks also have knees, considerably less distinct, on their high-frequency sides. The fact that the knees face the center of the spectrum, and decrease in prominence with decreasing temperature, suggests that they are due to the radial variation of γ. Their distinctness in the high-frequency peaks is a result of cancellation of the γ- and N^2-pullings; that they exist at all probably indicates that they arise from states with relatively small N but large vibrational quantum numbers; the N^2 effect would not cancel the pulling due to these states.

Figure 5-11 is a spectrum for γ_o = 240 kHz (the average value found in section 5.2B) and $T_r = T_v = 11^oK$. It extends 1.7 MHz from its central frequency, and at 1.4 MHz away its height is less than 3% of the center height. This is consistent with Fig. 5-9, and with the experimental spectra of Fig. 5-6, indicating that the computer calculation is at least not wildly unrealistic.

(iii) Comparison of Experimental and Calculated Spectra

The experimental spectra of Figs. 5-12 and 5-13 may be compared with the computer-generated spectra. While the signal-to-noise ratio is quite poor, several features may be discerned. The peaks on both the low- and high-frequency sides slope toward high frequencies, the low-

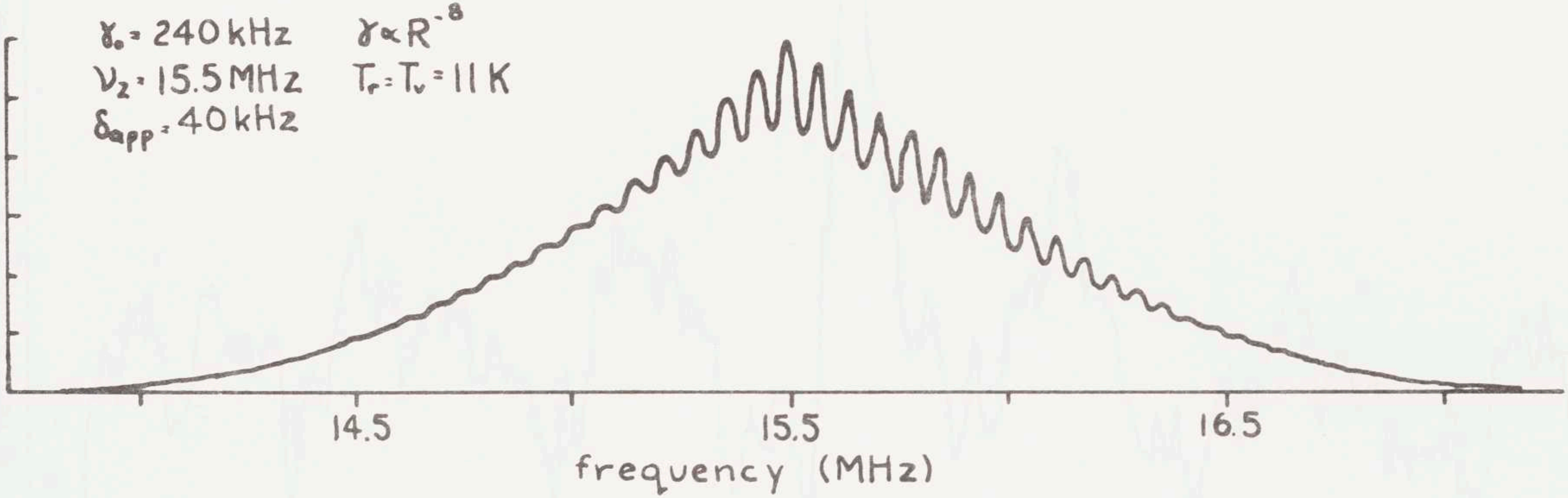

Fig. 5-11 Computer-Generated KAr Near Spectrum.

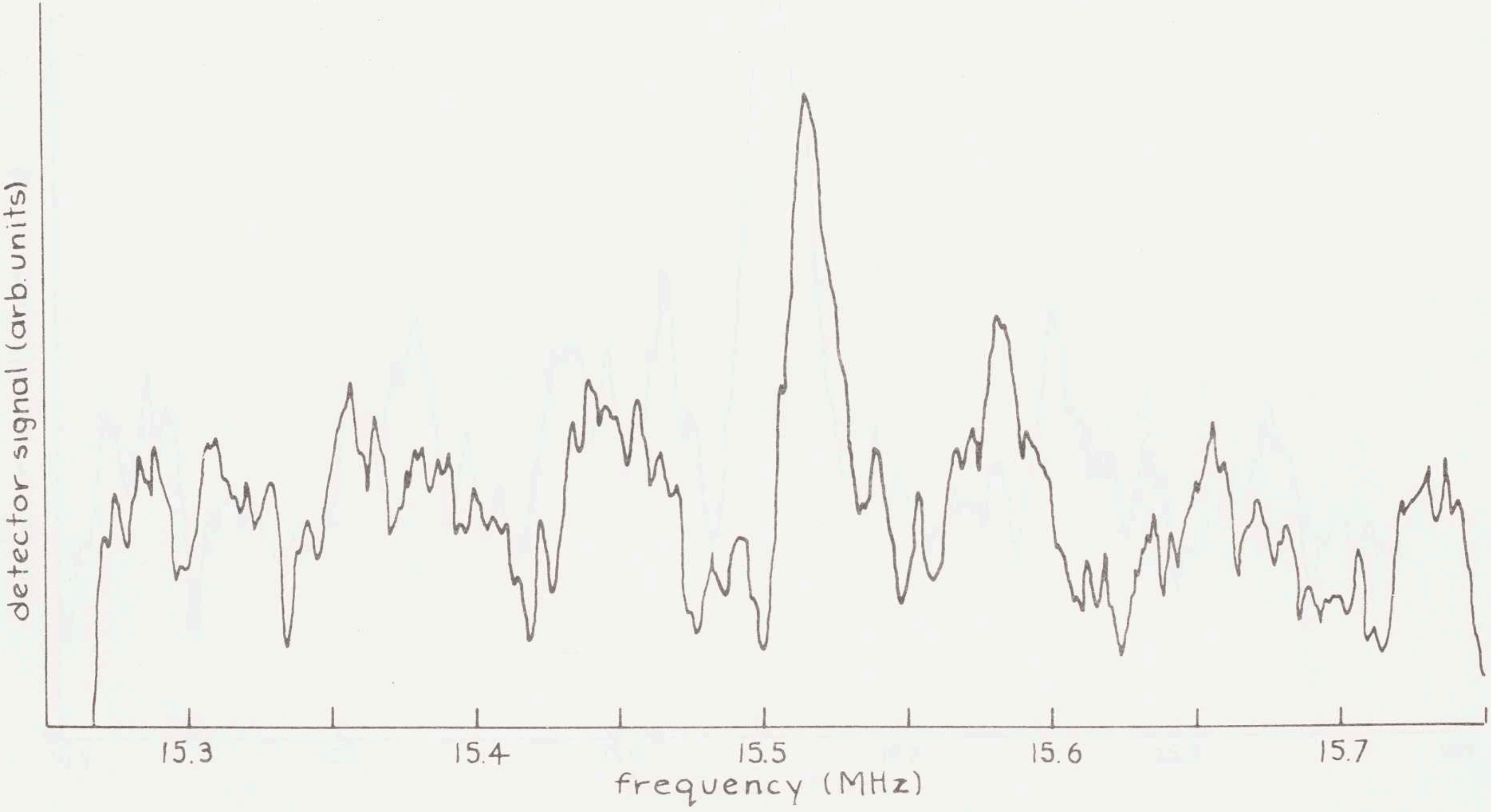

Fig. 5-12 Experimental KAr Near Spectrum.

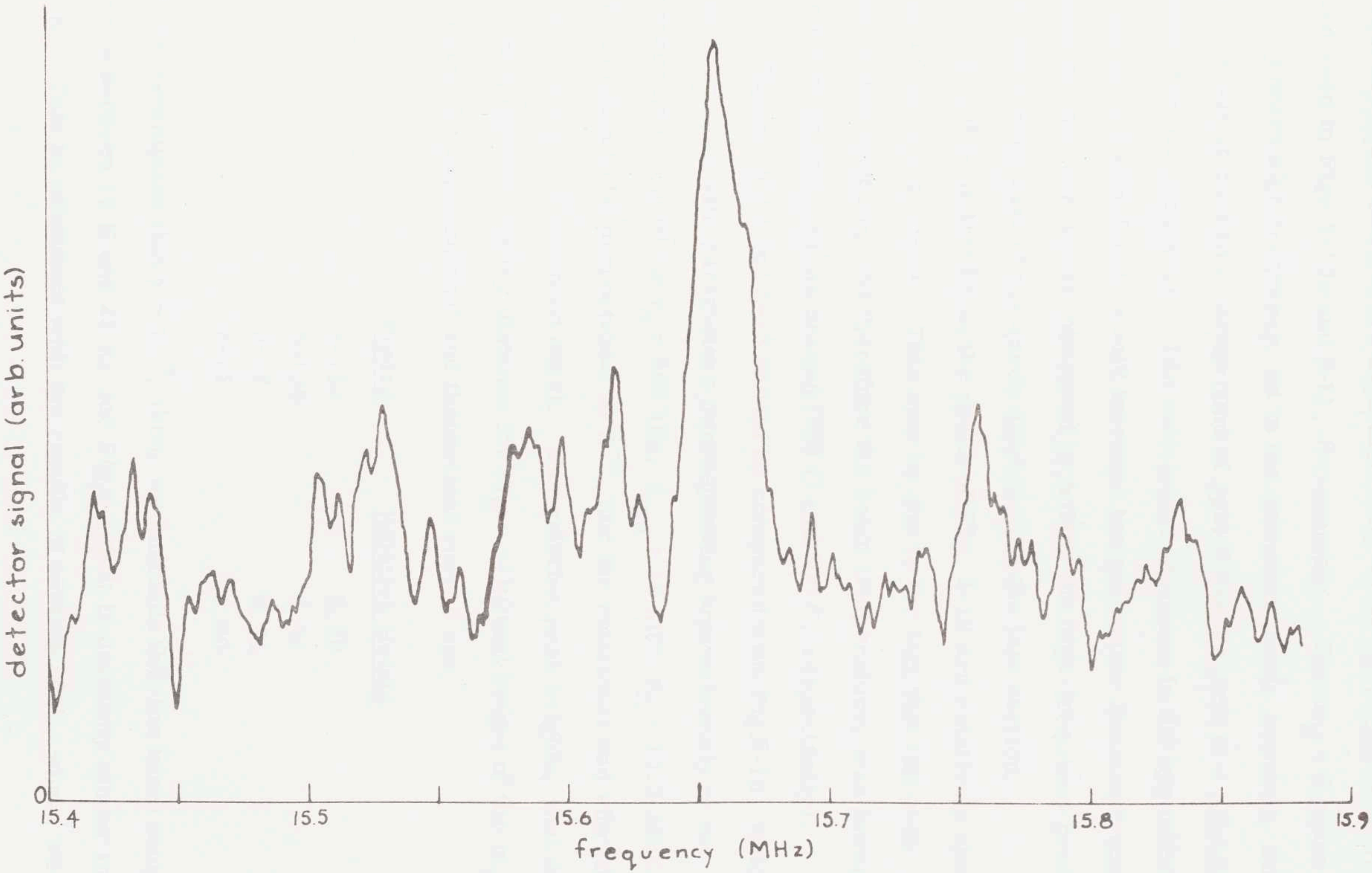

Fig. 5-13 Experimental KAr Near Spectrum.

frequency peaks being more asymmetrical; these characteristics have been seen in Figs.5-10b and 5-11, for example. The $m_N = 0$ peaks also slope toward high frequency, as in the computer plots; however, this may be due in part to a background of spin-flipped atoms at a slightly lower Zeeman frequency. (An anticipated decrease in the hyperfine coupling in the molecule would increase the molecular Zeeman frequency.) Although they are almost obscured by noise, the high-frequency peaks contain suggestions of the knees discussed in the last section.

It will be noticed that the peaks of Fig. 5-12 are relatively sharper than those of Fig. 5-13. This may be due to the fact that the oven nozzle temperature, and therefore the beam temperature, was lower in the first case than in the second (560 C and 600 C, respectively).

Figures 5-12 and 5-13 should be compared with Fig.5-10, which was calculated with parameters corresponding approximately to the experimental conditions $\gamma_o = 240$ kHz, $\delta_{app} = 18$ kHz, $\nu_Z = 15.5$ MHz. $\gamma(R)$ is taken to be proportional to R^{-8}, and the rotational and vibrational temperatures are assumed equal. The relative peak heights, that is, the ratio (peak-to-valley distance for $m_N = -1$):(total height of the $m_N = 0$ peak) for the experimental and theoretical curves are:

Figure	Relative Height
5-10a	0.20
5-10b	0.44
5-12	0.34
5-13	0.30

On the assumption that $\gamma \sim R^{-8}$, then, we conclude that the beam temperature is between 11 K and 22 K; for Fig.5-10b it is certainly closer to 11 K. This is consistent with the results of section 5.1C, where we found an atom temperature of 14 K and a dimer temperature of 12 K.

The peak separations of Fig.5-10b are between 69 and 73 kHz, in good agreement with the results of section 5.2A. (The peaks of 5-10a are not exactly in step with those of 5-10b, and the high-frequency peaks of (a) seem to become progressively more spread out. This is probably due to the pulling effect of the higher rotational and vibrational states, which are more populated in (a).)

More definitive measurements of $\gamma(R)$ and of the rotational and vibrational temperatures await three things: less noisy experimental data, further computer simulations, and an experimentally determined interatomic potential for more accurate calculations of $\gamma(R)$. Nevertheless, the present agreement between our experimental data and the computer calculations provides a great deal of confidence in our present understanding of the molecular spectrum.

BIBLIOGRAPHY

AND65 Anderson, J. B., and J. B. Fenn, Phys. Fluids 8, 780 (1965).

AND66 Anderson, J. B., R. P. Andres, and J. B. Fenn, Advances in Chemical Physics 10, 275 (1966).

ATA73 Atakan, Ahmet, K., and Harry C. Jacobson, Phys. Rev. A7, 1452 (1973).

BAY69 Baylis, W. E., J. Chem. Phys. 51, 2665 (1969).

BER62 Bernheim, R. A., J. Chem. Phys. 36, 135 (1962).

BOU69 Bouchiat, C. C., M. A. Bouchiat, and L. C. L. Pottier, Phys. Rev. 181, 144 (1969).

BOU70 Bouchiat, C. C. and M. A. Bouchiat, Phys. Rev. A2, 1274 (1970).

BOU72a Bouchiat, M. A., J. Brossel, and L. C. Pottier, J. Chem. Phys. 56, 3703 (1972).

BOU72b Bouchiat, M. A. and L. C. Pottier, J. de Phys. (Paris) 33, 213 (1972).

BRY59 Brymer, R. and W. Steckelmacher, J. Sci. Inst. 36, 278 (1959).

CHE57 Ch'en, S. Y. and M. Takeo, Rev. Mod. Phys. 29, 20 (1957).

CHU72 Chu, F. Y.-F., Ph.D. Thesis, Massachusetts Institute of Technology (1972), unpublished.

DUR68 Düren, R., G. P. Raabe, and Ch. Schlier, Z. Physik 214, 410 (1968).

DYK72 Dyke, T. R., G. R. Tomasevich, W. Klemperer, and W. E. Falconer, J. Chem. Phys. 57, 2277 (1972).

FOR72 Foreman, P. B., G. M. Kendall, and R. Grice, Mol. Phys. 23, 117 (1972).

FUL65 Fuller, G. H. and V. W. Cohen, "Nuclear Moments" (Appendix 1 to Nuclear Data Sheets), Oak Ridge National Laboratory (Oak Ridge, Tenn.), March 1965.

GOL70 Golomb, D., R. E. Good, and R. F. Brown, J. Chem. Phys. 52, 1545 (1970).

GOL72 Golomb, D., R. E. Good, A. B. Bailey, M. R. Busby, and R. Dawbarn, J. Chem. Phys. 57, 3844 (1972).

GOL72A Goldhor, R., Thesis, Massachusetts Institute of Technology (1972), unpublished.

GOR71 Gordon, R. J., Y. T. Lee, and D. R. Herschbach, J. Chem. Phys. 54, 2393 (1971).

HAG72 Hagena, O. F. and W. Obert, J. Chem. Phys. 56, 1793 (1972).

HED72 Hedges, R. E. M., D. L. Drummond, and Alan Gallager, Phys. Rev. A6, 1519 (1972).

HEN73 Henderson, G. and G. E. Ewing, J. Chem. Phys. 59, 2280 (1973).

HER64 Herman, R. M., Phys. Rev. 136, A1576 (1964).

HER50 Herzberg, G., Spectra of Diatomic Molecules, Van Nostrand Reinhold Company, New York (1950).

KUD71 Kudian, A. K. and H. L. Welsh, Can. J. Phys. 49, 230 (1971).

MAR39 Margenau, H., Rev. Mod. Phys. 11, 1 (1939).

MAU67 Mausteller, J. W., F. Tepper, and S. J. Rodgers, Alkali Metal Handling and Systems Operating Techniques, Gordon and Breach (New York), 1967.

MIL67 Milne, Thomas A. and Frank T. Greene, J. Chem. Phys. 47, 4095 (1967).

MIL70 Milne, Thomas A, A. Eugene Vandergrift, and Frank T. Greene, J. Chem. Phys. 52, 1552 (1970).

MOO71 Moore, C. E., Atomic Energy Levels, Nat. Bur. Stand. (U. S.) (1971).

NOV73 Novick, S. E., P. Davies, S. J. Harris, and W. Klemperer, J. Chem. Phys. 59, 2273 (1973).

PRI71A Prince, R. H. and J. A. Cross, Rev. Sci. Inst. 42, 66 (1971).

PRI71B Pritchard, D. E., R. L. E. Quarterly Progress Report No. 100, p. 27, M. I. T. Research Laboratory of Electronics, Cambridge, Mass. (January 1971).

PRI73 Pritchard, D. E., private communication.

RAM56 Ramsey, N. F., Molecular Beams, Oxford University Press, London (1956).

SHA53 Shapiro, Asher H., The Dynamics and Thermodynamics of Compressible Fluid Flow, Roland Press (New York) 1953.

SIN73 Sinha, M. P., A. Schultz, and R. N. Zare, J. Chem. Phys. 58, 549 (1973).

SOB69 Soboll, H., Z. Naturforsch. 24a, 2023 (1969).

TAN72 Tanaka, Y. and K. Yoshino, J. Chem. Phys. 57, 2964 (1971).

YEA72 Yealland, R. M., J. M. Deckers, I. D. Scott, and C. T. Tuori, Can. J. Phys. 50, 2469 (1972).

ZOR74 Zorn, J. C. and T. C. English, Methods of Experimental Physics, Vol. 3 (2nd edition), D. Williams, Ed., Academic Press, Inc., New York (to be published 1974).

ACKNOWLEDGEMENTS

It is a commonplace to say that one's thesis work could not have been accomplished without the aid of others; nevertheless it is the truth. Perhaps the most pleasurable aspect of writing a thesis is thanking those who have lent a helping hand along the way.

The single most important individual in a student's professional life is his research advisor. Professor Daniel Kleppner suggested this project. Without his vision it would never have been started; without his suggestions and encouragement it would not have reached fruition. I am grateful for his help in all aspects of the work, not least his aid in extirpating obfuscatory locutions from the remainder of this text.

Professor David Pritchard has always been ready with an idea or suggestion in time of need. His shrewd explanations of why things don't work, and his methods for improving them, have been of great assistance in dark hours; his ability to discern data in overwhelming noise is nothing short of awe-inspiring.

My association with Dr. Richard Freeman, though relatively short, has been most fruitful. His physical insight and infectious enthusiasm have helped speed the work along; our many discussions of physics have taught me a great deal.

Dr. Frank Chu paved the way for this thesis by showing that paramagnetic van der Waals molecules could be produced in a beam and separated from the atom background.

I should like to thank Jerome Apt III for his able assistance in the lab during the early--and sometimes frustrating--stages of this work.

Richard Goldhor has made a valuable contribution to the analysis

of the molecular spectra by developing computer programs for calculating quantum-mechanical expectation values.

I am deeply indebted to Dr. Frederick G. Walther for his unstinting help and advice concerning the next step in my career; he has exerted himself unselfishly in my behalf.

Thesis work is not carried out in a vacuum--at least, not all of it. One's fellow students and co-workers can help make life pleasant. I am fortunate to have kibitzed with, lunched with, partied with, and even discussed physics with William Phillips, William Cooke, Dr. Theodore Dukas, Michael Littman, Francine Wright, and Gary Carter. In addition, Gary and I have shared a laboratory for several years. He has listened to my gripes, commiserated when things went badly, cheered when they went well, put up with my tendency to increase the lab's entropy, and joined me in running around the Charles River.

Over the years, Franklin Payne and I have had many enjoyable discussions of subjects from plant care to figure skating. Through his wide knowledge and consummate skill as a machinist, he has taught me much about machine work and mechanical techniques; in addition, he has built part of the experimental apparatus for this thesis.

Much of the experimental equipment was constructed by the skilled machinists of the Research Laboratory of Electronics machine shop. Many suggestions on construction techniques were made by the shop's foreman, John Keefe.

A thesis is not an isolated event, but represents the culmination of many years of study. I wish to express my appreciation to Professor Sanborn C. Brown for his help and encouragement in the early stages of my graduate career.

Several persons have provided invaluable help in putting this text into its present form. John Mara prepared many of the illustrations; Dr. Frederick Walther spent several late evenings with me developing and printing Fig. 3-2; and Mrs. Delphine Radcliffe expertly produced a fine manuscript.

I want to express my appreciation to David Pritchard and Richard Freeman for the time and effort they expended at the eleventh hour in making the spectrum-generating program work.

The Massachusetts Institute of Technology provided financial support through an Alfred E. Sloan Traineeship.

Most important of all, beyond mere words of thanks, is my wife Marsha. In sharing my life she has shared every aspect of this thesis, and it is to her that I dedicate it.